2016

Modelling and improvement of proton computed tomography

Valentina Giacometti
University of Wollongong

MODELLING AND IMPROVEMENT OF PROTON COMPUTED TOMOGRAPHY

A Dissertation Submitted in Fulfilment of
the Requirements for the Award of the Degree of

Doctor of Philosophy

from

UNIVERSITY OF WOLLONGONG

by

Valentina Giacometti

B.Sc. Mathematical Engineering
M. Sc. Nuclear Engineering

School of Physics
Faculty of Engineering

2016

CERTIFICATION

I, Valentina Giacometti, declare that this thesis, submitted in fulfilment of the requirements for the award of Doctor of Philosophy, in the School of Physics, Faculty of Engineering University of Wollongong, is wholly my own work unless otherwise referenced or acknowledged. The document has not been submitted for qualifications at any other academic institution.

(Signature Required)

Valentina Giacometti
30 08 2016

To my mum and dad

And to Carlo... I wish you could have read this

Table of Contents

List of Tables

List of Figures

MODELLING AND IMPROVEMENT OF PROTON COMPUTED TOMOGRAPHY

Valentina Giacometti

A Thesis for PhD in Medical Physics

School of Physics
University of Wollongong

ABSTRACT

Proton computed tomography (pCT) is a promising imaging technique to substitute x-ray CT for more accurate proton therapy treatment planning as it allows to calculate directly proton relative stopping power (RSP) from proton energy loss measurements.

A novel pCT scanner (phase II pCT scanner prototype) was completed with a silicon-based particle tracking system and a 5 stage scintillating energy detector. In parallel, a modular software platform was developed to characterize the performance of the pCT system. The modular pCT software platform consists of (1) a Geant4-based simulation modelling the Loma Linda (California, USA) proton therapy beam line and the phase II pCT scanner prototype, (2) water equivalent path length calibration and (3) conversion of the scintillating energy detector, and (4) image reconstruction algorithm for the reconstruction of the RSP of the scanned object. The platform has been validated with respect to experimental measurements and proved to be a valid tool to characterize and optimize the novel pCT system.

The results show that the pCT software platform accurately reproduces the performance of the existing phase II pCT scanner prototype with a RSP agreement between experimental and simulated values to better than 1.5%.

The pCT software platform was also used to perform a dosimetric evaluation of the phase II pCT scanner prototype. The results are very promising because the dose delivered during a pCT scan was calculated to be 10 time less than the dose delivered during a cone-beam CT scan.

Finally, the accuracy of the most likely path calculation in homogeneous and heterogeneous medium was also investigated using a pixelated Medipix detector. The detector was successfully integrated with the experimental phase II pCT scanner prototype. A Geant4 simulation of the pCT-Medipix system was also developed and theoretically predicted, simulated and experimental data were compared and analysed. The agreement between experimental and simulated results is always within one standard deviation and the correlation coefficients between predicted and measured data is close to 1, showing a good agreement between predicted and measured data.

Acknowledgements

This PhD project started in 2012, from a collaboration between the University of Wollongong and the Loma Linda University, CA, USA. It is a pleasure for me to thank Prof. Anatoly Rosenfeld and Dr. Reinhard Schulte who made this thesis possible. I do not think I know two people who work harder than you: thanks for your guidance, for your support and for everything you taught me, both as scientists and as a human beings.

I am grateful to all the pCT collaboration who made possible the realisation of an innovative pCT scanner that, hopefully, one day, will be an instrument that could help in saving some people lives. In particular, thanks to Prof. Bashkirov, Prof. Johnson, Prof. Sadrozinski, Dr. Zatserklyaniy, and Dr. Plautz: thanks for your help, for your patience and for everything you taught me.

A special thank to everyone at CMRP: the support, help and encouragement that each one of you always gave me was simply great. In particular, thanks to Dr. Susanna Guatelli: I could have not asked for a better supervisor. You are an inspiration for me to follow for the rest of my life.

I owe my deepest gratitude to my parents: thanks for supporting me, pushing me and always being there for me. I would like to express my sincere gratitude also to my godparents, my uncles, aunts, and cousins: no matter how far I go, you are always asking me when I am coming back.

Far West Thanks to Ryan, John, Josh, Raquel for the great memories (and nickname) I got from Salem CT. Thanks to Marghe, Roger and Pier for making the lab a better place. A special thanks to Diogo and the lucky coincidence of being, again, in the same State at the same time: thanks, in particular, for introducing me to Silvio, Stefano and Sole.

Down Under Thanks to my Aussie friends (Matt, Pricey, Jesse, Odi in particular) who made me feel at home in a new land, teaching me important cultural life lessons. Thanks to Sara, Enrico, Davide and Mirko because I would have never survived this year without them. Thanks to all my other Italian friends, also Rino and Nelda, for the singing and eating moments. Thanks to Christel for being an idiot. Thanks to all the volley-people for making me looking forward for the weekend. Thanks and sorry to all the other people I cannot mention here for space issues.

My Lovely Boot Paolo, Gra, Marco and Tella, please, do not stop fighting for us. Tella, thanks for your patience. Gra, thanks for the voice messages. Marco, thanks for your wise advice. Paolo, thanks for making me smile and driving me crazy at the same time. Ila and Ale, I would be lost without you and without Ila's email reminding me the Etti's family skype meetings. Marta and Ele, thanks for being as crazy as me. Matti, thanks for being always present, no matter the time zones where we are. Mati, our friendship is unusual but crucial for me: thanks for helping me the most when I left. Thanks to Fede and Laura for waiting for me.

List of Publications

Journal Pubblication

1. V. A. Bashkirov, R. W. Schulte, R. F. Hurley, R. P. Johnson, H. F. W. Sadrozinski, A. Zatserklyaniy, T. E. Plautz, V. Giacometti, "Novel scintillation detector design and performance for proton radiography and computed tomography", *Medical Physics*, **43** (2), 664-74 (2016). DOI: 10.1118/1.4939255.

2. R. P. Johnson, V. A. Bashkirov, L. DeWitt, V. Giacometti, R. F. Hurley, P. Piersimoni, T. E. Plautz, H. F. W. Sadrozinski, K. E. Schubert, R. W. Schulte, B. Schultze, A. Zatserklyaniy, "A Fast Pre-Clinical Head Scanner for Proton CT", *IEEE Transactions on Nuclear Science*, **63** (1), 52-60 (2016). DOI: 10.1109/TNS.2015.2491918

3. H. F. W. Sadrozinski, T. Geoghegan, E. Harvey, R. P. Johnson, T. E. Plautz, A. Zatserklyaniy, V. A. Bashkirov, R. F. Hurley, P. Piersimoni, R. W. Schulte, P. Karbasi, K. E. Schubert, B. Schultze, V. Giacometti, "Operation of the Preclinical Head Scanner for Proton CT", *Nuclear Instruments and Methods in Physics Research Section A: Accelerators, Spectrometers, Detectors and Associated Equipment* , **831**, 394-99 (2016). DOI: 10.1016/j.nima.2016.02.001.

4. V. Giacometti, S. Guatelli, M. Bazalova-Carter, A. B. Rosenfeld, R. W. Schulte, "Development of a High Resolution Voxelised Head Phantom for Medical Physics Applications", submitted to *Physica Medica* (2016) and accepted (2017).

5. V. Giacometti, V. A. Bashkirov, P. Piersimoni, S. Guatelli, T. E. Plautz, H. F. W. Sadrozinski, R. P. Johnson, A. Zatserklyaniy, T. Tessonnier, K. Parodi, A. B. Rosenfeld, R. W. Schulte, "Software Platform for Simulation of a Prototype Proton CT Scanner", submitted to *Medical Physics* (2016) and accepted (2017).

6. T. E. Plautz, R. P. Johnson, H. F. W. Sadrozinski, A. Zatserklyaniy, V. A. Bashkirov, R. F. Hurley, R. W. Schulte, P. Piersimoni, V. Giacometti, "Evaluation of Spatial Resolution for a Prototype Proton CT Scanner", submitted to *Medical Physics* (2016) and accepted (2016).

Conference Proceedings

1. V. Giacometti, S. Guatelli, A. Zatserklyaniy, R. P. Johnson, H. F. W. Sadrozinski, T. E. Plautz, P. Piersimoni, Caesar E. Ordonez, V. A. Bashkirov, A. B. Rosenfeld, R. W. Schulte, "Dosimetric Evaluation of Proton CT using a Prototype Proton CT Scanner", *2016 IEEE Nuclear Science Symposium and Medical Imaging Conference (NSS/MIC)*, Strasbourg, FR, (2016).

2. R.W. Schulte, V. A. Bashkirov, V. Giacometti, R. F. Hurley, M. Johnson, R. P. Johnson, T. E. Plautz, P. Piersimoni, H. F. W. Sadrozinski, K. E. Schubert, "A Proton CT Imaging System for Improving the Accuracy of Particle Treatment Planning and Delivery: Monte Carlo Simulations and First Experimental Results", *International journal of radiation oncology*, **93** (3), S98 (2015). DOI: 10.1016/j.ijrobp.2015.07.235.

3. R. P. Johnson, V. A. Bashkirov, V. Giacometti, R. F. Hurley, P. Piersimoni, T. E. Plautz, H. F. W. Sadrozinski, K. E. Schubert, R. W. Schulte, B. Schultze, M. Witt, A. Zatserklyaniy, "Results from a pre-clinical head scanner for proton CT", *2014 IEEE Nuclear Science Symposium and Medical Imaging Conference (NSS/MIC)*, Seattle, WA, 1-5 (2014). DOI: 10.1109/NSSMIC.2014.74308762.

4. T. E. Plautz, V. A. Bashkirov, R. F. Hurley, V. Giacometti, R. P. Johnson, H. F. W. Sadrozinski, R. W. Schulte, A. Zatserklyaniy, "Spatial resolution studies for a prototype proton CT scanner", *2014 IEEE Nuclear Science Symposium and Medical Imaging Conference (NSS/MIC)*, Seattle, WA, 1-5 (2014). DOI: 10.1109/NSSMIC.2014.7431002.

5. A. Zatserklyaniy, R. P. Johnson, S. Macafee, T. E. Plautz, H. F. W. Sadrozinski, V. A. Bashkirov, R. F. Hurley, R. W. Schulte, N. Vence, V. Giacometti, "Track reconstruction with the silicon strip tracker of the proton CT Phase 2 scanner", *2014 IEEE Nuclear Science Symposium and Medical Imaging Conference (NSS/MIC)*, Seattle, WA, 1-5 (2014). DOI: 10.1109/NSSMIC.2014.7430749.

List of Presentations

Oral presentations

- A high-resolution Dicom Digital Head Phantom, Geant4 School and Monte Carlo Workshop for Medical Physics, Wollongong, Australia, 2016.
- A High-Resolution Digital Head Phantom for Geant4 Proton Beam Simulations, Geant4 International User Conference, Bordeaux, France, 2013.
- Characterization of a Proton-CT System by means of Geant4 Simulations, Micro-Mini & Nano Dosimetry Conference, Wollongong, Australia, 2012.

Poster presentations

- Dosimetric Evaluation of Proton CT using a Prototype Proton CT Scanner, IEEE Nuclear Science Symposium and Medical Imaging Conference, Strasbourg, FR, 2016.
- A Medipix Study of Proton Paths through Heterogeneous Materials during Proton CT data Acquisition, IEEE Nuclear Science Symposium and Medical Imaging Conference, San Diego, USA, 2015.
- Macro and Nanodosimetric Evaluation of the Phase II Proton CT Scanner with Geant4 Simulations, Micro-Mini & Nano Dosimetry and International Prostate Cancer Treatment Conference, Port Douglas, Australia, 2014.
- Geant4 Simulation Platform for the Phase II Proton CT Scanner, IEEE Nuclear Science Symposium and Medical Imaging Conference, Seattle, USA, 2014.

Other posters

- Spatial Resolution Studies in Proton CT Using a Phase-II Prototype Head Scanner, American Association of Physicists in Medicine (AAPM), Washington, DC, USA, 2016.
- Design and performance of a preclinical proton CT head scanner, 3rd ESTRO Forum, Barcellona, Spain, 2015.

- Tools for Development of 4D Proton CT, American Association of Physicists in Medicine (AAPM), Anaheim, CA, 2015.
- Performance of a Proton-CT-to-Proton-CT Image Registration Algorithm for Image-Guided Proton Therapy, IEEE Nuclear Science Symposium and Medical Imaging Conference, San Diego, USA, 2015.
- Experimental Proton CT: an Update on Data Pre-Processing for Iterative Image Reconstruction, IEEE Nuclear Science Symposium and Medical Imaging Conference, San Diego, USA, 2015.
- Machine Learning Algorithm for Calibration of the Energy Detector of the Phase II Proton Computed Tomography Head Scanner, IEEE Nuclear Science Symposium and Medical Imaging Conference, San Diego, USA, 2015.
- Testing a Pre-Clinical Proton-CT Head Scanner, IEEE Nuclear Science Symposium and Medical Imaging Conference, San Diego, USA, 2015.
- Improving Proton Radiography using the Most Likely Path, IEEE Nuclear Science Symposium and Medical Imaging Conference, San Diego, USA, 2015.
- Clinical Performance Evaluation of a Phase II Proton CT Scanner, American Association of Physicists in Medicine (AAPM), Austin, TX, USA, 2014.
- Result from a Pre-Clinical Head Scanner for Proton CT, IEEE Nuclear Science Symposium and Medical Imaging Conference, Seattle, USA, 2014.
- Spatial Resolution Studies and Measurement of the Modulation Transfer Function for a Prototype Proton CT Scanner, IEEE Nuclear Science Symposium and Medical Imaging Conference, Seattle, USA, 2014.
- A Novel Phantom and Method for Calibration of the Phase II Proton CT Scanner, IEEE Nuclear Science Symposium and Medical Imaging Conference, Seattle, USA, 2014.

List of Acronyms

ART	Algebraic reconstruction technique
CCD	Charge-coupled device
CT	Computed tomography
DAQ	Data acquisition
DECT	Dual-energy computed tomography
FBP	Filtered back projection
FDK	Feldkamp–Davis–Kress
FOV	Field of view
FT	Fiber trackers
FWHM	Full width at half maximum
HU	Hounsfield unit
IMRT	Intensity-modulated radiation therapy
MC	Monte Carlo
MCS	Multi Coulomb scattering
MLP	Most likely path
MRI	Magnetic resonance imaging
MTF	Modulation transfer function
OAR	Organ at risk
PCT	Proton computed tomography
PMT	Photomultiplier tubes
RSP	Relative stopping power
Sci-Fi	Scintillating fibres
SECT	Single-energy computed tomography
SEM	Secondary electron emission monitor
SOBP	Spreadout Bragg peak
SP	Stopping power
SSD	Silicon strip detector
WET	Water equivalent thickness
WEPL	Water equivalent path length
XCT	X-ray computed tomography

Facilities

FNAL	Fermilab National Accelerator Laboratory
HCL	Harvard University Cyclotron Laboratory
HIT	Heidelberg Ion-Beam Therapy
INFN	Instituto Nazionale di Fisica Nucleare
LAMPF	Los Alamos Meson Physics Facility
LBL	Lawrence Berkeley Laboratory
LLU	Loma Linda University
LLUMC	Loma Linda University Medical Centre
LSN	Laboratori Nazionali del Sud
MGH	Massachusetts General Hospital
NIU	Northern Illinois University
NMCPC	Northwestern Medicine Chicago Proton Center
PRAVDA	Proton Radiotherapy Verification and Dosimetry Application
PREDATE	Particle Residual Energy And Tracker Enhancement
PRIMA	PRoton IMAging
PSI	Paul Scherrer Institute
UCSC	University of California Santa Cruz

Chapter 1

Introduction

Protons are increasingly used for radiotherapy, in particular, in children and when the tolerance of organs at risk becomes dose-limiting[1]. To take full advantage of the dosimetric properties of protons, the range of the proton beams in tissue has to be precisely known. The current practice of converting Hounsfield values of x-ray computed tomography (xCT) to relative stopping power (RSP) for proton treatment planning leads to systematic range errors[2]. Better range accuracy can be achieved with proton computed tomography (pCT) since it provides a direct calculation of the proton RSP from proton energy loss measurements[3].

A prototype pCT scanner with a silicon-based particle tracking system and a 5 stage scintillating energy detector has been completed by the collaboration between the University of Santa Cruz and the Loma Linda University[4]. This thesis investigates various aspects of the novel pCT sytem via modelling the existing prototype scanner.

After an historical and scientific overview on pCT (chapter 2), the prototype pCT scanner is described in detail in chapter 3. A modular software platform was developed to characterize the performance of the scanner (chapter 5). The scanner was modelled using Geant4[5], a Monte Carlo toolkit for the simulation of the passage of particles through matter. The simulation was validated with respect to experimental data and benchmarked against theoretical

predictions.

Several phantoms were scanned however, simple geometries were not sufficient to fully characterize the novel pCT scanner prototype. Therefore, a high resolution digital head phantom, modelling an existing head phantom (model HN715, CIRS, Norfolk, Virginia, USA), was created to have an accurate representation of the human anatomy (chapter 4). The use of such a detailed phantom is important to understand the effects of multiple Coulomb scattering (MCS) on pCT image reconstruction, since MCS is one of the main limitations for pCT spatial resolution.

An evaluation of the quality of the pCT image reconstruction achieved using the pCT scanner prototype was presented in chapter 6, together with a simualted dosimetric evaluation aiming at investigating the dosimetric advantages of using pCT rather than xCT for scanning a patient.

Finally, another complication in using protons for imaging purposes is associated with the determination of protons most likely path (MLP). The MLP formalism used for the work presented in this thesis was proposed by Schulte et al.[6]; an experimental study on the effects of heterogeneities on the protons MLP calculation is presented in chapter 7.

Chapter 2

Proton Computed Tomography Overview

PCT is a promising imaging technique that started to be investigated in the 60s as a possible alternative to xCT. The interest in pCT arose with the use of protons for therapeutic purposes, particularly in proton therapy.

2.1 Proton Therapy

The use of ionizing radiation (x-rays) for medical applications is one of the main treatment option in oncology since 1985[7]. The first cyclotron was invented by Ernest O. Lawrence in 1929 at the University of California, Berkley and a few years later, in 1946, the use of charge heavy particles in radiotherapy, protons in particular, was proposed by Robert R. Wilson[8] Wilson pointed out that protons have advantages over x-rays in radiotherapy because:

1. protons travel into a medium almost in a straight line;
2. protons ionise the tissue losing energy until they stop;
3. the energy of the protons is inversely related to their specific ionization i.e. protons

deposit most of the dose at the end of their path (specifically, in the last 2% of their range), when they have lost most of their energy.

The latter characteristic is a phenomenon known as Bragg peak and it can be considered one of the main reasons why protons and other heavy particles started to be used in radiotherapy.

Nowadays, oncologists and medical physicists can choose to modulate proton beam energies thus combining several Bragg peaks, in order to cover small localized areas and precisely irradiate the tumours. The plateau of deposited dose obtained is called spread-out Bragg peak (SOBP). Fig. 2.1 shows an example of SOBP and photons dose distribution. With protons, most of the dose is delivered to the target, sparing the surrounding tissues while photons instead deposit dose along their entire path.

Since the protons LET is very high in correspondence of the Bragg peak, it is often avoided placing the Bragg curve at the edge of organs at risk (OARs) because of range uncertainties often resulting in non-optimal treatment plans[1]. When treating tumours near critical organs, another proton beam characteristics is exploited: the sharper proton beam penumbra[9].

The first proton treatment was carried at the Lawrence Berkeley Laboratory (LBL) in 1954, and in the following 3 years, 30 patients were treated. In the 1960s, the facilities pioneer in proton therapy were LBL, the Gustav Werner Institute, in Uppsala (Sweden), where the first patient was treated in 1957 and the Massachusetts General Hospital (MGH). MGH in collaboration with the Harvard University Cyclotron Laboratory (HCL) treated 9116 patients between 1961 and 2002[1,8,11]. In the following decades, proton therapy began at several research institutions around the world (Russia, Japan, Switzerland, France, UK, South Africa, etc.) but only in 1990 the first hospital-based facility was opened at Loma Linda University Medical Centre (LLUMC), in California[12]. Currently there are 58 clinical proton center operating worldwide: 19 in North America, 21 in Europe, 1 in Africa, 17 in

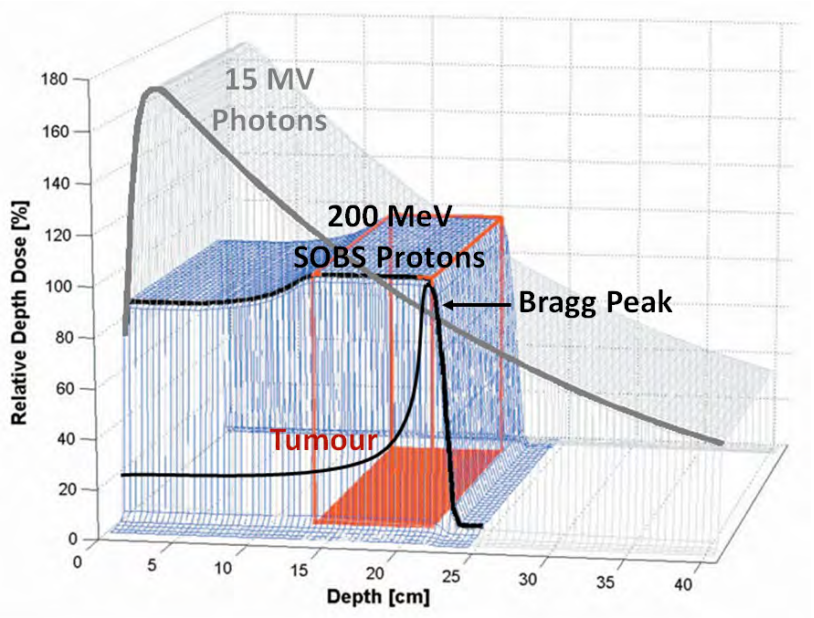

Figure 2.1: Depth vs dose curve for photons and protons. The orange parallelepiped represents the tumour (target volume) while the area below the curves is the integral dose deposited by photons (grey) and protons (blue). The plot is normalized to the dose desired in the target. The SOBP is produced by a modulated proton beam. Image taken from[10]

Asia[13].

Proton therapy has been proven to be very effective for several types of cancer. Tumours of the central nervous system, cervical carcinoma and head & neck cancers are good candidates for proton treatment because of their proximity to radiosensitive organs and for their radioresistance. In the 90's the use of protons to treat prostate cancer started to be investigated too but it still not clear whether it is advantageous to use protons for prostate[14]. Many studies were conducted to compare conventional photon radiotherapy therapy, intensity modulated radiation therapy (IMRT) and proton therapy. Fig. 2.2 shows the dosimetric advantage of proton therapy in sparing the surrounding healthy tissues during the treatment. This characteristic makes proton therapy particularly suitable to treat paediatric tumour since it decreases the probability of secondary cancers compared to conventional radiotherapy[15][16]. An extensive review of the radiation induced cancers is presented in[17]. An interesting work was conducted by Chung et al.[18] where 558 patients were retrospectively

studied comparing the risk of secondary cancer after receiving proton and x-ray therapy: 29 proton patients (5.2%) vs 42 photon patients (7.5%) were effected by second malignancies.

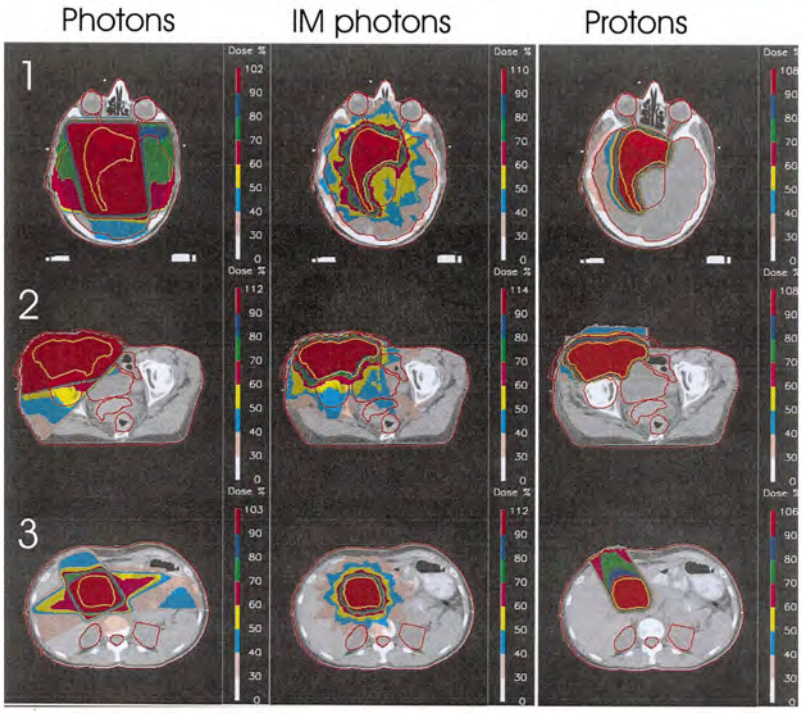

Figure 2.2: Comparison of dose delivered with conventional radiotherapy (photons), IMRT and proton therapy in a (1) meningioma, (2) malignant melanoma and (3) Klatskin tumour. Colour bands indicate the correspondent dose delivered. Image taken from[19].

2.2 From proton therapy to proton computed tomography

Proton therapy effectiveness strongly depends on the accuracy and precision of both the treatment planning and the proton beam delivery. Nowadays, for both photons and protons therapy the patient treatment is based on xCT images, which consist of a map of Hounsfield (HU) values:

$$HU = 1000 \cdot \left(\frac{\mu - \mu_{water}}{\mu_{water} - \mu_{air}} \right) \tag{2.1}$$

where μ is the average linear attenuation coefficient in a voxel, μ_{air} and μ_{water} are the

linear attenuation coefficients of air and water, respectively

Each xCT scanner is characterised by its own calibration curve used to convert the HU values into electron density of known materials with an acceptable accuracy. For proton therapy purposes, a map of the proton RSP is although necessary. The RSP corresponds to the stopping power (SP) of a specific material relative to water:

$$RSP = \frac{SP_{material}}{SP_{water}} \tag{2.2}$$

In order to get a RSP map from a xCT image, both theoretical and experimental approaches were investigated. The theoretical relationship between RSP (or SP) and attenuation coefficient (or HU values) was studied in the past[20] but the formulation was not simple and the accuracy of the result was not clinically acceptable ($\pm 5\%$). The main problem in establishing a relationship between RSP and HU is the different dependence on Z and Z/A of protons and photons, resulting into a non-unique correspondence between RSP and HU that causes uncertainties in the proton range estimation. Therefore, two experimental approaches are currently used to correlate HU values and RSP, (1) the stoichiometric method[21] and (2) the polybinary calibration[22], with proton range uncertainties around $1-3\%$. Yang et al.[23] conducted a study on how the use of the stoichiometric method effected the RSP estimation and range uncertainties in proton therapy planning. The sources of error for the RSP were classified into five independent categories:

1. uncertainties from CT imaging;
2. uncertainties in the stoichiometric formula used to calculate theoretical CT numbers;
3. uncertainties in the human tissue composition (different from the ICRU standard tissue[24]);
4. uncertainties in the mean excitation energies used in the Bethe-Bloch equation;

5. uncertainties due to RSP proton energy dependence not taken into account by dose algorithms.

The uncertainties calculated are obviously more critical for heterogeneous organs than homogeneous tissues because of the increase of proton scattering. Dose perturbation and Bragg peak degradation are typical problems encountered at the interface between two materials of different scattering powers, i.e. bone and soft tissue[1].

Different approaches are under investigation to get the patient RSP map reducing the sources of uncertainties. In primis, dual energy CT (DECT) has shown promising results in the reduction of the range uncertainties in heterogeneous tissues[23] as proved also in the comparative study between single energy CT (SECT) and DECT recently conducted by Hudobivnik et al.[25]. Unfortunately DECT still relies on patients' CT images, therefore uncertainties and artefacts effect the electron density and atomic number calculation[23].

It is evident that a direct determination of the RSP is the ideal way to proceed. This is where pCT plays an important role in medical physics and imaging: it allows a direct calculation of the RSP from proton energy loss measurements, for more accurate proton therapy treatment planning.

2.3 Proton computed tomography: historical overview

PCT is a promising imaging technique that started to be studied in the 60's. Allan Corkmack in 1963 proposed to use the energy loss of charged particles in the matter to determine the variable density of matter with constant chemical composition[26,27]. In 1968 Koehler[28] presented the first example of use of energetic protons for radiographic purposes at Harvard cyclotron. Five years later, he compared proton radiographs and x-radiographs of human tissues with tumours[28,29] proving that the image contrast with protons was higher than with photons.

The promising results encouraged the use of protons for imaging in the following decades. While Moffet et al.[30,31] kept investigating proton radiography, in 1972 the first heavy particle tomographical reconstruction was performed by Goiten in 1972[32] at LBL Cyclotron. Goiten reconstructed images of a few phantoms from alpha particles data using an iterative reconstruction algorithm: the phantoms were scanned with 41 translations and 19 view angles using a 840 MeV alpha beam at LBL (Fig. 2.3). Goitein conducted a complete study on the quality of the image reconstruction, in particular he focused on image resolution, measurement accuracy, imaging artifacts and ideal scanning angle range. His study was very important because for the first time an iterative relaxation technique was used for tomographic imaging and the resolution achievable using heavy particles was studied in detail.

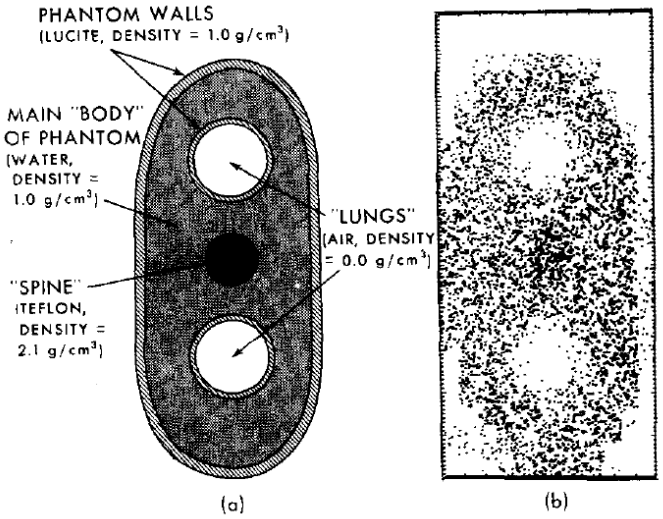

Figure 2.3: (a) Schematic representation of the phantom scanned by Lyman with 840 MeV alpha particles at the LBL cyclotron. (b) Reconstruction of the phantom performed by Goitein. Image taken from[32].

Three years later, in 1975, Cormak and Koehler conducted the first study on the use of protons for tomography[33].

They irradiated a circularly symmetrical phantom made of Lucite and sugar solutions with 158 MeV protons at the Harvard cyclotron. They concluded that proton tomography could distinguish density differences up to 0.5% and they noticed that the change in MCS at interfaces between different materials effected the measurements. The residual energy of

protons traversing the phantom was measured using two sodium iodide scintillation counters with diametre 3.81 cm and thickness 2.54 cm, mounted on photomultipliers tube.

Proton tomography was extensively investigated at the Los Alamos Meson Physics Facility (LAMPF) in New Mexico by Hanson et al. in the late 1970s and early 1980s. In 1978 and 1979 a 29 cm and a 19 cm diametre phantom were scanned with 240 MeV and 192 MeV protons, respectively. The phantoms had inserts of different material and density and were both reconstructed using a filtered backprojections (FBP) algorithm[34,35]. An hyperpure germanium (HPGe) detector was used to measure the proton residual energy and 360 projections were collected in the full rotation scan (1 degree step angle). The same phantoms were also scanned with an x-ray EMI 5005 CT scanner to compare the results. Hanson et al. concluded that that using protons the dose delivered is lower, the beam hardening artifacts are absent and that a pCT scan can be relatively fast. On the other hand the technology necessary to have proton beams of sufficient energy is expensive and more complicated than photons and the image resolution is strongly effected by MCS. In 1981 Hanson et al. demonstrated the dosimetric advantage of pCT[36] and did the first pCT scan of humans organs[37]. They scanned and reconstructed an adult hearth specimen and a normal fresh adult brain using the same method adopted in[34,35]. In this experiment the proton energy varied from 224 to 236 MeV and a range telescope was used to record the proton residual energy.

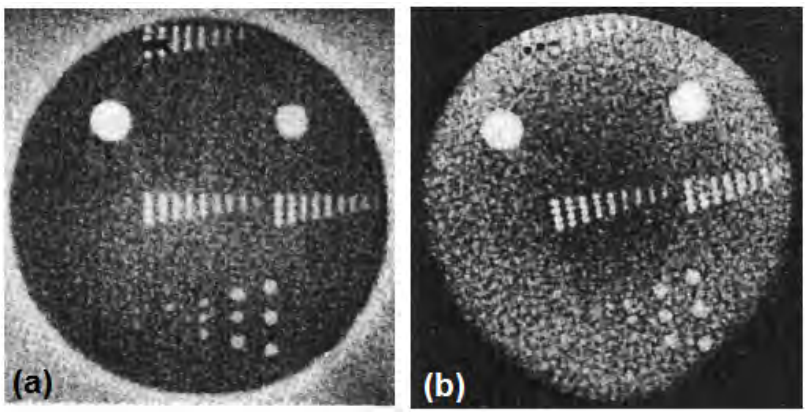

Figure 2.4: Comparison between pCT reconstruction (a) and xCT reconstruction (b) of a 29 cm phantom performed by Hanson et al. Image taken from[34].

The contribution of the LAMPF group was determinant for spreading worldwide the validity of pCT as an imaging technique. Unfortunately Hanson himself recognized that the technology available in the 1980s was not sufficient to fully exploit the potential of pCT. A decade later, in 1994, at the Paul Scherrer Institute (PSI) in Switzerland, Schneider and Pedroni started investigating the possibility of using proton radiography as a control tool for the HU-RSP calibration curve in proton therapy[38]. With proton radiography, the range uncertainty was improved up to a factor of 2.5, i.e. approximately 1 mm of error range.

Ten years later, Schneider et al. performed the first proton radiography on an animal patient (a dog) to prove the dosimetric advantages of proton radiography[39]. It was proven that the dose delivered using protons was 50 to 100 times lower than the one necessary to obtain a comparable image using x-rays.

At the end of the 20th century, the first cone beam pCT system was developed at the HCL aiming at using the reconstructed images in proton therapy treatment planning. A 160 MeV proton beam was scattered with a modifier to produce a proton cone beam that irradiated a phantom. The residual energy of protons was measured with a gadolinium oxysulfide scintillator screen viewed by a cooled charged-coupled device (CCD). The 3D proton RSP map was performed using the Feldkamp-Davis-Kress (FDK) algorithm[40], the cone beam version of the FBP. The results published by Zygmanski et al. in 1999[41] showed that the RSP values directly calculated with pCT were in better agreement with the real phantom values than then one indirectly calculated converting xCT values into RSPs. On the other hand, the spatial resolution was very poor, mostly because of the MCS.

2.4 Proton computed tomography: current status

Currently, several prototypes of proton radiography and tomography scanners are present all over the world. Focusing on pCT, based on the published material, seven groups of research are working on pCT scanner prototypes, 2 in America, 3 in Europe, and 1 in Asia. All the

existing prototypes consist of two main components, (1) a proton tracking system and (2) a residual energy detector. The scanned objects are placed at the centre (isocentre) between front and rear tracking planes and rotates along the vertical axis.

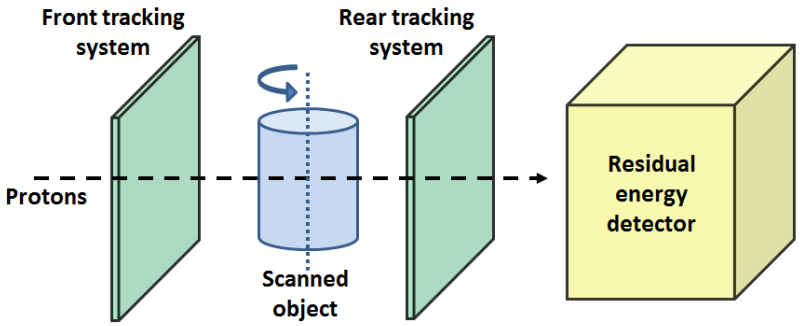

Figure 2.5: Schematic representation of the pCT scanner prototypes components; proton tracking system (in green), residual energy detector (in yellow) and scanned object (in blue).

In 2007, based on the original design concept presented in[42] , the first pCT scanner prototype was built by a collaboration started in 2003 including the University of California Santa Cruz (UCSC), the Loma Linda University (LLU) and the Northern Illinois University (NIU). Individual protons are tracked before entering and after exiting the phantom or patient with 2D-sensitive silicon trackers. Each tracking module consists of two planes of paired silicon strip detectors (SSD) with orthogonally arranged strip orientation[3,42]. The strip pich was 194 μm and the thickness was 400 μm. The sensitive area of each SSD was 6.4×6.4 cm^2. The proton residual energy was measured with a thallium doped caesium iodide CsI(Tl) crystal scintillator. The covered area was 6.4×6.4 cm^2, thus matching the SSD area and stopping 115 MeV protons. This scanner is known as the phase 0 pCT scanner and was used to conduct some preliminary pCT experiments[10]. It was limited by the number of available SSDs that did not allow to cover a big area and by the system acquisition rate which was approximately 10 kHz.

A few years later, in 2010, a second pCT prototype was built by the same collaboration. Each tracking module consisted of four planes of paired (coupled) SSD with orthogonal strips[3,42]. The strip pich was 228 μm and the thickness was 400 μm. The sensitive area of

each SSD was 9×9 cm^2; they were combined two by two to cover an area of 9×18 cm^2. The proton residual energy was still measured with a segmented array of thallium doped caesium iodide CsI(Tl) crystal calorimeter. Eighteen CsI crystals were combined to form a 3×6 rectangular matrix covering a total area of approximately 10.2×20.4 cm^2 [43]. This system operated at a maximum proton rate of 20 kHz, effecting the speed of the CT scan ($\sim$ 20 hours for a full scan of 90 projections at 4° interval). This scanner is known as the phase I pCT scanner and the schematic representation of the scanner geometry is shown in Fig. 2.6.

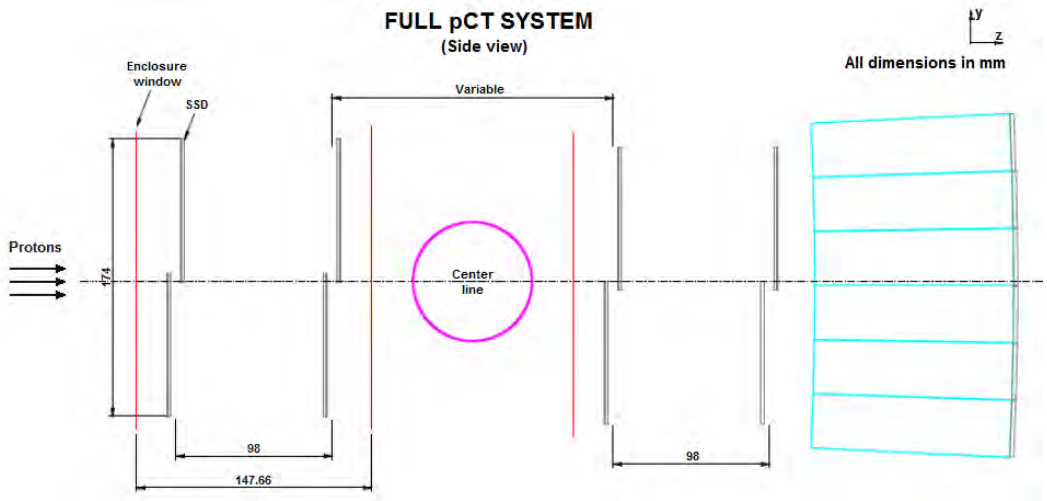

Figure 2.6: Schematic representation of the phase I pCT scanner. Image taken from [10].

In 2013 a new pCT scanner (phase II pCT scanner) was built by the pCT collaboration formed by LLU and UCSC. The tracking system consists of the same type of SSDs but the total sensitive area is double (9×36 cm^2)[44]. The residual energy is measured with a five stage scintillating energy detector[45] and the event rate is increased to 2 MHz. The phase II pCT scanner is described in detail in chapter 3 and its modelling, characterisation and guidelines for its improvement is the subject of this thesis.

NIU continued the work started with LLU and UCSC estabilishing a new collaboration with Fermilab National Accelerator Laboratory (FNAL) in 2011, when they started building a pCT scanner prototype. Individual protons are tracked with 2D-sensitive fiber trackers:

four planes of paired scintillating fibres (Sci-Fi) retrieve x and y coordinates of the protons covering an area of approximately 20×24 cm^2 [46,47]. A calorimeter stack made of 96 scintillating polyvinyltoluene is used to measure the residual energy of protons. The area covered by each tile is 27×36 cm^2 and their thickness is 3.2 mm. This system is built to operate at an event rate of 2 MHz or faster.

In 2007 the PRIMA (PRoton IMAging) Italian collaboration started the development of a prototype pCT scanner[48–50] . The proton tracking system consists of four planes of silicon microstrip detectors with a sensitive area of approximately 5×5 cm^2. Four yttrium aluminum garnet activated by cerium (YAG:Ce) scintillating crystals collect the proton residual energy. The area and depth of each crystal is 3×3 cm^2 and 10 cm, respectively and the system event rate is 10 kHz. The PRIMA pCT system was characterized both with 62 MeV protons and with 180 MeV protons[51–53] at the Laboratori Nazionali del Sud (LSN, Italy) and at Svedberg Laboratory (Sweden). A second generation pCT scanner will be built by the PRIMA collaboration[54] with a larger sensitive area (5×20 cm^2), 14 YAG:Ce crystals covering an area of 6×21 cm^2, and 1 MHz event rate.

Another Italian group, the Instituto Nazionale di Fisica Nucleare (INFN), in 2013 started the PREDATE experiment (Particle Residual Energy And Tracker Enhancement) aiming at developing a real time imaging and tracking system. Four couples of 400 FT, with 500 $\mu\mathrm{m}$ square section, orthogonally placed, covering a sensitive area of 20×20 cm^2 are used for tracking the particles with a spatial resolution of about $\mu\mathrm{m}$[55,56]. Sixty polystyrene layers of Sci-Fi, 500 $\mu\mathrm{m}$ thick, covering an area of 4×4 cm^2 are used to measure the particle residual energy. The system was tested and characterised at the LSN facility but no image reconstruction has been done yet. The use of FT both for tracking and residual energy system theoretically allows for high rates event acquisition (up to 10 MHz, currently 1 MHz)[46].

In 2013, the Proton Radiotherapy Verification and Dosimetry Application (PRaVDA) Consortium started developing a new pCT system, fully based on solid state components[57].

Individual protons are tracked before and after the phantom or patient with silicon microstrip sensors (Micron Semiconductor Ltd, 150 μm) covering an active area of 9.3×9.6 cm^2 [58,59]. Differently from all the systems previously described, each tracking module consists of three detectors planes. The detectors are positioned at a 60° angle with respect to each other to precisely measure the proton hit coordinates as shown in Fig. 2.7. Twenty-four CMOS Active Pixel Sensors (APS) stacked are used to measure the residual proton energy, covering an area of 12.8×12.8 cm^2 [60]. The event rate of the system is 1 MHz.

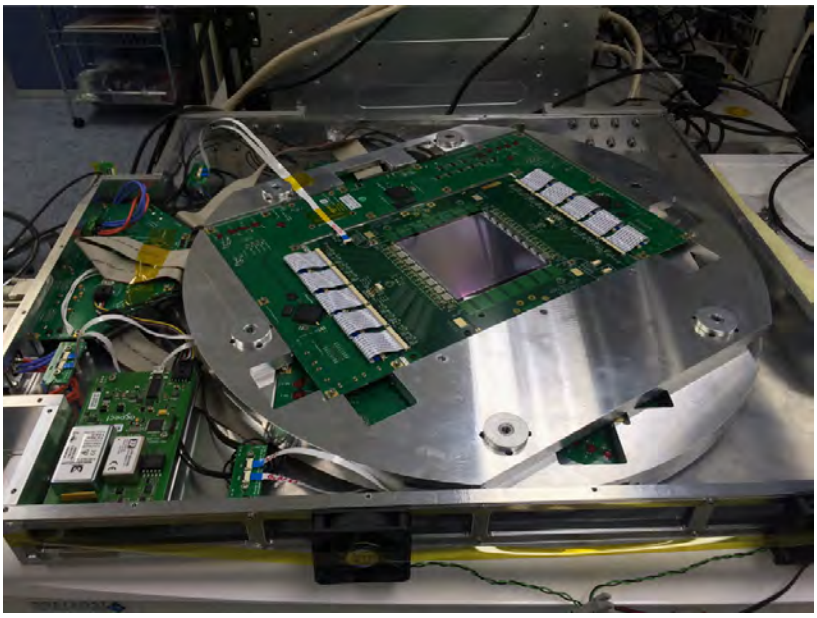

Figure 2.7: Setup of the tracking module of the PRaVDA pCT system. Image taken from [58].

One of the most active country for proton and heavy ion therapy is Japan, as proven by the fact that currently in Asia 14 out of 17 proton therapy facilities are in Japan. The interest in pCT in Japan started in the 1980s, when Akisada published an article describing a conceptual prototype of a pCT system [61].

At Niigata University a complete pCT prototype was developed in 2013 [62]. Single-sided silicon strip detector covering an area of 9×9 cm^2 were used to track the protons and their residual energy was measured with a calorimeter made of NaI(Tl) crystals. This pCT system is based on the LLU-NIU-UCSC phase I pCT scanner previously described. the rate of this

system is very low (30 Hz) due to DAQ limitations. In 2014, at the same university a high rate silicon tracker for pCT was designed[63].

In 2016, a collaboration between Tokyo and Hiroshima university developed an innovative pCT imaging system. The system consists of a CCD camera facing the beam acquiring a 2D image and a $20\times20\times5\mathrm{cm}^3$ plastic scintillator collecting the proton residual energy[64].

A summary of the features of the pCT systems mentioned in this section is listed in Table 2.1.

Table 2.1: Summary of the features of the currently existing pCT scanners.

Group	Country	Year (time frame)	Tracking system	Area [cm^2]	Residual energy detector	Acquisition rate
UCSC - LLU NIU	USA	2003-2007	2 planes x-y SSDs	6.4×6.4	CsI(Tl) calorimeter	10 kHz
UCSC - LLU NIU	USA	2007-2010	4 planes x-y SSDs	9×18	CsI(Tl) calorimeter	20 kHz
UCSC - LLU	USA	2010-2013	4 planes x-y SSDs	9×36	Plastic scintillator	2 MHz
NIU FNAL	USA	2011-2014	4 planes Sci-Fi	20×24	Plastic scintillator	2 MHz
PRIMA	Italy	2007-2014	4 planes x-y SSDs	5×5	YAG:Ce calorimeter	10 kHz
PREDATE INFN	Italy	2013-2014	4 couples Sci-Fi	20×20	Sci-Fi	1 MHz
PRaVDA	UK	2013-2015	x-y-z SSDs	9.3×9.6	CMOS APS	1 MHz
Niigata University	Japan	2013-2014	4 planes x-y SSDs	9×9	NaI(Tl) calorimeter	30 Hz
Tokyo-Hiroshima University	Japan	2014-2016	CCD camera	10×10	Plastic scintillator	-

2.5 Limitation in proton computed tomography

PCT is still not clinically available after more than 50 years of scientific investigation because of several limitations that still need to be overcome. Density and spatial resolution present some physical limitations in pCT but also the economic aspect plays a big role in the pCT clinical development.

2.5.1 Physical limitation

Protons travelling in a medium lose energy through[1,65]:

1. electromagnetic interactions with electrons and nuclei, causing erratic changes in protons direction;

2. nuclear interactions with nuclei, generating secondary particles.

Nuclear interactions are not very frequent and, above all, do not give any contribution to pCT image reconstruction while energy loss and scatter of protons traversing a phantom or a patient (angular and lateral scatter) are the two main physical processes observed for proton imaging.

2.5.1.1 Scattering

Protons are subjected to small multiple angular and lateral deflection when traversing a medium because of the electromagnetic interactions with the atomic nuclei of the material traversed[66]. The contribution of all the small angular and lateral deflections are nearly Gaussian distributed (as expected from the Central Limit Theorem). The central part of the distribution is Gaussian but a single scattering tail is present due to the large single scatters in the medium that sometime can cause differences of few mm between entry and exit position.

MCS is one of the main limiting factor for pCT spatial resolution[67,68]. It was proven that a good estimation of the proton path is fundamental to increase the spatial resolution. In this PhD thesis, a specific algorithm was used to calculate the MLP[6] for protons in pCT. The effect of heterogeneities in the proton path estimation was investigated in chapter 7.

2.5.1.2 Stopping

The relevant energy range for pCT is between 100-250 MeV[69]. In this range of energies, protons mainly lose their energy by ionizations and atomic excitation, while density effect

and shell correction are negligible[70–72]. This behaviour is well described by the Bethe-Bloch stopping power formula for protons:

$$-\frac{dE}{dx}(E,r) = \frac{4\pi}{m_e c^2}\frac{\eta(r)}{\beta^2(E)}\left(\frac{e^2}{4\pi\epsilon_0}\right)^2\left[ln\left(\frac{2m_e c^2}{I(r)}\frac{\beta^2(E)}{1-\beta^2(E)}\right)-\beta^2(E)\right] \tag{2.3}$$

E and r are the proton energy and location, respectively. β is the proton velocity relative to the speed of light c, m_e is the electron mass, e is the electron charge, ϵ_0 is the electric constant, and I is the mean excitation potential of the medium. η, the electron density, can be calculated as follow:

$$\eta_e = \rho N_A\left(\frac{Z_e}{A_e}\right) \tag{2.4}$$

where N_A is Avogadro's number, Z_e and A_e are the effective atomic number and weight of the medium, respectively.

For protons with the same initial energy, the stopping location will not be the same because protons are effected by fluctuations in their energy loss and consequently, in their range. This phenomenon is known as energy straggling or range straggling and it is a limiting factor in pCT because it effects pCT density resolution[73].

2.5.1.3 Nuclear Interactions

Protons can interact inelastically with the atomic nuclei of a target when they have energies that can overcome the Coulomb barriers of the nuclei. The nuclei are transformed irreversibility and secondary particles such as neutrons, protons or heavier ions may be emitted.

Secondary particles are very important when using high energy protons for cancer treatments because they affect spatial and absorbed dose distribution in patients[74,75]. It has been calculated, for example, that for 200 MeV protons the secondary particle contribution

to dose is about 10% at 20 cm of water depth[69].

The inelastic cross section of biologic materials for proton nuclear interaction is characterised by a threshold of about 10 MeV, a peak at about 20 MeV, and a drop to approximately half of the maximum value at about 100 MeV[65,76]. Given that the proton energy range for pCT is between 100-250 MeV[69], the nuclear interaction contribution to pCT is negligible.

2.5.2 Economical limitation

The clinical use of pCT is strongly affected by the costs of medical facilities using protons for treatment purposes. The easiest solution would be to use proton accelerators and beam transport systems already used for proton therapy treatments. Unfortunately, even though many proton-based facilities have been opened in the last 20 years, proton therapy widespread adoption is not as fast as for photon therapy. This is mainly due to construction problems (size of accelerators and beam delivery system required), running costs and lack of evidence of cost-competitiveness and cost-effectiveness[10,65]. The cost of a proton treatment was estimated to be approximately double the cost of a photon treatment[77].

Some of the advantages of proton therapy were discussed in section 2.1. However, from an economical point of view, more proofs of the effectiveness of proton therapy over IMRT are required. Several studies have been published on this topic[78–80]. It was concluded that the number of randomized control trials (RTCs) on proton therapy is currently not enough, even if the ones conducted are very promising.

It is expected that the research conducted in all the new proton facilities worldwide will bring new solutions to reduce the proton therapy and facilities costs, therefore making a step forward for the pCT clinical implementation.

2.6 Conclusions

Proton therapy is a radiation modality alternative to conventional photon or electron therapy used primarily because proton beams allow delivering high doses to tumours (localised targets) while sparing the surrounding healthy tissues. For this particular reason, proton therapy is particularly indicated for head & neck cancer, brain and paediatric tumours. To fully exploit the advantages of proton therapy, an accurate prediction of the proton range is crucial. Currently, xCT images are used for proton treatment planning: CT numbers are converted into RSP values leading up to 3% uncertainty in the proton range estimation[81].

PCT is an imaging technique that allows the direct calculation of the RSP. Knowing the energy lost by protons traversing the patient, pCT provides a 3D RSP map that can be used for treatment planning, reducing the proton range uncertainty to 1% or less. Moreover, the dose delivered to a patient during a complete pCT scan is about 50 times less than with x-ray CT.

PCT is still not ready to be clinically implemented but a few pCT scanner prototypes are currently used by several research groups all over the world to investigate and improve different aspects of pCT.

This PhD thesis aims at studying a second generation pCT scanner system build in 2013 by a collaboration between LLU and UCSC. Specifically:

- Monte Carlo methods are used to model the LLU/UCSC pCT scanner prototype;
- the effects of heterogeneities in the image reconstruction are studied using a pixelated dector (Medipix);
- the dosimetric advantages of using pCT over cone beam CT are investigated both using simulated and experimental data.

The final goal is to model and investigate as many aspects of pCT as possible in order to make a step forward towards the clinical implementation of this imaging technique. Proton

imaging has a great potential; its success is strongly linked to proton therapy treatments and depends on the current progress of the ongoing research.

Chapter 3

The Phase II pCT Scanner Prototype

3.1 Introduction

A brief summary of the pCT prototypes scanners available all over the world was presented in section 2.4. In particular, the phase 0 and phase I pCT scanner built by the pCT collaboration in 2007 and 2010, respectively, were described. The pCT collaboration between LLU and UCSC started in 2003 and the latest pCT scanner prototype build in 2013 (phase II pCT scanner) is the main subject of this PhD thesis.

3.2 Phase II pCT scanner

Fig. 3.1 shows the phase II pCT scanner prototype, in all its components. The development of this scanner has been described previously[42] [3]. Individual protons with energy of 170-250 MeV are tracked with 2D-sensitive silicon trackers before entering and after exiting the phantom. In addition, the residual energy of protons is measured with a multi-stage scintillator detector, currently comprised of 5 individual scintillators with photomultiplier readout. In chapter 5, a more detailed description of the individual components of the pCT scanner will be given.

The scanner has been tested both at the synchrotron at LLUMC and at the cyclotron at the Northwestern Medicine Chicago Proton Center (NMCPC - Warrenville, IL).

The Loma Linda beam line is described in[12]. The proton beam exits after passing through five 12.7 mm thick aluminum foils, representing the secondary-electron emission monitor (SEM) detectors integrated in the distal end of the vacuum pipe. A lead foil of 1.9 mm thickness was placed immediately after the SEM exit window to scatter the beam at the entrance of the front tracker. The beam energy is 200 MeV.

The NMCPC beamline consists of a 230 MeV scanning beam degraded in order to reach an energy of 200 MeV. The proton beam covers an area of approximately 4×4 cm^2 and Wobbler magnets are used to select the adequate scanning field of interest.

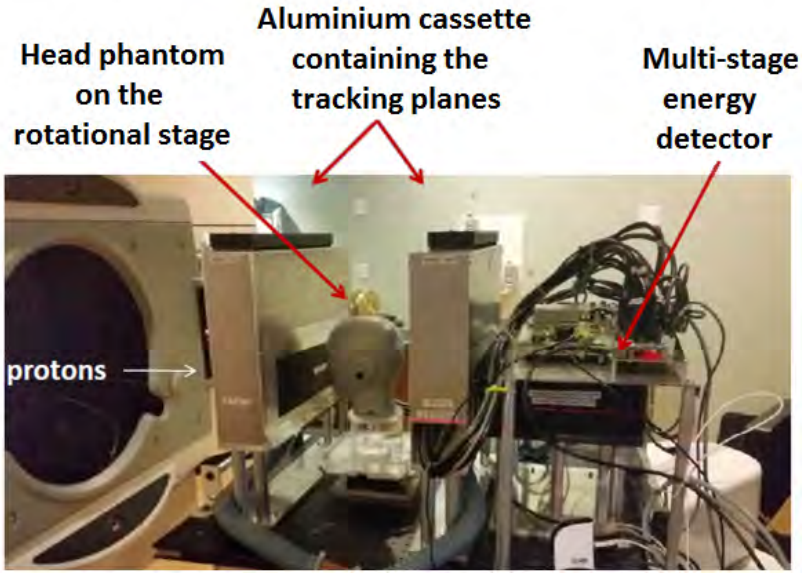

Figure 3.1: The prototype pCT scanner mounted on a beam line of the Northwester Medicine Chicago Proton Centre.

3.3 Tracking Detector

The front and rear trackers consist of two paired silicon strip detector planes with vertical and horizontal strip orientation, respectively[4]. The silicon strip sensors were originally

custom-designed for the NASA Fermi large-area gamma ray telescope (Fermi-LAT, now in orbit) and manufactured by Hamamatsu Photonics (Japan). The trackers and associated electronics are housed in an aluminium cassette. The front and rear trackers are positioned symmetrically with respect to the scanner isocenter, which is defined as the intersection of the phantom rotation platform and the central axis of the detector system on which the proton beam is centred, as shown in Fig. 3.1.

Silicon strip detectors were selected for tracking protons because of several advantages:

- high performance - SSDs efficiency is nearly 100% for charged particles detection and the noise occupancy is almost zero;
- high reliability and stability - the SSDs calibration is simple and stable for many years;
- easy to assemble - SSDs are compact and can be assembled using conventional industrial processes, guaranteeing an excellent mechanical stability;
- high spatial resolution.

Each tracker plane consists of four square SSDs with individual sensitive areas of 8.6 $\times$ 8.6 cm^2, which form a total sensitive area of 34.9 $\times$ 8.6 cm^2 per plane, including the submillimetre gaps between SSDs. The thickness of each SSD is 0.4 mm, and the strip pitch is 0.228 mm. The tracker plane with vertical strips (t-plane) is formed by 1536 strips and the plane with horizontal strips (v-plane) by 384 strips. The gaps between the adjacent SSDs were minimized, sawing the edges next to the guard ring. The final gaps were approximately 0.6 mm wide. The gaps are not superposed (small offset) in different tracking planes in order to minimize the probability for protons to go through more than one gap. Protons tracks can be reconstructed both using 8 hits (complete track reconstruction) or using 7 hits recovering the missing hit as described in section[82].

When a proton intersects the paired detector planes, the t-plane electronics retrieve the horizontal hit coordinate while the v-plane retrieves the vertical hit coordinate. The applica-

tion specific integrated circuit (ASIC) chips of the tracker plane readout electronics handle 64 consecutive strips per chip, and the data are processed by 12 FPGAs (1 per v-plane and 2 per t-plane) mounted on the same circuit boards that carry the SSDs[44]. This will be described more accurately in section 3.5.

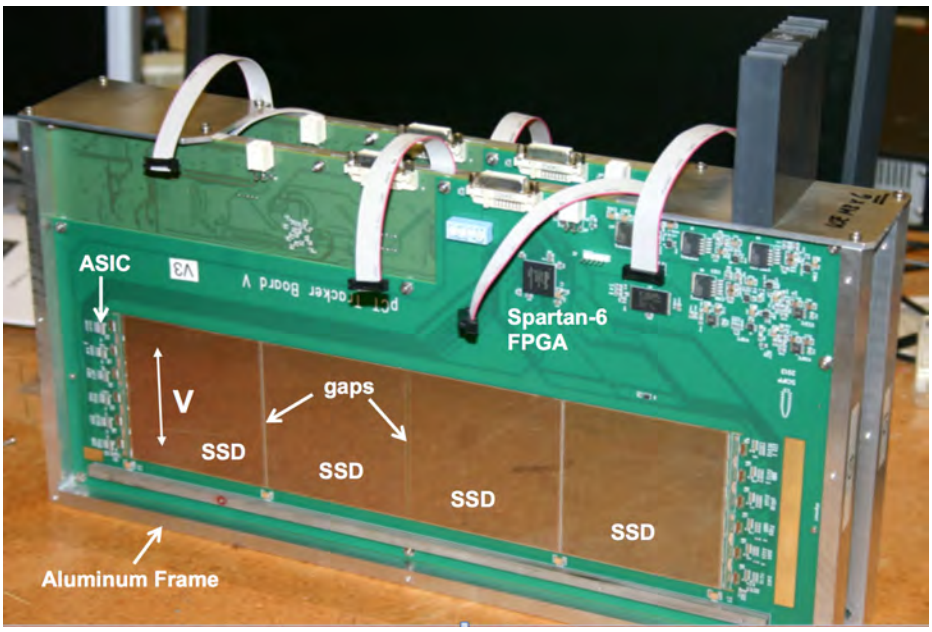

Figure 3.2: Tracking module with two V layers and two T layers. The strips on pairs of SSDs are wire bonded together and read out by six ASICs on either end of the board. Each V board has 12 ASICS and each T board has 24 ASICS. The loose cables visible are for programming the six Xilinx Spartan-6 FPGAs, one per V board and two per T board[83].

3.4 Residual Energy Detector

The decision of replacing the CsI(Tl) crystal array calorimeter used in the phase I pCT scanner was mainly given by the necessity of a faster system for data acquisition (high data-rate requirement). In[45] the advantages of using a multistage detector are presented. In particular, the calorimeter was found to add uncertainty to the WEPL measurement depending on the thickness of the object scanned and the calorimeter response was found to be non uniform over its sensitive area. Fig. 3.3 shows a comparison between the responses of a calorimeter and a multistage energy detector.

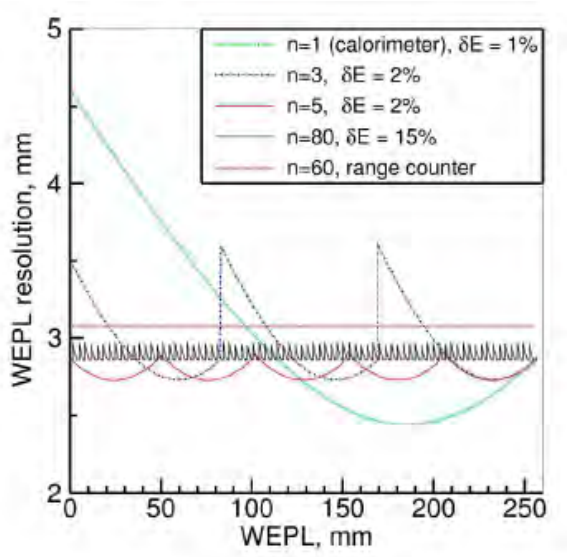

Figure 3.3: Comparison between the responses of a calorimeter (in green) and a multistage detector with n stages. Image taken from [45].

The multi-stage detector used in the phase II pCT scanner is composed of five UPS-923A polystyrene scintillators with a sensitive area of $36 \times 10\ \mathrm{cm}^2$ and a thickness of 5.1 cm (Fig. 1b). The total water equivalent thickness of the detector is 26.4 cm, which is sufficient to stop 200 MeV protons. The scintillating light of protons stopping or traversing a stage is registered by an R3318 Hamamatsu photomultiplier (PMT) attached to the top of the stage and converted to a digital value by custom readout electronics [83]. The scintillators were optically polished and optical epoxy was used to glue the PMT to the scintillators. A layer of Vikuiti™ ESR film, 65 $\mu\mathrm{m}$ thick, was used to wrap the each scintillator-PMT. Vikuiti™ ESR is a reflective material with greater than 98% reflectance. The five stages were finally enclosed in a steen housing as shown in Fig. 3.4. A detailed description of this novel type of detector and first performance results have been presented elsewhere [45].

Fig. 3.5 shows an example of the response of the multi-stage detector during five different experimental empty runs (no phantom between the tracking planes).

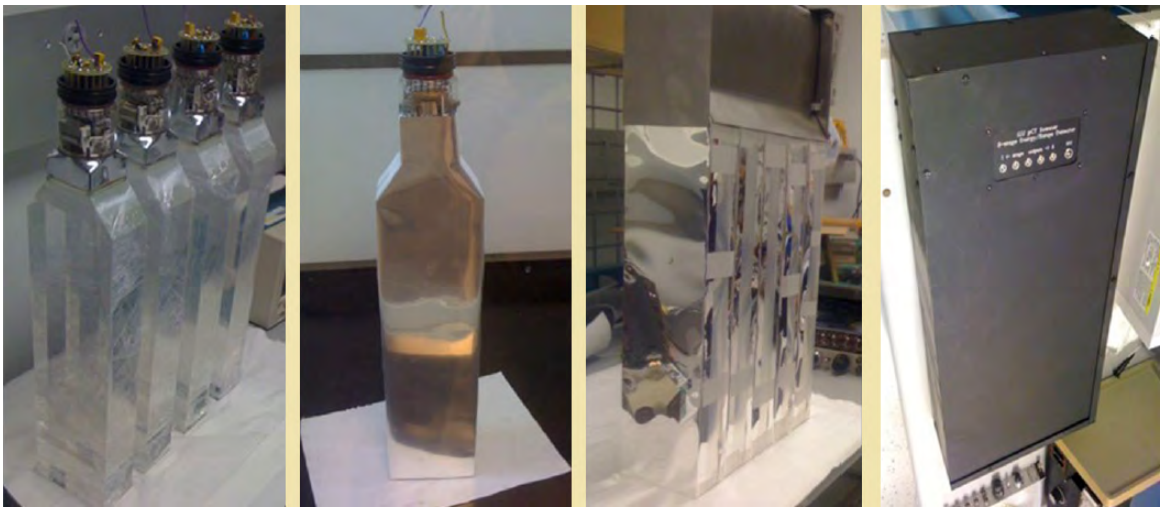

Figure 3.4: Assembly of the multi-stage detector. Image taken from [45].

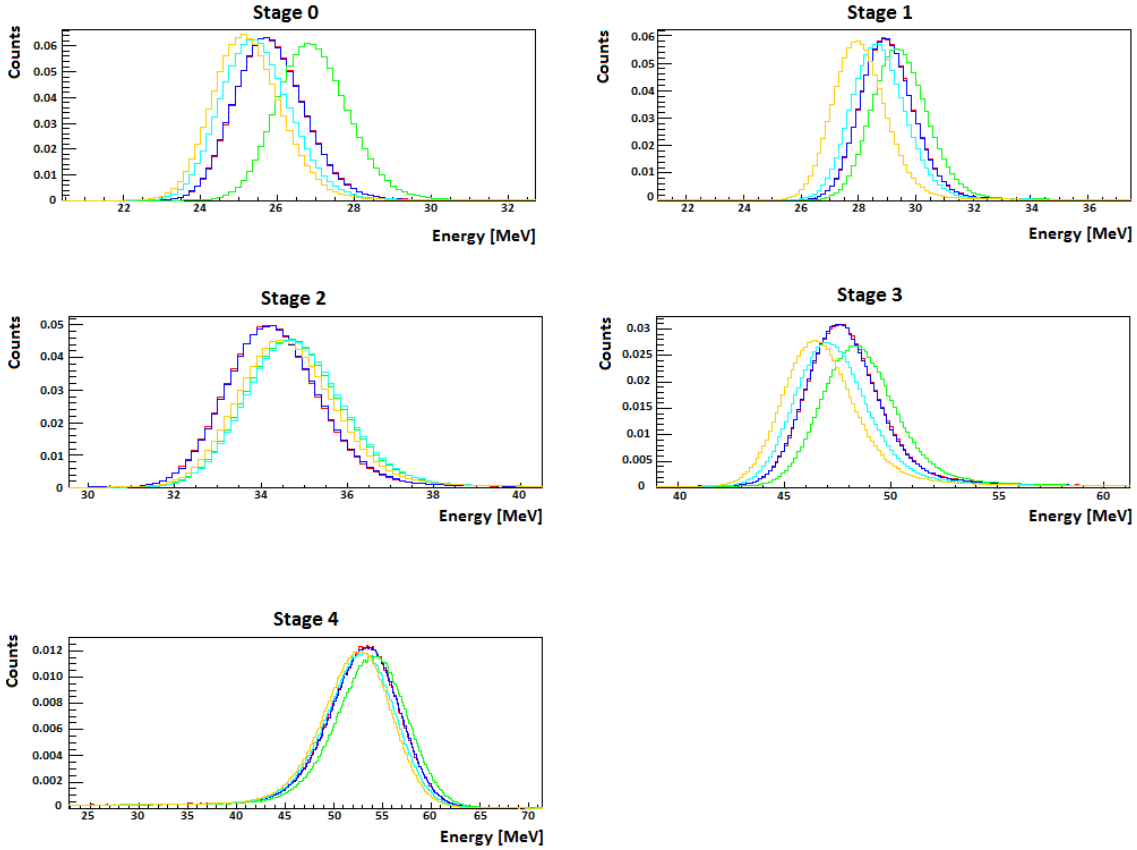

Figure 3.5: Examples of energy deposited in the five stages of the multi-stage detector during five different experimental runs. There was no phantom between the tracking planes (empty run). The distributions are not perfectly aligned due to fluctuations in the initial beam energy.

3.5 Data Read Out

The trigger of the pCT data acquisition system (DAQ) is formed by the readout-electronics of the multi-stage detector. For every proton detected by the multi-stage detector, strip number, chip number, SSD number, and FPGA number are registered. The read out of front and rear tracking detectors is performed by a unique CMOS chip, specifically designed for this purpose. The scanner can measure up to two million proton tracks per second, so it is crucial that the chip can digitize the data and send them out rapidly. Meanwhile the front-end amplifiers must be active at all times. 144 custom ASICS were used to fulfil this task, each of them handling 64 channels (one channel per strip) with a 100 Mbit/s link to an FPGA on the same board.

Twelve Spartan-6 FPGAs handle the data flow for the tracking planes, two the data flow for the energy detectors.

The PMT signals are digitised by an ADC that operates at 65 MHz and then processed and transmitted to the event builder with a custom printed board (PCB).

The complete event is built by a Xilinx Virtex-6 FPGA event builder[83] and then sent to the DAQ computer that writes all raw data to disk using custom-designed Python software. A detailed description of the read out system can be found in[44].

3.6 Preprocessing

In order to use the information collected for imaging reconstruction purposes, the raw data must be preprocessed. Specifically, the strip number needs to be converted in coordinates t and v (in mm) with respect to the isocenter and the energy needs to be converted into WEPL. These two steps will be described in sections 3.6.1 and 3.6.3, respectively. Finally, the converted data must be written in the binary format required as input for the reconstruction algorithm.

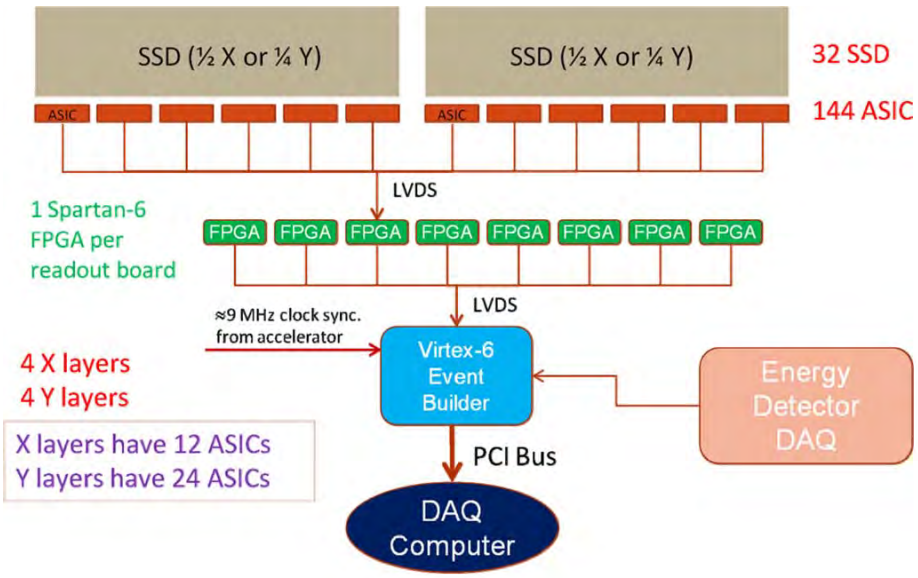

Figure 3.6: Schematic representation of the pCT data acquisition system. Image taken from[44].

3.6.1 Proton track reconstruction

A fundamental step in the preprocessing phase is the reconstruction of the proton tracks. Upstream and downstream aluminium cassettes containing the tracking planes are approximately 30 cm a part (see Fig 3.1): the protons track must be accurately reconstructed in order to associate correctly the hit in the front and rear tracking planes. Using four hits both in front and rear planes (one hit per plane) it is possible to reconstruct two dimensional tracks for all the combination of hits. A two dimensional "supertrack" is defined merging correspondent front and rear two dimensional tracks. The criteria chosen to recognise matching tracks is the displacement between them: if the displacement is less than 10 mm at the isocenter (plane $u = 0$), then the two tracks form a "supertrack". 10 mm corresponds to 12.5 standard deviations of the displacement distribution when no degrader is present. A detailed explanation of the "supertrack" recovery can be found in[82].

3.6.2 Missing Hits Recovery

It is possible that one of the four hits necessary to reconstruct the front or rear 2D track is missing. This could happen when a proton goes through the gap between the SSDs (2%) or through a dead or noisy strip (0.2%). The missing hit can be geometrically recovered knowing the position of the beam spot at the flange of the accelerator beam pipe. Using this information as the forth point, it is possible to verify if the missing hit corresponds to a gap. In this case, the coordinate of the center of the gap is manually attributed to the proton hit. This procedure is used both for front and rear trackers and the calculated spatial accuracy in recovering the missing hits are 168 μm and 290 μm, respectively.

3.6.3 Calibration

In order to convert the ADC response into WEPL, an ad-hoc calibration procedure is adopted. The calibration of the pCT scanner must be done before performing any pCT experimental measurement because it depends on beam conditions and geometrical set up.

The response of the scintillator depends on the proton path inside of the scintillator therefore it is necessary to implement a correction that takes into account the spatial dependency. The track of the protons exiting the rear trackers are extrapolated, accumulated in 0.5×0.5 cm^2 bins and averaged. A quadratic function was used to fit the 3D distribution for each stage in horizontal (T) and vertical (V) direction. From this, the name "T-V correction" was attributed to this procedure. Note that T and V are used for horizontal and vertical response as the t-planes and v-planes measure the horizontal and vertical position of the proton hit. The ADC response is then converted into MeV using a Geant4[5] model for normalising the fitting function. It was proven that this correction reduces the spatial variation to 0.4% rms deviation over almost the entire sensitive area of the detector[45].

Once the T-V correction is applied to the scintillator response, the WEPL conversion can be performed using an adequate calibration. A custom calibration phantom was built for the

pCT scanner prototype. It consists of three stepped pyramids of polystyrene (Fig. 3.7) and a variable number of polystyrene degraders with a RSP of 1.038. Each pyramid contained 8 steps of 6.35 mm physical thickness adding up to a maximum thickness of 5.08 cm. In order to cover the total range of 200 MeV protons in polystyrene (25.4 cm), the stepped pyramids are combined with a choice of 0, 1, 2, 3, or 4 polystyrene degraders placed downstream of the calibration phantom. Every degrader has a physical thickness of 5.08 cm, which is identical to the maximum thickness of the steps.

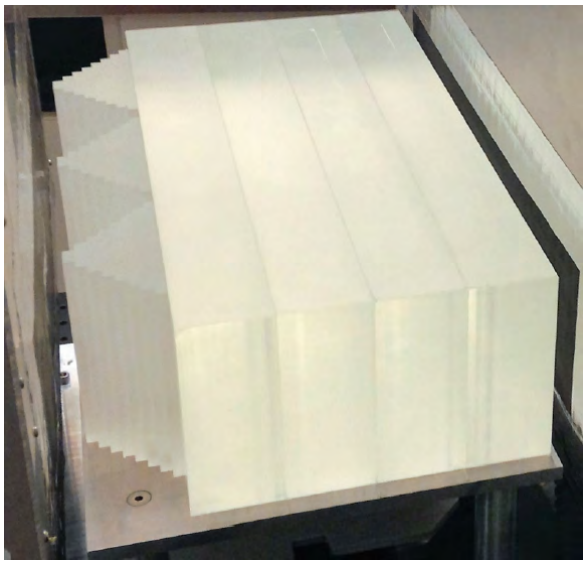

Figure 3.7: Step calibration phantom with the addition of four polystyrene degraders. Image taken from[45].

The tracking information and the knowledge of the phantom geometry allow the calculation of the protons path lengths in the object. The path length is converted into WEPL multiplying air and polystyrene path length by their corresponding RSP. For that particular WEPL, the corresponding energy detector response in each stage is recorded and the TV correction is applied.

The mean value and standard deviation of the detector response for protons stopping in each stage are calculated fitting the stage responses with Gaussian curves. The mean stopping responses in each plane are fitted with a second order polynomial function WEPL $=$ $p_0 + p_1 E + p_2 E^2$ that represents the calibration curve for each plane.

Bashkirov et al.[45] showed that the WEPL resolution achievable with this calibration is about 3 mm, regardless the traversed thickness. Range straggling and leakage of energy due to nuclear interaction in phantom and detector are the two main causes of uncertainty.

The calibration procedure will be explained in detail in chapter 5.

3.6.4 Conclusions

A prototype pCT scanner has been built and successfully tested in two beam lines. Hardware and data acquisition have been operated reliably at the design data rate in both synchrotron and isochronous-cyclotron facilities. The novel multi-stage scintillator combines elements of calorimetric measurement with proton range measurements, and we have shown that the range resolution achieved in both simulation and experiment is close to the theoretical limit. The system supports testing of reconstruction algorithms as well as a thorough evaluation of pCT in terms of image resolution, RSP measurement, spatial resolution, and dose deposition in a variety of phantoms.

Chapter 4

Development of a High-Resolution Digital Head Phantom for Simulation of New Imaging and Radiation Therapy Modalities

Development of a High Resolution Voxelised Head Phantom for Medical Physics Applications **by Giacometti V. et al.** The work presented in this chapter and partially in chapter 6 (specifically in section 6.4) was published in the Focus Issue "3rd Geant4 School and Monte Carlo Workshop for Medical Physics" in Physica Medica, 2017.

4.1 Introduction

The development of anthropomorphic phantoms, both physical and computational, is an active field of investigation in medical physics[84]. Anthropomorphic computational phantoms have undergone an evolution from simple stylized phantoms to voxelised phantoms and, more recently, to hybrid phantoms offering a mixture of surface-based and voxelised

representations[85–87]. Stylized mathematical phantoms[85], which are based on 3D surface equations for internal organs definition, provide only a rough approximation of the true anatomy of individual patients. Voxelised[86] and hybrid phantoms[87] are usually generated from CT and/or MRI data of patients or volunteers. They provide a better anatomical detail, but are frequently compromised by image noise, partial-volume averaging and imaging artefacts. Despite these drawbacks, it has been well established that voxelised phantoms can be successfully used in a wide range of medical physics applications[88–91]. In this chapter we describe the development and use of a novel high resolution voxelised head phantom, called here `HighResHead`, based on a high resolution CT acquisition of a physical paediatric head phantom (HN715, CIRS).

The `HighResHead` was initially created for pCT studies when it became clear that simple geometrical phantoms such as, for example, the Catphan ® 600 series (The Phantom Laboratory, Salem, New York, USA) were not sufficient to fully characterize pCT, but that an accurate representation of the human anatomy was necessary.

4.2 Physical Head Phantom

The `HighResHead` was created from the CT scan of a commercially available tissue-equivalent dosimetry phantom (ATOM®, Model HN715, CIRS Inc., Norfolk, VA) (Fig. 4.1a). The physical phantom provides very realistic anatomical details of the head and spine of a 5-year-old child including skeletal and soft tissue features, intra-cranial and paranasal sinuses, ear canals, and outer head contours (Fig. 4.1b). The physical phantom is composed of the following seven tissue-equivalent materials (density in g/cm^3): soft tissue (1.055), brain (1.07), paediatric spinal disc (1.10), paediatric trabecular bone (1.13), 5-year-old compact bone (1.75), tooth dentine (1.66), and tooth enamel (2.04). All materials of the real phantom are homogeneous in their density and composition; a few minor defects such as small cavities can be present, which were not included in the `HighResHead`. The proprietary

atomic composition of each material is available from CIRS upon request.

4.3 High Resolution CT scans

Eight separate helical CT scans of the entire physical head phantom were acquired with a 64-detector-row CT scanner (Lightspeed, GE Healthcare, Waukesha, WI) at LLUMC using an image matrix size of 512×512 pixels and a display FOV of 9.6 cm, corresponding to a pixel size of 0.1875 mm × 0.1875 mm. The slice thickness was 1.25 mm. The display field of views (FOVs) were partially overlapped so that each part of the phantom was covered by at least one display FOV (Fig. 4.1c). A single DICOM study with 128 slices and matrix size of 1024 × 1024 pixels was generated from the CT scan with a segmentation study performed with Matlab (The MathWorks Inc., Natick, MA, USA).

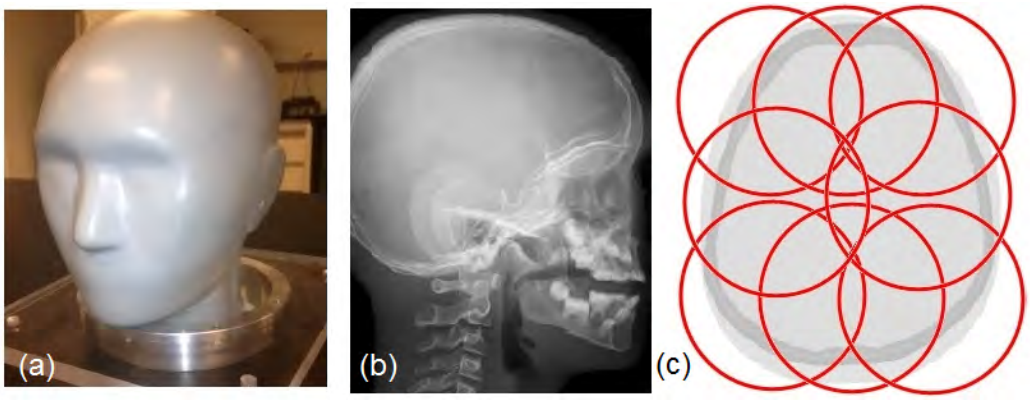

Figure 4.1: (a) Head phantom (HN715, CIRS); (b) lateral x-ray radiograph of the head phantom demonstrating its anatomical detail; (c) arrangement of eight partially overlapping FOVs represented by the red circles of 9.6cm diameter.

4.4 Segmentation of the anatomy

The different tissue regions of the phantom were segmented in each CT slice using ImageJ version 1.46r (http://imagej.nih.gov/ij). The HU values of the outer air and most of the tissue

regions were found to be well described by well-separated Gaussian distributions with mean and standard deviations listed in Table 4.1.

Step 1 The first step of the segmentation process consisted in identifying continuous boundaries between the voxelised phantom and the surrounding air, and between the different tissues of the head itself by means of a thresholding process. To detect entire tissue regions and their boundaries, different windows of HU were selected using a custom thresholding macro in ImageJ. Imperfections in the boundaries were manually edited as guided by anatomical knowledge or by the fact that they were obvious artefacts.

Step 2 The second step consisted in importing the thresholded ImageJ images in black and white in Microsoft Paint, where the different tissue regions were assigned to specific colours. Voxels which were found to deviate from their immediate neighbours in the interior of each tissue region were assigned to the tissue of the surrounding medium, thus eliminating single-voxel errors.

Step 3 The third step consisted in assigning the corresponding mean HU value, listed in Table 4.1, to the voxels of each identified tissue region, to eliminate the noise affecting the phantom. The regions with sinus, consisting of lung inhale tissue equivalent material in the physical head phantom, were assigned to the HU value of air in the `HighResHead`.

Fig. 4.2 illustrates, for a given slice, the steps from the thresholded image to the final phantom bitmap image.

4.5 `HighResHead`

After all slices were segmented as described above, the digital head phantom images were combined into a single DICOM study. A second version of the `HighResHead` (Fig. 4.3c) was created by implementing a base of skull tumour and surrounding organs at risk (OAR).

Table 4.1: Mean and standard deviation (SD) of the HU values 7 tissue-equivalent phantom materials in the HN715 phantom, ordered from lowest to highest mean value.

Material	Mean (HU)	SD (HU)
Soft tissue	24	9
Brain	52	8
Spinal disc	92	2
Trabecular bone	197	7
Cortical bone	923	107
Tooth dentin	1280	27
Tooth enamel	2310	80

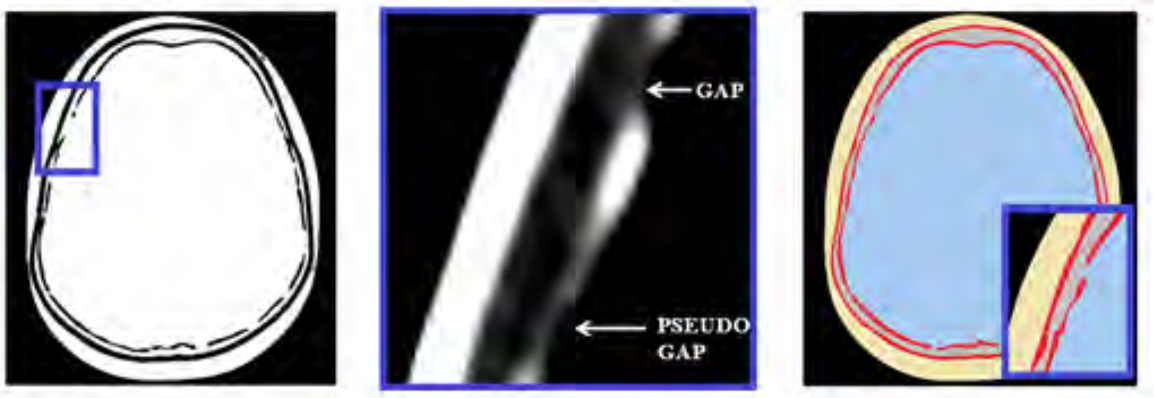

Figure 4.2: (a) Thresholded ImageJ image; (b) close-up view of the inner table with the DicomWorks viewer showing a real gap and pseudo gap; (c) final bitmap image after the segmentation process; the pseudo gap has been eliminated while the real gap has been kept. The image is noiseless. Each tissue is identified with the corresponding mean HU, as listed in Table 4.1.

In order to visualize these regions, HU values of brain +100 were assigned to tumour and brain -100 to OARs, respectively. Position, shape, size and HU value of the tumour were decided under the supervision of Dr. R. W. Schulte, who is a board-certified radiation oncologist.

Fig. 4.3 shows a slice of the x-ray CT scan of the physical head phantom, the corresponding image of the `HighResHead` and the same image with tumour and surrounding organs.

Figure 4.3: (a) xRay CT scan of the physical head phantom; (b) corresponding image of the HighResHead; (c) same image of the modified version of HighResHead with tumour and surrounding OAR.

4.6 ConvHead

Another voxelised virtual phantom, called here ConvHead, was created scanning the same physical head phantom with the same x-ray CT scanner at LLUMC using an image matrix size of 512×512 pixels and a display FOV of 37 cm, in order to cover the entire phantom with one scan. Its spatial resolution is lower than the case of the HighResHead. The pixel size and slice thickness are 0.72 mm × 0.72 mm and 1.25 mm, respectfully. 171 slices were collected in a single DICOM study.

The ConvHead was not subjected to any image segmentation process but was developed to be used as a term of comparison to quantify the effect of adopting a high spatial resolution and a noiseless virtual phantom, such as the HighResHead, when characterising a pCT system (chapter 6).

4.7 Discussion and conclusions

A high-resolution digital head phantom was created by converting a 0.18 mm pixel-size CT study of a detailed anthropomorphic phantom into a noiseless DICOM image set with 8 tissue equivalent materials and air. Eight high resolution CT scans were combined and treated with a segmentation process creating a noise-free digital phantom.

A second version of the `HighResHead` phantom that was created with a prototypic base of skull tumour and surrounding OAR (Fig. 4.3c) has applications in treatment planning studies. As a recent application example (unpublished), this digital phantom version was imported into the research version of RayStation (RaySearch Laboratories, Stockholm, Sweden) and used for treatment planning studies. The dose delivered to the tumour and surrounding OAR by a very high energy electron scanning pencil beam (VHEE) plan was calculated with a Monte Carlo simulation assuming treatment delivery with a scanning electron pencil beam (Fig. 4.4).

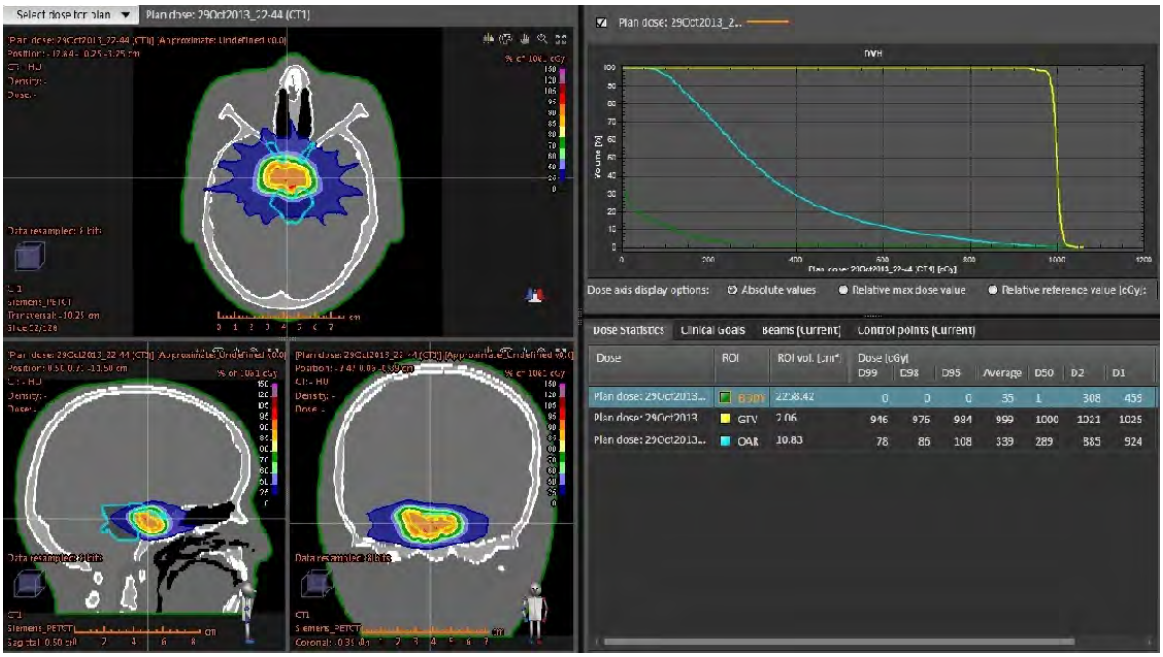

Figure 4.4: Digital head phantom implemented in RayStation for dosimetric evaluation of a VHEE plan.

This example proves the versatility and usefulness of the `HighResHead`. Other material assignments, such human standard tissues or additional tumour studies can be easily created. Since the `HighResHead` provides the ground truth of a real-world physical phantom, it can be used to verify the results of Monte Carlo simulations with experimental measurements. In chapter 5, the implementation of the `HighResHead` in a Geant4 simulation modelling the pCT system (described in chapter 3) is accurately presented and the `ConvHead` was used as the term of comparison in the analysis.

The `HighResHead` has also applications in planning range verification and experiments with proton CT or other CT modalities. It can be used to simulate new treatment modalities in treatment planning studies as demonstrated in this work.

Chapter 5

Development of a Software Platform for the Phase II pCT Scanner Prototype

Software Platform for Simulation of a Prototype Proton CT Scanner **by Giacometti V. et al.** The work presented in this chapter and in chapter 6 was submitted for publication and accepted as an original paper in 2016 in Medical Physics.

5.1 Introduction

Monte Carlo (MC) simulations are a useful tool to study the performance of detectors in many applications including in medical physics[92]. In proton imaging, this tool not only allows to understand and optimize the performance of individual detectors in a pCT imaging system, but it also gives the opportunity for studying the capabilities of pCT and developing and testing new reconstruction algorithms with realistic pCT data for investigators that do not have this technology.

A software platform of the pCT system described in chapter 3 consisting of modules for (1) Geant4 simulation, (2) WEPL calibration, (3) WEPL conversion, and (4) image reconstruction was developed, as schematically shown in Fig. 5.1. The Geant4 simulation

module produces realistic pCT output data using the prototype pCT scanner under study and the clinical or experimental proton beam line where the pCT scanner is installed. The WEPL calibration module simulates data with a calibration phantom and establishes a one-to-one relationship between the response of the multistage scintillator detector and the traversed thickness of the calibration phantom material of accurately known RSP. The output of the calibration module is used by the WEPL conversion module to process the residual proton energy from the multistage scintillator when scanning an object in the simulation. The tracked coordinates and WEPL values of protons are then processed by the image reconstruction module that implements the reconstruction software developed by the pCT collaboration[93] and produces reconstructed RSP images of the object.

This chapter provides a detailed description of the pCT software platform and its validation with respect to experimental results obtained on the experimental beam line of the LLUMC proton synchrotron. Its performance was also benchmarked against theoretical predictions. Specifically, the modules for (1) Geant4 simulation, (2) WEPL calibration, (3) WEPL conversion are described in this chapter while the image reconstruction module (4) will be discussed separately in chapter 6

The pCT software platform will provide a useful scientific and practical tool for further development of pCT technology and image reconstruction algorithms to the medical physics and applied mathematics community, and will allow testing of its characteristics and usefulness in proton treatment planning and image guidance.

5.2 The Geant4 pCT simulation

The pCT software platform, simulating the prototype CT scanner described above, was implemented in Geant4 version 10.1. Fig. 5.2 shows the schematic geometry of the prototype pCT scanner as simulated in Geant4[5,92,94]. The research proton beam line of the medical proton synchrotron at LLUMC[12] was modelled in the simulation.

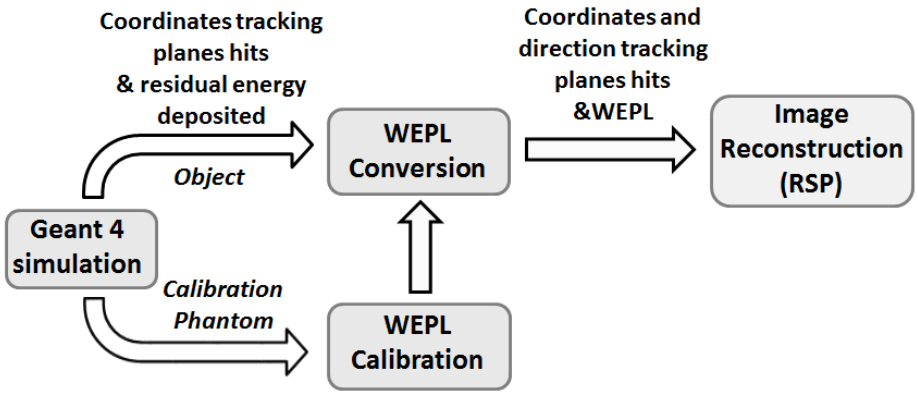

Figure 5.1: Schematic representation of the modular pCT software platform (for details see the introduction section 5.1).

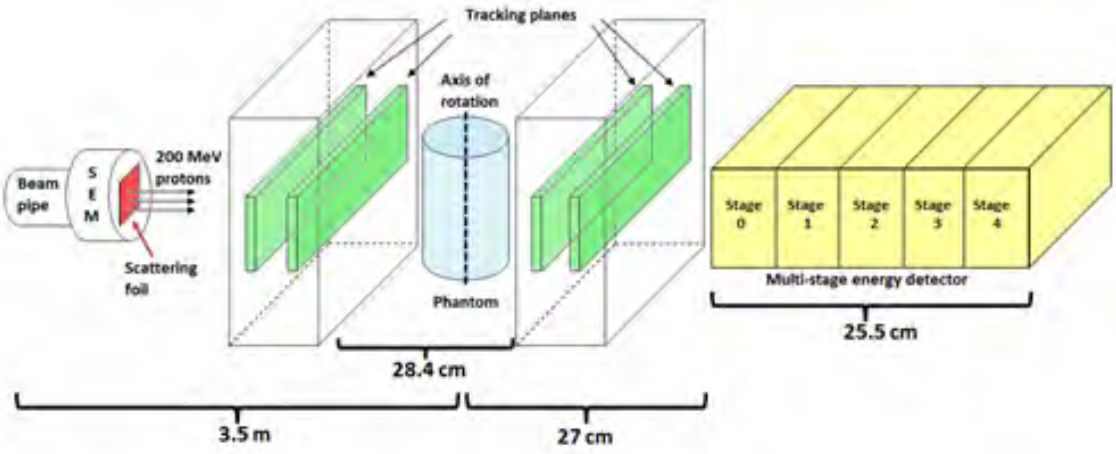

Figure 5.2: Schematic representation of the Geant4 model of the prototype pCT scanner.

The initial 200 MeV proton pencil beam was modelled assuming a Gaussian energy spread with a sigma of 5 keV[95]. The pencil beam was modelled with 0.2 cm diameter and without angular divergence inside a vacuum enclosed in a stainless steel pipe of 5 cm length, inner diameter of 3.52 cm, and wall thickness of 2.9 mm. After passing through five 12.7 $\mu\mathrm{m}$ thick aluminium foils, representing the secondary-electron emission monitor (SEM) integrated detectors in the distal end of the vacuum pipe, the proton beam exits through a 25 $\mu\mathrm{m}$ thick titanium foil. As in the real setup, a lead foil of 1.9 mm thickness was placed immediately after the SEM exit window to create a proton cone beam of approximately 16 cm full width at half maximum (FWHM) at the entrance of the front tracker. All these specifics represent exactly the experimental beam line of the LLUMC proton synchrotron a part from the length of the pipe that is shortened in the simulation. The length of the simulated pipe was chosen according to the position of the SEM in the real setup.

The SSD strips were modeled as sensitive silicon volumes of identical size and spacing, as in the real detector. Simulated strips were grouped according to chip, SSD, and FPGA number used by the DAQ system.

The beam profile at the entrance of the front tracking plane is shown in Fig. 5.3.a. The lead foil scattered the beam thus creating a cone of approximately 16 cm of FWHM. Fig. 5.3.b and fig. 5.3.c show the beam profile projected along the horizontal direction and vertical direction, respectively, fitted with a Gaussian curve.

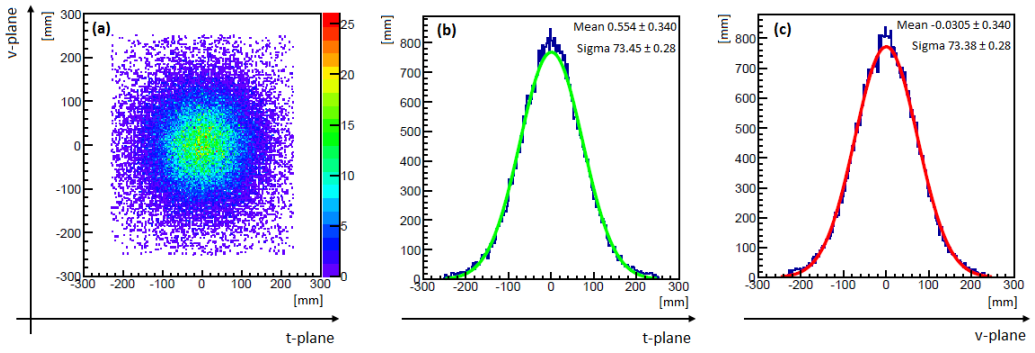

Figure 5.3: Proton beam profile of the simulated beam line at the upstream tracking plane (a), projected along the vertical plane (b) and horizontal plane (c), superposed with a Gaussian fit.

The scanned objects are placed at the scanner isocenter between the trackers. In the simulations presented in this work, the objects were rotated around a vertical rotation axis passing through isocenter in discrete steps of 4 degrees. However, a continuous rotation can be simulated as well. Protons traversing the scanned object typically stop in the multi-stage detector located 27 cm downstream from isocenter and behind the rear tracker (Fig. 5.2). The multi-stage detector has been implemented in detail in terms of geometry and materials, but the light collection process is not simulated and the energy deposited by the protons is directly retrieved in MeV.

Fig. 5.4 shows the position of the Brag peak in the multi-stage detector when no phantom is scanned. Most of the protons stop in the last stage of the multi-stage detector since they did not lose energy traversing any object.

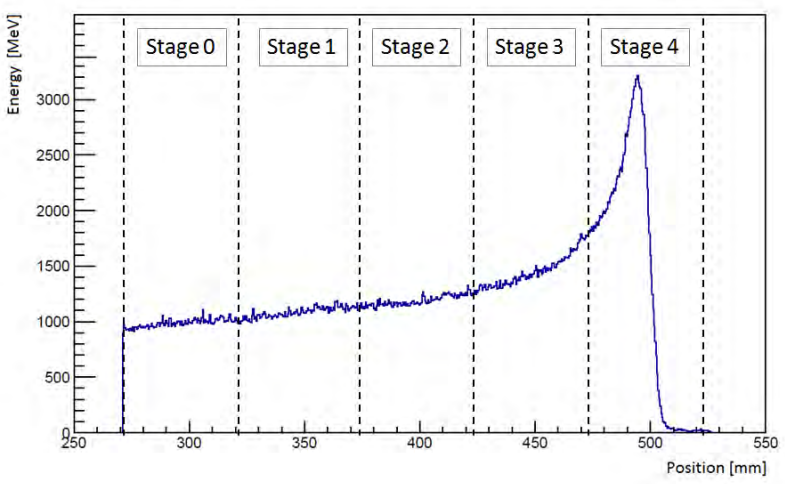

Figure 5.4: Energy deposited in the multi-stage energy detector in function of the position. The Bragg peak is located in stage 4 of the energy detector when no phantom is scanned.

When running a simulation in Geant4, it is necessary to specify a Physics List class which defines particles, physics processes and secondary particles production thresholds. Depending on particles, energies and targets simulated, different physics models can be included in the simulation. Geant4 provides some pre-packaged Physics Lists that can be used by users (e.g. hadronic Physics List, electromagnetic Physics List, etc.).

The Livermore EM Physics List[96] was selected to model electromagnetic interactions.

The threshold of production of secondary particles (cuts) was optimized to speed up the simulation without compromising the accuracy of its results. The secondary particles unable to travel at least the range cut distance chosen, were not produced. The Geant4 region class described in[97] was used with the following cuts in different geometrical components: 10 μm in the SEM, 5 μm in the energy detector, and 1 cm everywhere else. Low and high energy cut thresholds were 250 eV and 100 GeV, respectively. The range cut distances were chosen to optimise the speed of the simulation without losing important information about the proton energy deposition.

The G4HadronPhysicsQGSPBICHP and the G4HadronElasticPhysicsHP Physics Lists were chosen to describe inelastic and elastic scattering of hadrons, respectively. The neutron High Precision (HP) Model was selected to describe neutron interactions up to 20 MeV. Ion hadronic interactions were described by means of the G4IonBinaryCascadePhysics Physics List.

The output of the simulation consists of (1) the position of the proton intersection with the tracking planes and (2) the energy deposited by each proton in every stage of the multi-stage detector. The user can select from two output formats of the hit positions:

- hit coordinates (in mm) with respect to the origin of the isocenter of the pCT scanner coordinate system;
- strip, chip, SSD, and FPGA numbers of the strips hit by the protons in each tracking plane; this option serves to simulate the prototype pCT data bit stream for testing purposes.

The user can choose the number of projections or simulate a continuous scan. In the work presented here, all simulated pCT scans were obtained with 90 projections (4-degree intervals). The total number of proton histories generated for each projection was 6×10^6, which corresponds to a central proton fluence of approximately 100 protons/$\mathrm{mm}^2$and is

approximately the same as the fluence used in the real pCT scan with the current prototype scanner.

5.3 Scanner calibration

A detailed description of the calibration procedure of the multistage scintillator detector can be found in[45]. This procedure was also simulated in the pCT software platform in order to realistically reproduce the performance of the pCT prototype system.

For a single proton, its WEPL is defined as the integral of the object RSP along the total path length l of the proton through the object, where the RSP is defined as the ratio of the stopping power (SP) of a material and the SP of water.

$$WEPL = \int_l RPS(E)dl = \int_l \frac{SP(E)_{\text{material}}}{SP(E)_{\text{water}}}dl \tag{5.1}$$

In principle, knowing the residual energy of protons, the WEPL can be calculated by numerically solving the integral on the right side of equation 5.1 using Bethe-Bloch theory, which is accurate above 10 MeV[98]. Rather than Bethe Bloch theory, which requires an assumption about the mean excitation potential I, a practical approach consists of calibrating the energy detector response against known water-equivalent thickness using a calibration phantom with accurately known RSP[45,99]. Here, the calibration was determined by correlating the signal generated by protons stopping in the multi-stage detector to the known thickness traversed in the simulated calibration phantom, accurately described in section 3.6.3 (Fig. 3.7).

Specifically, equation 5.1 then becomes:

$$WEPL = RSP_{\text{polystirene}} \cdot x \tag{5.2}$$

where x is the physical thickness traversed in the calibration phantom and $RSP_{\text{polystirene}}$

is known to be 1.038 for the calibration phantom used in this work. This calibration procedure establishes a one-to-one relationship between energy detector response and WEPL that allows measuring the WEPL of protons traversing any object, knowing the energy response in the scintillator stage where they stopped.

The calibration procedure was simulated with Geant4; to reproduce the experimental scanning procedure, five calibration simulations with 10^6 histories each were executed, one with the stairs alone, and four with the 1, 2, 3, or 4 degraders placed after the stairs, respectively. The polystyrene thickness traversed by the protons and the energy deposited in each stage of the multi-stage detector were recorded for each incident proton. To avoid ambiguities, protons entering a step of the stairs within 0.35 mm from its edge were excluded. Also, protons that were recorded to have entered more than one step were excluded. Fig. 5.5 shows the simulated geometrical set up for the calibration with the stairs and 4 polystyrene degraders.

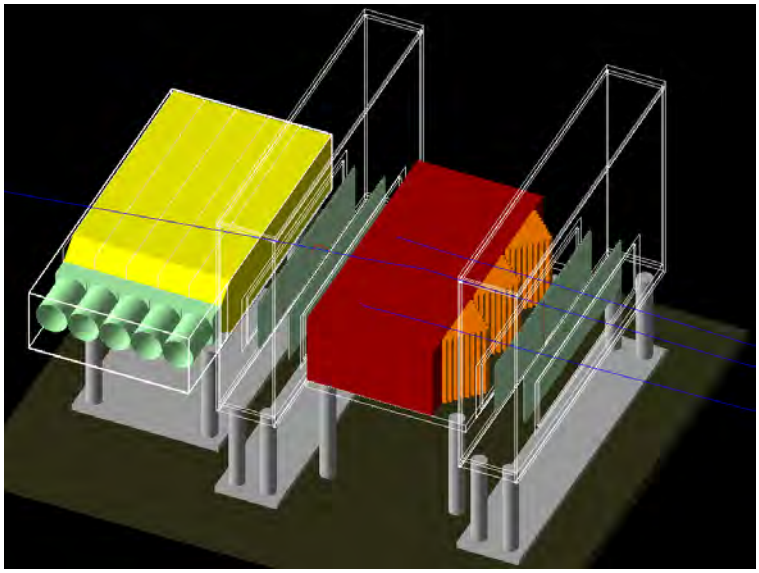

Figure 5.5: The Geant4 simulated calibration setup. The green panels represent the silicon detectors; the yellow parallelepipeds with truncated corners at PMT ends represent the 5 stages of the multistage scintillator. The calibration phantom comprised of the stepped pyramids in orange and up to 4 polystyrene degraders (parallelepiped in red) are located between the two front and rear tracker. Protons enter the scanner from the right.

For each polystyrene step thickness, the mean energy deposited in every stage was eval-

uated with a Gaussian fit centred approximately in correspondence of the peak of the histograms of the scintillator responses. Polynomial curves of energy vs polystyrene step thickness were fit to those mean energy values. One should note that with the exception of the most distal stage, every stage had two types of response: a response from protons traversing the stage and a response from protons stopping in the stage. Fig. 5.6 shows simulated scatter plots superimposed with polynomial fitsv, in every stage. The plots show polystyrene step thickness vs. energy deposited. The distinction between stopping (upper segments) and traversing (lower segments) responses are clearly seen. From the calibration curves of stopping protons, the proton WEPL corresponding to the response recorded by the stage where the proton stopped was derived using equation 5.2. Only for protons that apparently stopped within 2 mm from an interface between two stages, ambiguities were resolved by taking into account the response of the upstream stages for traversing protons, statistically weighting the stopping and traversing contributions.

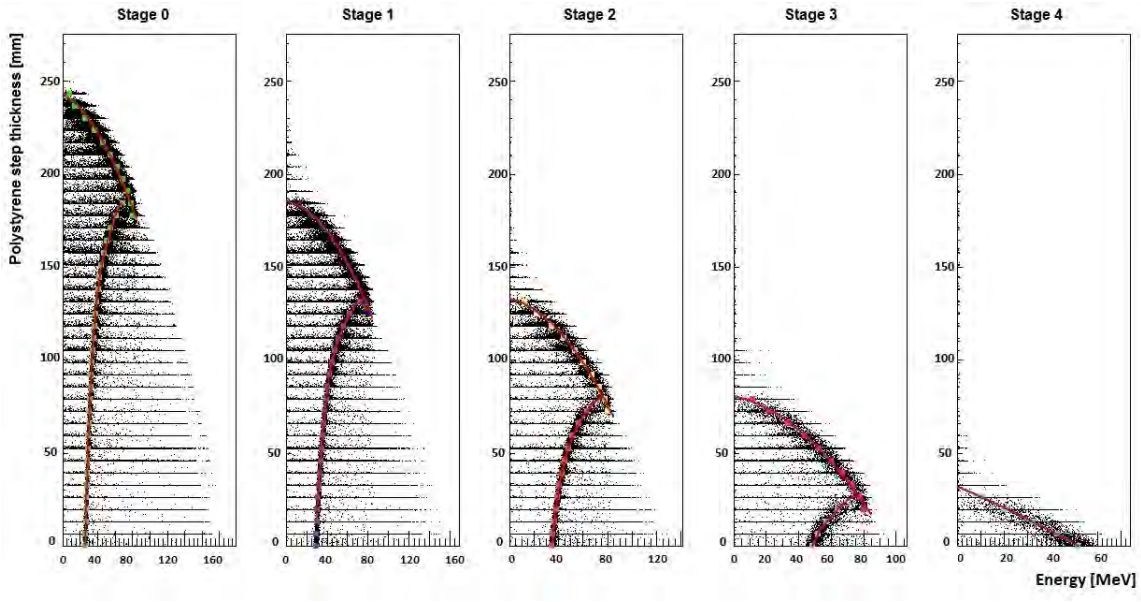

Figure 5.6: Scatter plots and calibration curves (red lines) of polystyrene step thickness vs. detector response derived from fitting energy response distributions to the simulated calibration data. The plots show the polynomial calibration curve segments corresponding to stopping protons (upper segment) and to traversing protons (lower segment) in each stage, except for stage 4, which only recorded stopping protons.

A standard error propagation procedure was used to calculate the WEPL uncertainty

$\Delta(\text{WEPL})$ associated to the calibration curve chosen[100]:

$$\Delta\text{WEPL} = \sigma_E(x)\frac{df(x)}{dx} \tag{5.3}$$

where x is the thickness traversed by the protons, and $f(x)$ is the generic polynomial fitting the collected data; $\sigma_E(x)$ is the standard deviation of the Gaussian curve fitting the energy response $E(x)$ of each energy detector stage at x. Several polynomial fitting curves $f_S(x)$ and $f_T(x)$ were tested and $\Delta(\text{WEPL})$ were compared.

5.4 pCT software platform validation

The single modules forming the pCT software platform were validated separately.

The Geant4 simulation module was validated by comparing the tracker detector responses with experimental measurements. In particular, the horizontal and vertical proton beam profiles reconstructed from the proton hit frequencies in all tracking planes were compared. To validate WEPL calibration and conversion modules, the simulated WEPL distributions of protons passing through polystyrene degraders of three different thicknesses of 50.8 mm, 101.6 mm, and 203.2 mm, respectively, were compared with the experimental WEPL distributions. In addition, both experimental and simulated mean WEPL values, obtained from a Gaussian fit to the central part of the distributions, were compared with the expected value of RSP = 1.038 times the physical thickness of the degraders.

The image reconstruction module of the pCT platform was validated by comparing reconstructed RSP values with experimental results for a variety of phantoms as described in chapter 6.

5.5 Results

5.5.1 Tracker response

For validating the simulated tracker responses, simulated and experimental horizontal and vertical beam profiles in the front and rear tracking planes were compared for a run without any phantoms in the beam path. Fig. 5.7 shows a comparison between the simulated and experimental tracker responses to a broad Gaussian-shaped proton beam generated by the 1.9 mm lead foil, normalized with respect to the total number of histories traversing each tracking plane. Since the t-planes are four time longer than the v-planes, their responses show a typical Gaussian shape, whereas the responses of the v-planes only show the central part of the Gaussian profile.

The shapes of the profiles in the respective planes with horizontal strips (v-planes) and vertical strips (t-planes) was generally very similar, validating the correctness of the beam line simulation. During the experiment, the system was carefully aligned to the room beam line laser, avoiding shift and tilt errors relative to the vertical axis. However, the cone beam axis was slightly tilted relative to the vertical scanner axis in the experiment causing asymmetry of the beam profile in the v-planes. The peak of counts at +40 mm in the first rear v-planes is caused by noisy strips. The Geant4 simulation correctly reproduced the drop in tracking efficiencies due to the vertical gaps in sensitivity between individual SSDs also seen in the experimental profiles. One should note that the missing coordinates due to the gaps were reconstructed based on the information from the other tracking planes and knowledge of the gap coordinates[82].

5.5.2 Multi-stage scintillator response and scanner calibration

Table 5.1 shows the WEPL uncertainty $\Delta(\mathrm{WEPL})$, calculated using eq. 5.3, and associated to the polynomial fit $f_S(x)$ and $f_T(x)$ chosen for responses to stopping and traversing

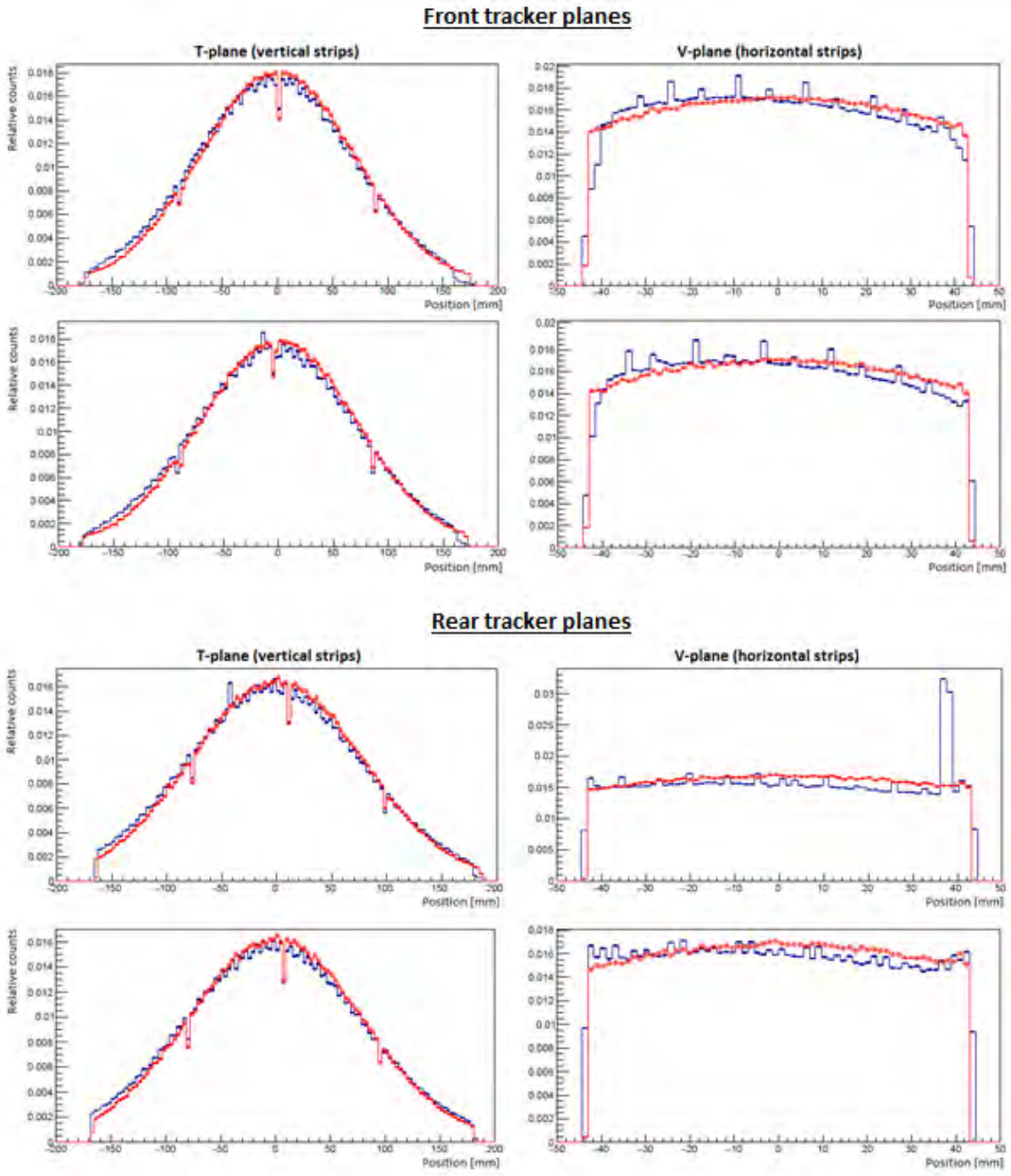

Figure 5.7: Simulated (red) vs experimental (blue) responses of each tracker plane to a broad Gaussian-shaped proton beam. The two left panels show the t-plane responses with drops in counts in the graph corresponding to the gaps between SSDs. The right two panels show the v-plane responses, in this cases the protons are registered without any dead zones. Note that the horizontal scales in the graphs on the left and on the right are different.

protons, respectively.

The smallest Δ(WEPL) was achieved using a 4^{th} grade polynomial curve for $f_T(x)$ and a 2^{nd} grade polynomial curve for $f_S(x)$.

Table 5.1: WEPL uncertainty associated to different polynomial fitting curves.

	Δ(WEPL) for $f_T(x)$				Δ(WEPL) for $f_S(x)$				
	Stage 0	*Stage 1*	*Stage 2*	*Stage 3*	*Stage 0*	*Stage 1*	*Stage 2*	*Stage 3*	*Stage 4*
2^{nd} grade polynomial	9.391	6.177	5.317	3.482	3.516	3.477	3.496	3.499	4.156
3^{rd} grade polynomial	9.135	6.775	5.321	3.300	4.199	3.954	3.960	3.948	4.463
4^{th} grade polynomial	9.129	6.492	5.036	3.463	4.135	3.835	3.860	3.864	4.642
5^{th} grade polynomial	9.430	6.924	4.779	9.639	4.687	4.317	4.298	4.259	4.638

For validating the simulated multi-stage scintillator detector, the simulated WEPL distribution of protons passing through polystyrene degraders of 50.8 mm, 101.6 mm, and 203.2 mm thickness, respectively, were compared with the experimental WEPL distributions (Fig. 5.8). In Table 5.2, the mean WEPL values calculated for experimental and simulated data are compared with the theoretical values calculated using equation 5.2, where x is the physical thickness of the degraders. The agreement between measured and theoretical WEPL was within 0.7% both for experimental and simulated data. The difference between experimental and simulated WEPL was below 1%.

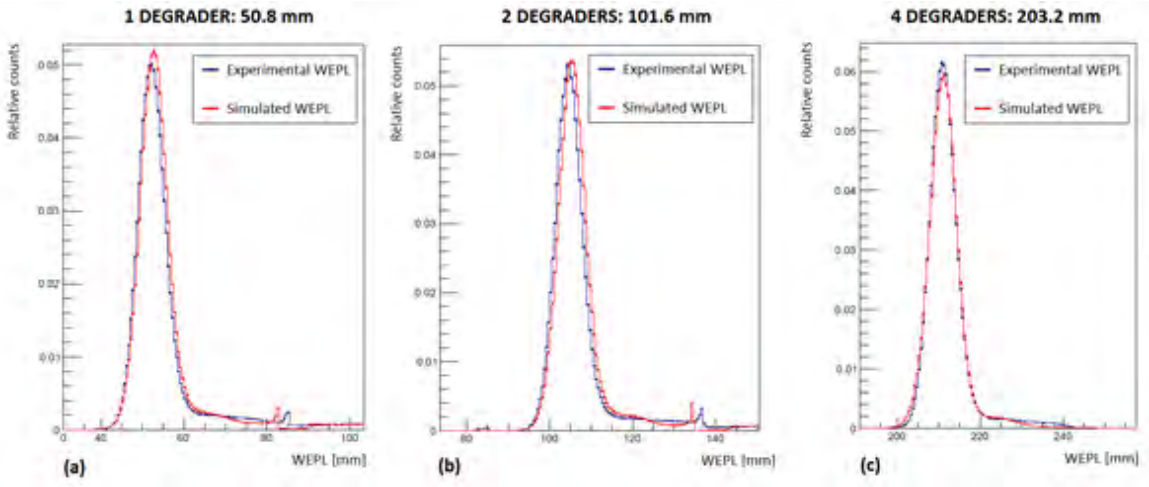

Figure 5.8: WEPL distribution of 1 slab (a), 2 slabs (b) and 4 slabs (c) of polystyrene using experimental data (in blue) and simulated data (in red).

Table 5.2: Comparison of experimental, simulated and theoretical WEPL (eq. 5.2) from the scan of 1, 2 and 4 polystyrene bricks.

			Experimental WEPL		*Simulated WEPL*		
Number of polystyrene degraders	Thickness [mm]	Theoretical WEPL [mm]	Mean ± SD [mm]	Difference[1] [%]	Mean ± SD [mm]	Difference[2] [%]	WEPL Difference[3] [%]
1	50.8	52.73	52.36 ± 3.38	-0.70	52.80 ± 3.48	0.13	0.84
2	101.6	105.46	104.80 ± 3.31	-0.62	105.50 ± 3.42	0.03	0.66
3	203.2	210.92	211.17 ± 3.17	0.08	211.10 ± 3.39	0.08	-0.009

[1] (experimental - theoretical)/theoretical
[2] (simulated - theoretical)/theoretical
[3] (simulated - experimental)/experimental

5.6 Discussion and Conclusions

In this chapter, the validation of the modules for (1) Geant4 simulation, (2) WEPL calibration, (3) WEPL conversion of a pCT software platform modelling a prototype pCT scanner was performed. The comparison of the responses of the tracking detectors to the scattered proton cone beam and the response of the 5-stage scintillator detectors used to calculate the WEPL of individual protons were performed. The validation of the image reconstruction module (4) will be discussed separately in chapter 6.

The simulation software has built-in flexibility in terms of geometry of the scanner and scanned objects, including the calibration object, allowing different calibration procedures to be tested and compared. The reconstruction procedure is straightforward once the output files are produced using Geant4 but the reconstruction module can also be changed by the user allowing different reconstruction algorithms to be used and added. The work conducted by Dr. Tai Dou at UCLA shown in in Fig. 5.9 proved the versatility and flexibility of the simulation software.

The pCT software platform can be used as a versatile tool for studying and improving the performance of clinical pCT without having access to an experimental pCT scanner. In the present work we implemented the experimental proton beam line at LLUMC. Other beam line models can be implemented as well, e.g. the NMCPC beam line. Note that the possibility of implementing patient anatomy in the form of DICOM studies within the

Geant4 simulation makes it possible to study the feasibility of pCT in treatment planning and pretreatment plan verification based on real patients in a virtual fashion. For example, the developed pCT software platform was recently used to simulate and reconstruct a pCT scan using an imported CT DICOM image of a lung cancer patient[101]. Since the existing scanner is only suitable for head scans, the geometry of the simulation and the proton energy were changed to accommodate the chest scan. The space between the two tracking modules was enlarged, and the active area of the SSDs was increased. In order to provide sufficient residual energy for all the projection angles, the proton energy was also increased to 230 MeV. An additional scintillating stage was added to the multi-stage detector to cover the total proton range, and new calibration curves were defined to convert the energy response into WEPL. The reconstructed chest image is shown in Fig. 5.9 and demonstrates the usefulness of the pCT software platform to study pCT in new applications and different anatomical regions.

Figure 5.9: proton CT reconstruction of a realistic human chest performed using simulated data. The sticks artefacts can be eliminated increasing the statistics of the simulation.

In addition, the pCT software platform will allow the development and test of new reconstruction algorithms, for example, for reconstructing 4D pCT image sets from breathing

patients. Target motion can cause severe geometrical distortion during a scan such as the displacement of the centre of the image or the lengthening/shortening of the target in the final image[69,102]. Therefore, using the pCT software platform it would be possible to simulate both the scan and the image reconstruction of a moving object in order to investigate and finally reduce (and possibly eliminate) the image artifacts caused by the motion.

Chapter 6

Evaluation of the Image Quality Achieved with the Phase II pCT Scanner Prototype

6.1 Introduction

The image reconstruction of pCT aims at calculating a 3D RSP map of the scanned object from the tracking and WEPL data for each single proton recorded. The reconstructed 3D RSP map consists of a sequence of images (pCT slices) in which each pixel corresponds to one RSP value.

Several reconstruction algorithms, specifically designed for pCT reconstruction, have been developed and published in recent years[103,104] . These algorithms use individual proton histories and calculate their estimated path through the object either based on the MLP[6] or cubic spline[105,106] formalisms. A review of iterative pCT image reconstruction techniques based on projections onto convex sets and MLP formalism is presented in[107].

FBP was one of the first image reconstruction techniques used in pCT[37] because of its common use in xCT. It consists of integrating all possible rays that pass through the same

point, i.e. "*backprojecting*" them and then *filtering* the image produced. In xCT individual projections are rendered in terms of x-ray attenuation coefficient while in pCT in terms of WEPL[10]. Iterative reconstruction techniques are a valid alternative to FBP, nowadays the preferred reconstruction methods used in pCT. They lead to a better image resolution and curved proton path can be incorporated in the reconstruction algorithm but they are computationally more intensive.

In this chapter, the image reconstruction module of the pCT platform was validated by comparing reconstructed RSP values with experimental results for a variety of phantoms. Specifically, the sensitometry module of the Catphan® 600 series was used to compare both reconstructed experimental and simulated RSP with the RSP values measured with the PeakFinder (PTW, Freiburg, Germany) at the Heidelberg Ion-Beam Therapy (HIT) Centre. The comparison of simulated and reconstructed modulation transfer function (MTF) was realized using the pCT reconstructed images of the linepair module of the Catphan® 600 series. The HN715 pediatric head phantom was used to compare both reconstructed experimental and simulated RSP. Operationally it was not possible to use the PeakFinder to measure the RSP of the different tissues in the phantom because the phantom cannot be opened in order to extract different materials. Therefore, it was calculated analytically, and a specific Geant4 simulation was built to collect the data required in the analytical formula.

Images reconstructed performing stardard pCT and cone beam CT (CBCT) scans of the sensitometry module were also compared. In addition, the dose delivered during a pCT and a CBCT scan were compared using the CTP554 dose phantom of the Catphan® 600 series. This preliminary dosimetric evaluation of the phase II pCT scanner prototype was entirely performed using the pCT software platform described in chapter 5.

6.2 Image reconstruction

In the current version of the pCT software platform, the block-iterative diagonally relaxed orthogonal projections (DROP) algorithm has been implemented for image reconstruction of experimental and simulated phantom pCT data. This image reconstruction algorithm performs feasibility seeking steps integrated with a total variation superiorization (TVS) scheme[103] and only considers protons entering into and exiting from the cylindrical reconstruction volume that enclosed the phantom object. Three-sigma cuts on WEPL, angle and vertical and horizontal deviation were implemented to remove protons that underwent large-angle scattering and/or large energy losses due to inelastic nuclear interactions. The accepted proton histories were binned into equal intervals of beam projection angles, lateral coordinates and vertical coordinates. The binned data were used as input to the Feldkamp-Davis-Kress (FDK) algorithm, the cone beam version of the FBP algorithm. The resulting FBP image was used to define the object boundary and as the starting point of the iterative reconstruction algorithm.

In brief, WEPL and position and direction of individual protons traversing the silicon detectors generate a linear system of equations of the form $Ax = b$ which is then solved iteratively with the DROP-TVS algorithm. The elements a_{ij} of the matrix A correspond to the intersection length of the i^{th} proton with the j^{th} voxel, x is the unknown RSP vector, and b is the vector of WEPL measurements. The algorithm partitioned the proton histories into 40 blocks and, and 8 cycles of iterating through all histories are completed. The relaxation parameter of the DROP algorithm was set to 0.1[10].

The DROP-TVS algorithm was executed on a single graphical processing unit (GPU) workstation, which is part of a computer cluster at the California State University San Bernardino. The cluster is composed of 8 nodes connected with 20 GB Infiniband and 1 GB Ethernet. Each node consists of a dual 6-core Xeon (48GB of RAM, 1 TB of Raid, 1.5 TB of data added storage). A GPU NVIDIA GTX-780 was used for the image reconstruc-

tion.

In this work, all simulated and experimental pCT scans were obtained with 90 projections (4-degree intervals) and the total number of proton histories per projection was $\sim 8 \times 10^6$. For comparative analysis, the RSPs of the different materials were determined using ImageJ.

6.3 Catphan Modules

6.3.1 Catphan Modules - Image Reconstruction

The validation of the performance of the simulated pCT scanner was performed with the sensitometry and line pair modules of the Catphan ® 600 series (The Phantom Laboratory, Salem, New York, USA) and a pediatric anthropomorphic head phantom (model HN715, CIRS, Norfolk, Virginia, USA), as described below.

The CTP 404 sensitometry module (diameter 15 cm) contains eight cylindrical cavities of 1.22 cm diameter, six of which are filled with different materials, and two that are filled with air (Fig. 6.1a). The RSP evaluation of the reconstructed images was conducted with ImageJ version 1.46r, a Java-based open source image-analysis software package that was downloaded from the US National Institute of Health website (http://imagej.nih.gov/ij). A circular area of approximately 1 cm diameter was selected within the boundaries of each insert and the mean RSP and standard deviation were calculated using standard ImageJ functions.

In addition, direct RSP measurements of the six CTP404 inserts were performed at the Heidelberg Ion-Beam Therapy Center (HIT) with the PeakFinder (PTW, Freiburg, Germany), a variable water column equipped with two plane-parallel ionization chambers, each of 4.08 cm radius[108]. The water equivalent thickness (WET) of each phantom insert and the phantom body were measured with a carbon beam of 310.82MeV/u (range 18.02 cm

in water) with 4.4 mm FWHM spot size at the isocenter. The measured RSP values were compared with the RSPs reconstructed from simulated and experimental pCT data using the iterative image reconstruction algorithm described in section 6.2. The use of carbon ions for measuring the RSP of materials for protons was validated with a separate measurement comparing data obtained with protons and carbon ions for different tissue equivalent materials using the same experimental setup. The RSP values obtained for carbon ions and protons were the same within the accuracy of the measurements, confirming that carbon ions can be used to measure the RSP of tissue-equivalent materials for protons. The advantage of utilizing carbon beams for the RSP measurements was the smaller spot size and the reduced multiple Coulomb scattering of the heavier ions compared to protons, making the measurement more suitable for the small inserts (12 mm diameter) of the CTP404 module. The sharper Bragg peak also allows easier WET interpretation from the measured Bragg curves.

The CTP528 line pair module (diameter 15 cm) provides 21 groups of high-contrast aluminum bars ranging from 1 to 21 line pairs per cm arranged such that all patterns share the same distance from the center of the phantom (Fig. 6.1b). This was used to compare the spatial resolution measured in images of the phantom reconstructed from simulated data to those measured in images reconstructed from experimental pCT data. For quantitative comparison of the spatial resolution, the MTF was calculated for both cases using a custom-script written in the Python programming language[109]. For each of line-pair patterns with lp = 1-5 line pairs, the average reconstructed RSP of the aluminum peaks and the average RSP of the base material troughs were calculated. The MTF for each analyzed line pair group was then calculated as:

$$MTF(lp) = \frac{< RSP_{\text{peak}}(lp) > - < RSP_{\text{trough}}(lp) >}{< RSP_{\text{Al}} > - < RSP_{\text{base}} >} \tag{6.1}$$

where $< RSP_{\text{peak}}(lp) >$ and $< RSP_{\text{trough}}(lp) >$ are the average reconstructed RSP values

for the aluminum peaks and base material troughs for a given line-pair number, respectively, and $< RSP_{\text{Al}} >$ and $< RSP_{\text{base}} >$ are the energy-averaged RSP values for aluminum (2.11) and the base material (1.14), respectively, which were calculated as described for the head phantom materials in section 6.4.2.

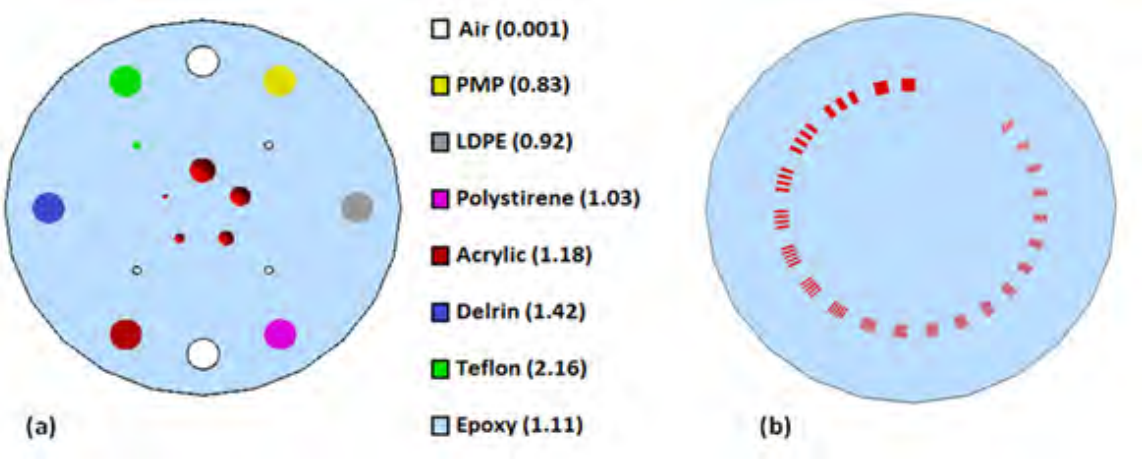

Figure 6.1: (a) Geant4 model of the CTP404 sensitometry module with color-coded materials as indicated. The density of each material, in parenthesis, is expressed in g/cm^3. (b) Geant4 model CTP528 line pair phantom with aluminium bars embedded in a polymer. Note that the base material of both phantoms is the same (epoxy).

6.3.2 Catphan Modules - Image Reconstruction Analysis

Fig. 6.2 shows the reconstructed images of the CTP404 sensitometry module using simulated and experimental data (slices thickness 2.5 mm, reconstructed field of view 18 cm, pixel size 0.7 mm). Table 2 shows the comparison between PeakFinder-measured and reconstructed RSP values (experimental and simulated) for the insertions in the sensitometry module. The difference between simulated and experimental RSP is below 1% for all the materials except PMP. The difference between simulated and experimental RSP for PMP is 1.6%: the simulated RSP is in full agreement with the expected value, but slightly lower than the experimental one. Fig. 6.3 shows the agreement between experimental/simulated RSP and PeakFinder-measured RSP. The coefficients of determination of 0.9999 for experimental data and 0.9998 for simulated data reflect the excellent predictability of directly measured

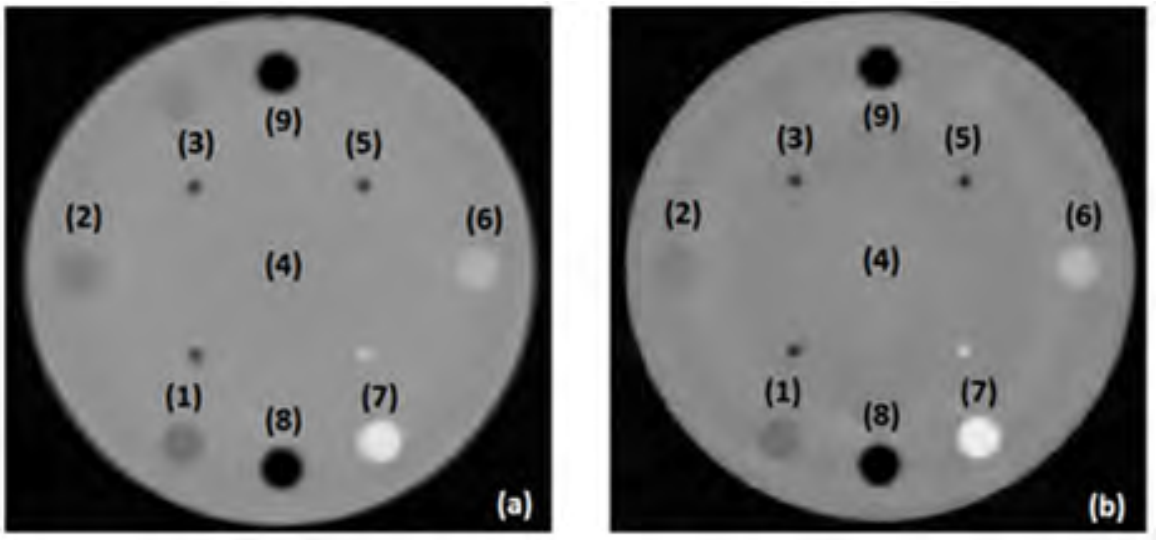

Figure 6.2: Catphan ® 600 sensitometry module pCT reconstruction using experimental (a) and simulated (b) data. The insertions are: PMP (1), LDPE (2), Polystyrene (3), Epoxy (4), PMMA (5), Delrin (6), Teflon (7), Air (8, 9).

RSP values with the reconstructed RSP values for both simulated and experimental pCT reconstructions. Finally, even if the difference between simulated and experimental RSP is below 1%, the protons stopping in the interfaces between the scintillators cause different outcomes in the final WEPL evaluation, as proven by the ring artefacts in the simulated reconstructed image.

Fig. 6.3 shows the reconstructed images of the line pair module using simulated and experimental data (slices thickness 2.5 mm, reconstructed field of view 18 cm, pixel size 0.7 mm). Fig. 6.5 shows simulated and experimental MTF calculated for the first five groups of line pairs, where the gaps between the beads are still slightly visible. Simulated results are slightly higher than experimental MTFs but the difference never exceeds 0.026 and is always within one standard deviation.

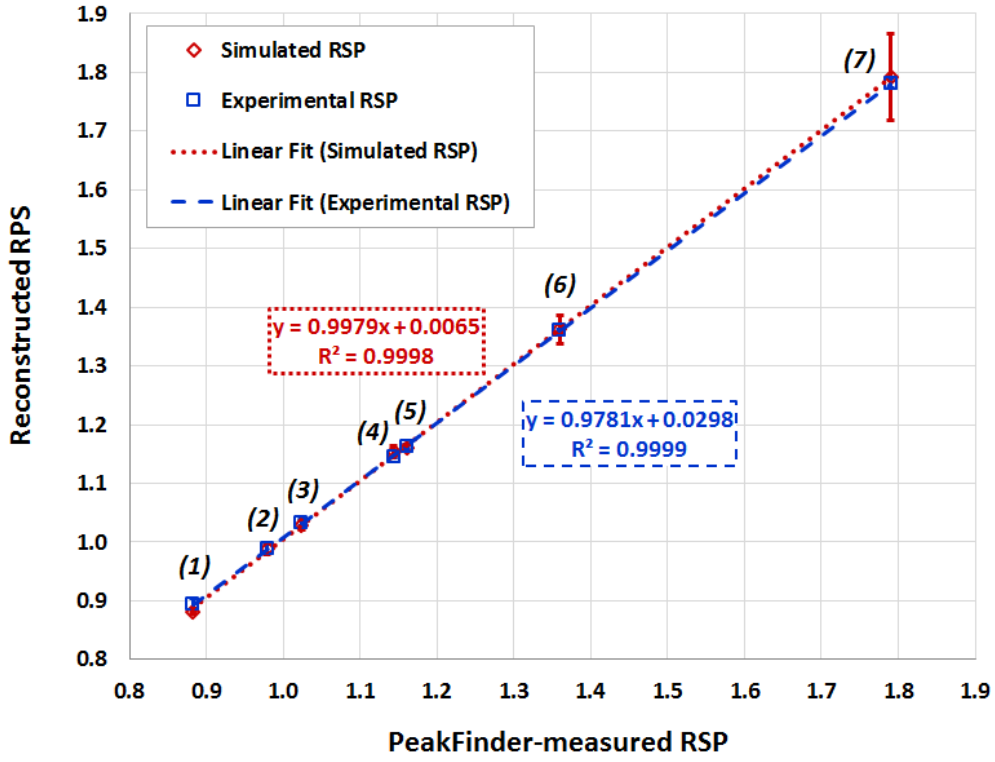

Figure 6.3: Catphan ® 600 sensitometry module reconstructed RSP from simulated data (in red) and experimental data (in blue). The dashed trend lines show the agreement between PeakFinder-measured and reconstructed RSPs. The number in brackets corresponds to the material labels listed in Tab. 6.1 and shown in Fig. 6.2. The coefficient of determination is 0.99 for both simulated and experimental data.

Table 6.1: Comparison between PeakFinder-measured and experimental and simulated reconstructed RSP values for the materials of the sensitometry module.

		Reconstructed RSP (experimental)		*Reconstructed RSP (simulated)*		
(Insert #) Material	PF-measured RSP	Mean ± SD	Difference [%][1]	Mean ± SD	Difference [%][2]	Difference [%][3]
(1) PMP	0.883±0.002	0.895±0.008	1.39	0.880±0.003	-0.30	-1.68
(2) LDPE	0.979±0.002	0.988±0.008	0.91	0.989±0.010	1.02	0.10
(3) Polystyrene	1.204±0.001	1.033±0.005	0.91	1.029±0.008	0.52	-0.39
(4) Epoxy	1.144±0.001	1.145±0.002	0.11	1.154±0.009	0.90	0.79
(5) PMMA	1.160±0.001	1.162±0.003	0.14	1.161±0.004	0.06	-0.09
(6) Delrin	1.359±0.003	1.360±0.002	0.04	1.362±0.024	0.19	0.15
(7) Teflon	1.790±0.002	1.782±0.008	-0.46	1.792±0.074	0.10	0.56

[1] (experimental - $PF_{measured}$)/$PF_{measured}$
[2] (simulated - $PF_{measured}$)/$PF_{measured}$
[3] (simulated - experimental)/experimental

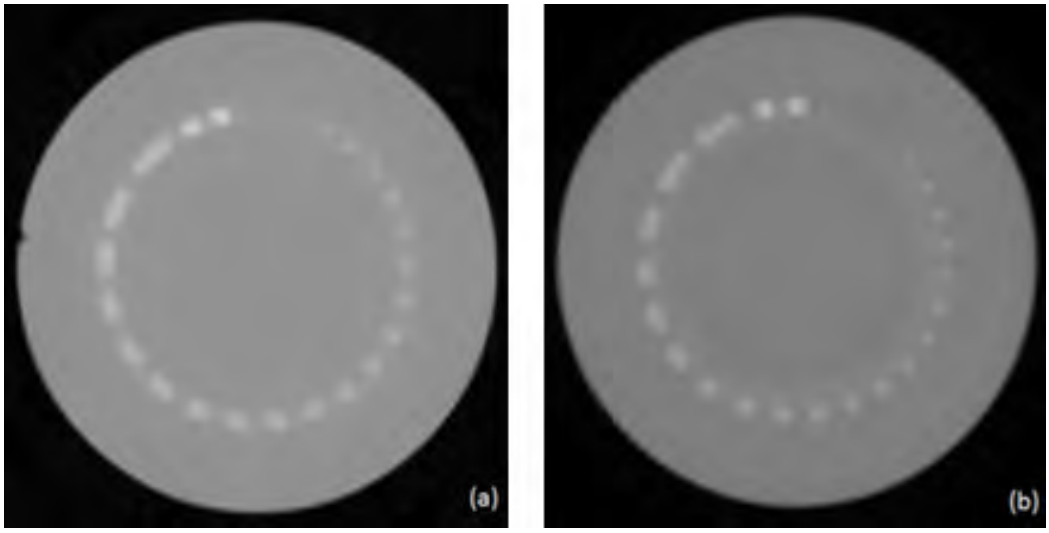

Figure 6.4: Catphan ® 600 Line pair module pCT reconstruction using experimental (a) and simulated (b) data.

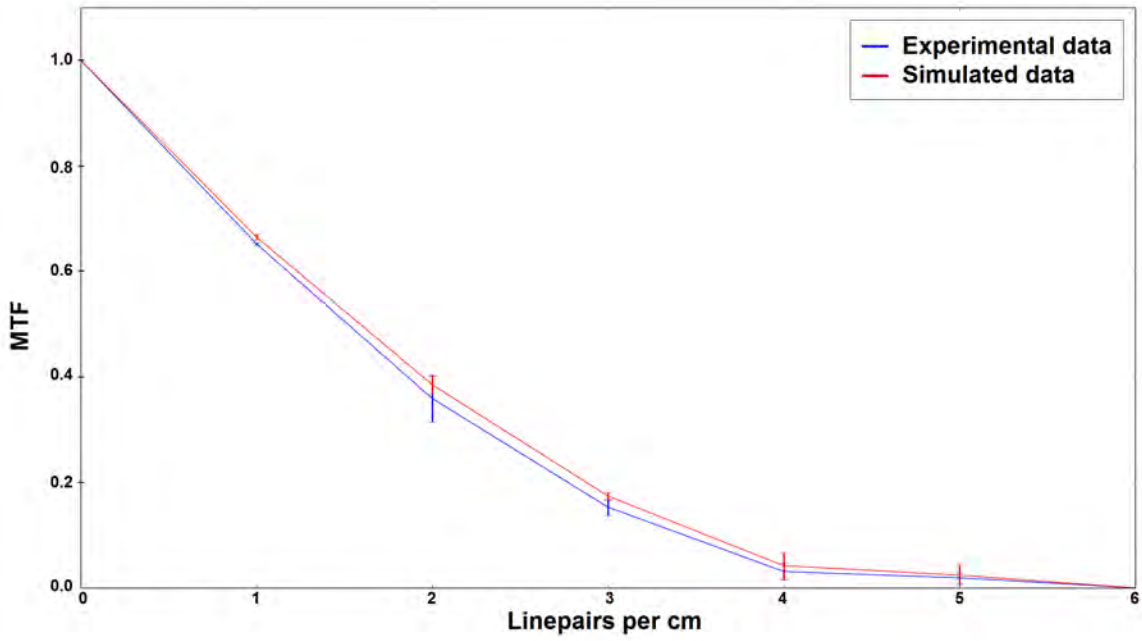

Figure 6.5: Catphan ® 600 Line pair MTF calculated for experimental data (in red) and simulated data (in blue).

6.4 Head Phantom

6.4.1 `HighResHead` vs `ConvHead`

The `HighResHead` was included in the pCT software platform (Fig. 6.6) described in chapter 5. In particular, it was implemented in the Geant4 DICOM extended example[110], which was then integrated in the Geant4 simulation module of the pCT software platform. The Geant4 DICOM extended example creates a Geant4 voxelised geometry based on the information of input DICOM files, using the Geant4 Parameterised Volumes geometry functionality (*G4VPVParameterisation*). By default, in the Geant4 example, the HU value of each voxel, information contained in the input DICOM study, is converted into the corresponding density based on the stoichiometric calibration method, described by Schneider et al.[21]. In addition, in the DICOM example, lower and upper bounds of density intervals must be defined by the user in order to assign corresponding tissue materials.

The uncertainties introduced by converting HU numbers into tissue materials using a calibration curve were investigated by Paganetti et al. for proton dose calculations and range verification studies[111–113]. It was shown that when the conversion is based on a proper stoichiometric calibration, the proton beam range uncertainty is about 0.2%. Therefore, the calibration curve based on the characteristic of the LLUMC CT scanner was used to model the `ConvHead` in the Geant4 DICOM application. Since the `HighResHead` contains only 8 HU values, resulting from the segmentation work described in Chapter 4, it was decided to assign each HU value directly to the corresponding material of the physical phantom, bypassing the stoichiometric calibration curve.

RSP values reconstructed from simulated pCT data obtained with the `HighResHead` and the `ConvHead` were compared with those derived from experimental pCT data of the underlying physical head phantom. For a better statistics, the total number of proton histories generated for each projection was 12×10^6.

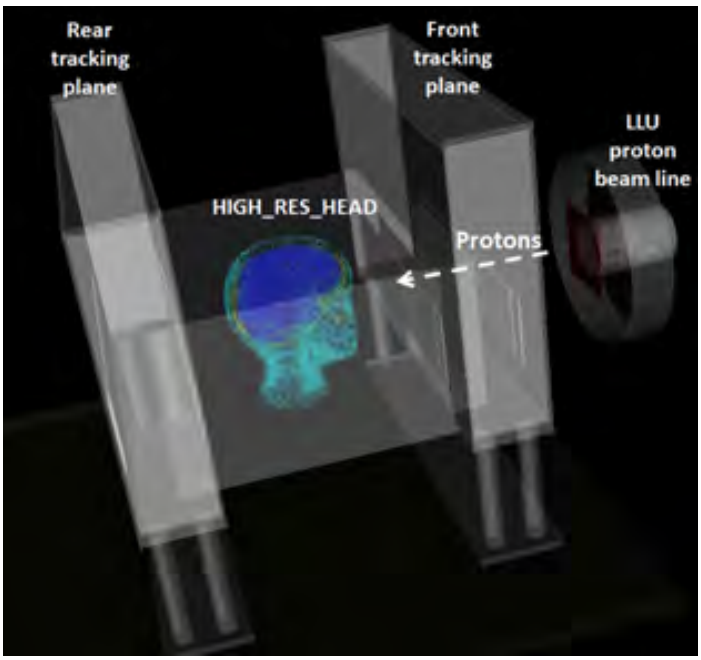

Figure 6.6: Visualisation of the Geant4 application set-up modelling the phase II pCT scanner prototype including the `HighResHead`.

6.4.1.1 `HighResHead` vs `ConvHead` - Image Reconstruction Analysis

Fig. 6.7 shows the visualisation of the `ConvHead` and `HighResHead` in Geant4. Fig. 6.8 shows the pCT images reconstructed from (a) simulated `ConvHead` data, (b) simulated `HighResHead` data, and (c) experimental data with the physical phantom. Approximately the same number of protons per projection were used for each image reconstruction. The mean and standard deviation (SD) of tissue RSP values in the three different images were calculated and are compared in Table 6.2.

It is obvious that the different tissues in the `ConvHead` (Fig. 6.7(a)) were not as well defined as in the `HighResHead` (Fig. 6.7(b)). For example, in `ConvHead`, many soft tissue voxels were incorrectly modelled as brain voxels. Also, in `ConvHead`, the extent of the cortical bone region was overestimated, and spinal disc voxels were found in regions close to cortical bone where they are not present anatomically. The noiseless digital phantom `HighResHead`, on the other hand, not only has a higher spatial resolution but also provides a more accurate representation of the physical head phantom. This lead to a more

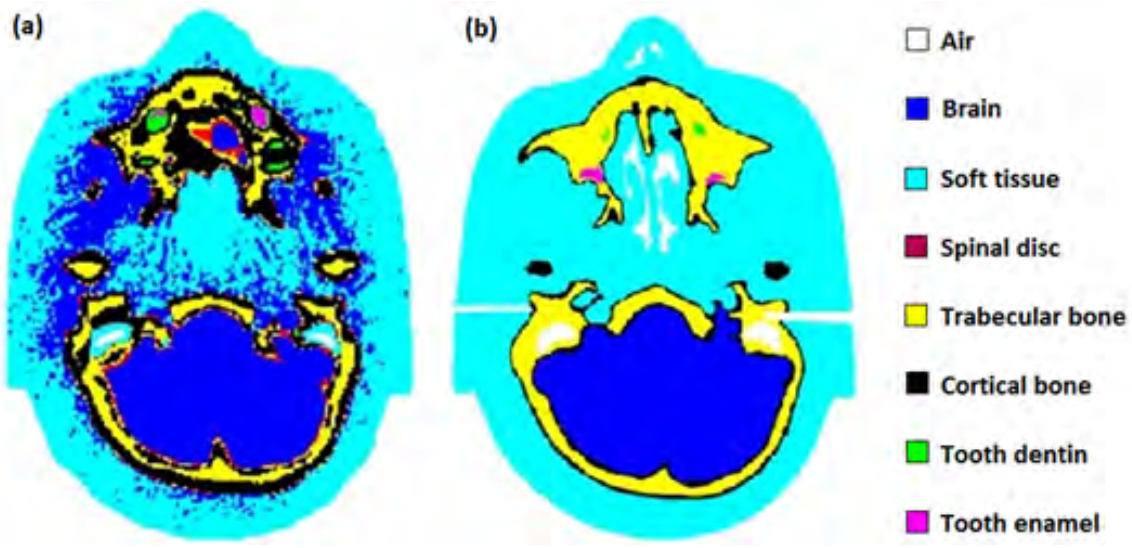

Figure 6.7: (a) `ConvHead` and (b) `HighResHead`, visualized in Geant4.

accurate reconstruction of RSP values when simulating the pCT scanner as shown in Table 6.2. On average, the RSP improved by 1.4% when using the `HighResHead`. The reconstructed RSP of different tissue-equivalent materials when compared to RSP reconstructed from experimental pCT data was within 1.5% for the `HighResHead` and 4.9% for the `ConvHead`.

6.4.1.2 `HighResHead` vs `ConvHead` - Discussion

The use of the `HighResHead` in the application of simulating the performance of a preclinical proton CT scanner led to an improvement of the resolution of the reconstructed RSP compared to experimental data by a factor 2 when compared to the version of the phantom created with standard voxel size. Thus, the phantom is more suitable representing the real-world phantom in that simulation application.

Having a counterpart in the real world has the advantage that performance of an experimental CT system can be predicted and optimized in the virtual world before the actual scanner is being built or as part of an iterative process of simulations and obtaining real-time data with stepwise improvement of the scanner hardware. The simulated data are also help-

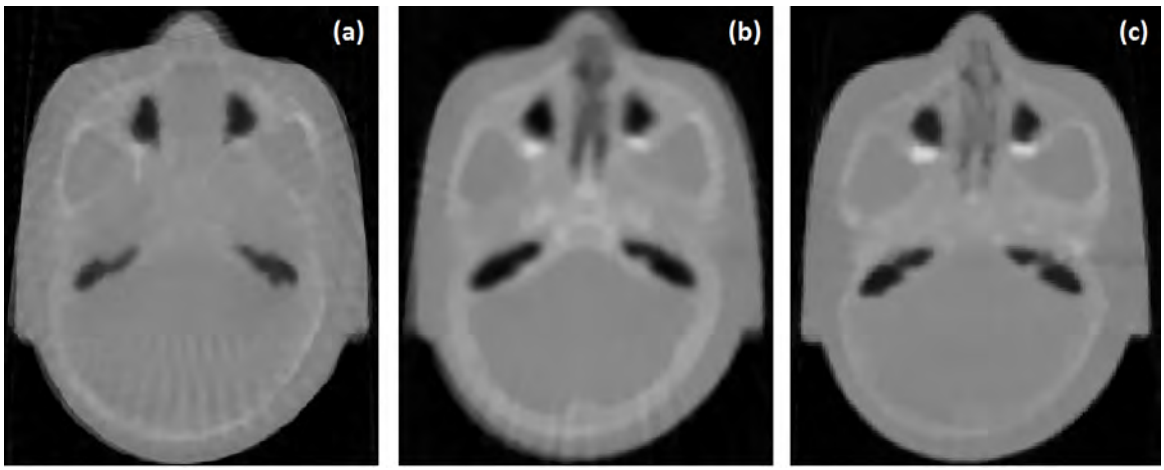

Figure 6.8: pCT image reconstruction of (a) simulated `ConvHead` (b) simulated `HighResHead` and (c) experimental real phantom. The visible radial strikes are reconstruction imaging artefacts.

Table 6.2: Comparison between mean ± standard deviation (SD) of RSP values derived from experimental data and simulated data of the anthropomorphic pediatric head phantom.

	Experimental RSP	*Simulated* `ConvHead`		*Simulated* `HighResHead`		
Material	Mean ± SD	Mean ± SD	Difference [%][1]	Mean ± SD	Difference [%][2]	RSP Difference [%][3]
Soft Tissue	1.032 ± 0.025	1.025 ± 0.018	-0.7	1.026 ± 0.014	-0.6	-0.1
Brain Tissue	1.044 ± 0.008	1.038 ± 0.012	-0.6	1.043 ± 0.012	-0.1	-0.5
Spinal Disc	1.069 ± 0.017	1.089 ± 0.025	1.9	1.053 ± 0.039	-1.5	3.4
Trabecular bone	1.111 ± 0.008	1.122 ± 0.028	1.0	1.110 ± 0.020	-0.1	1.1
Cortical bone	1.331 ± 0.032	1.288 ± 0.046	-3.2	1.312 ± 0.082	-1.4	-1.8
Tooth Dentin	1.524 ± 0.122	1.551 ± 0.089	1.8	1.521 ± 0.080	-0.2	2.0
Tooth Enamel	1.651 ± 0.050	1.732 ± 0.078	4.9	1.640 ± 0.064	-0.7	5.6

[1] (simulated$_{\texttt{ConvHead}}$ - experimental) / experimental
[2] (simulated$_{\texttt{HighResHead}}$ - experimental) / experimental
[3] (simulated$_{\texttt{ConvHead}}$ - simulated$_{\texttt{HighResHead}}$) / experimental

ful in analysing and understanding the origin of real-world reconstruction artefacts. Having an accurate representation of the real-world phantom in the Geant4 simulation turned out to be very helpful in this respect. For example, the precision of the MLP algorithm could be tested knowing the exact position of the protons inside of the simulated phantom, the image artefacts could be analysed comparing experimental, simulated and ideal (simulated) energy detector, the dose deposited inside the phantom could be calculated, etc.

A modified version of the commercial phantom 715-HN (CIRS) with a film stack insert in the posterior fossa also exists for range error measurements in proton therapy. Range error experiments can be simulated ahead of time in the corresponding modified version of the `HighResHead`.

6.4.2 Head Phantom - Image Reconstruction

The HN715 pediatric head phantom was used to compare the reconstructed simulated and experimental RSP values of a realistic anatomical object with each other and with theoretical values based on Bethe Bloch theory.

Theoretical absolute stopping power values of each head phantom material and water were determined using a separate Geant4 simulation. Note that Geant4 uses Bethe Bloch theory to calculate the energy loss of protons when their kinetic energy is higher than 2 MeV[5]. Monoenergetic protons were tracked inside of a cubic volume. The threshold of production of secondary particles was high enough not to generate delta electrons, and energy loss fluctuation was not included in the simulation. This procedure to calculate the stopping power is described in[114]. The stopping power was calculated as the ratio between energy deposited and the step length in the first step of protons for initial kinetic energy between E_0 = 100 MeV and E_1= 210 MeV using equally spaced intervals of 0.5 MeV. The stopping power calculated for each energy was then fitted with a fourth-degree polynomial,

which was integrated to obtain the energy-averaged stopping power $< SP_{\text{theo}} >$:

$$< SP_{\text{theo}} >= \frac{\int_{E_0}^{E_1} SP(E)dE}{\int_{E_0}^{E_1} dE} \tag{6.2}$$

This simulation was performed for each phantom material and water. The energy-averaged theoretical RSP for each material ($< RSP_{\text{theo material}} >$) was then calculated as:

$$< RSP_{\text{theo material}} >= \frac{< SP_{\text{theo material}} >}{< SP_{\text{theo water}} >} \tag{6.3}$$

As before, the RSP calculated from reconstructed simulated and experimental data was determined using ImageJ with the same procedure used for the CTP404 sensitometry module. Since some material regions in the head phantom, e.g. enamel and cortical bone, had very limited spatial extension, RSP was calculated by combining the results from several reconstructed CT slices (typically from 5 - 10 slices). For each selected tissue material region, mean RSP and standard deviation were calculated.

6.4.3 Head Phantom - Image Reconstruction Analysis

Fig. 6.9 shows representative reconstructed images of the pediatric head phantom using simulated and experimental data, respectively (slices thickness 1.25 mm, reconstructed field of view 24 cm, pixel size 0.9 mm). Table 6.3 shows the comparison between experimental and simulated reconstructed RSP values of the solid tissue equivalent materials of the pediatric head phantom. The agreement between simulated and experimental reconstructed RSP was found to be within 1.5%. Cortical bone and spinal disc simulated and experimental RSPs present a 1.4% of discrepancy. The cortical bone and enamel are very thin (1-2 mm), thus making it very difficult to select homogeneous regions to measure its RSP. Moreover, due to limited spatial resolution, such small regions are not resolved, so the reconstructed RSP values are much lower than the theoretical values due to partial volume averaging with

surrounding soft or brain tissue. The spinal disc was difficult to distinguish from brain in the reconstructed images causing more uncertainty in its RSP values.

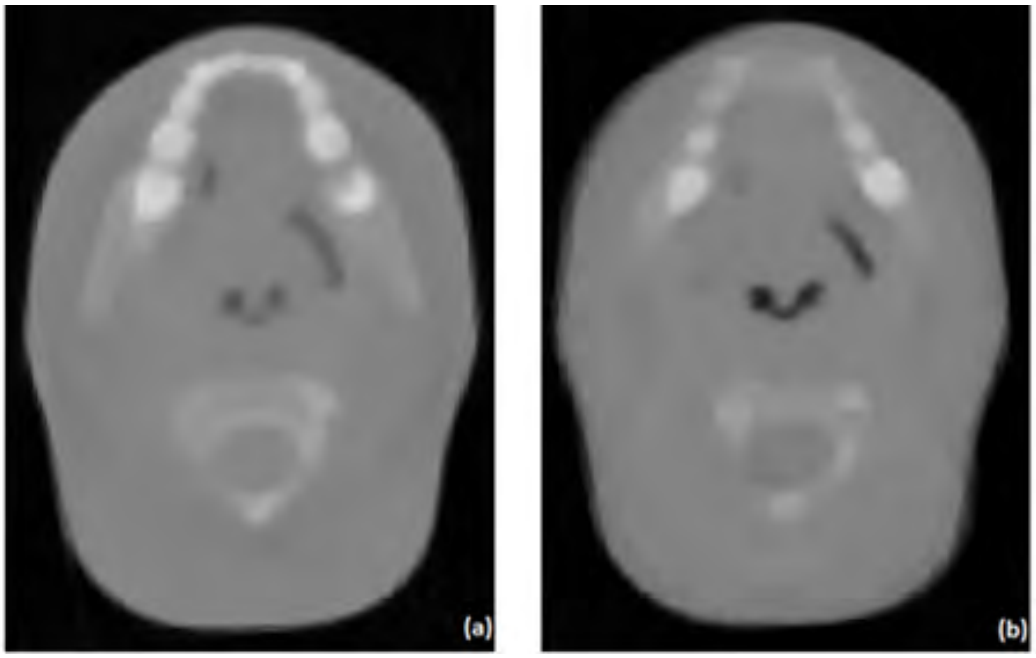

Figure 6.9: Representative head phantom pCT images reconstructed using experimental (a) and simulated (b) data.

6.5 Simulated dosimetric study

Dose, image quality, and range prediction accuracy are closely related; therefore the calculation of the dose delivered during a pCT scan is crucial for characterizing a pCT scanner. Given that the relevant energy range for pCT is 100-250 MeV[69], the Bragg peak does not occur in the scanned phantom, therefore the deposited dose is minimal in the patient. In 2013 Testa et al.[115] conducted a study in which the dose rate produced in a medium was used to identify a unique pattern in time at each point along the beam path thus finding the WEPL and reconstructing the image. They calculated that the dose required to produce a proton radiographic image with their setup was approximately 0.7 cGy.

The Geant4 simulation developed for the pCT software simulation platform described in

Table 6.3: Comparison between RSPs reconstructed from experimental and simulated reconstructed data for the anthropomorphic pediatric head phantom. The theoretical RSP was calculated using equation 6.3.

		Reconstructed RSP (experimental)		*Reconstructed RSP (simulated)*		
Material	Theoretical RSP	Mean ± SD	Difference [%][1]	Mean ± SD	Difference [%][2]	Difference [%][3]
Soft Tissue	1.037	1.032±0.025	-0.52	1.026±0.014	-1.10	-0.58
Brain Tissue	1.047	1.044±0.080	-0.25	1.043±0.012	-0.35	-0.10
Spinal Disc	1.060	1.069±0.017	0.81	1.053±0.039	0.70	-1.50
Trabecular Bone	1.108	1.111±0.008	0.26	1.110±0.020	0.17	-0.09
Cortical Bone	1.585	1.331±0.032	-16.03	1.312±0.082	-17.23	-1.43
Tooth Dentin	1.513	1.524±0.122	0.72	1.521±0.080	0.52	-0.20
Tooth Enamel	1.788	1.651±0.050	-7.68	1.640±0.064	-8.29	-0.67

[1] (experimental - theoretical)/theoretical
[2] (simulated - theoretical)/theoretical
[3] (simulated - experimental)/experimental

chapter 5, was here used to study the dosimetric performance of the prototype pCT scanner described in chapter 3.

10^6 protons per projection incident on the Catphan CTP554 16 cm acrylic dose phantom (The Phantom Laboratory, Greenwich, NY) representing a human head, were simulated, and the dose to water deposited in the centre and 4 peripheral locations was calculated (Fig. 6.10). This phantom is a standard phantom used for calculating the computed tomography dose index (CTDI) for quality assurance of CT scanners[116]. The phantom was placed at the centre between the tracking planes (isocentre) and rotated on a vertical axis in discrete steps of 4 degrees, using the same set-up adopted for reconstructing sensitometry CTP404 module, linepair CTP528 module and head phantom.

As term of comparison, the effective source spectrum and full bow-tie filter attenuation of a Varian OBI CBCT scanner[117] were used as input for a second Geant4 simulation. Since the energy spectra was provided by the authors, it was not necessary to model any beam line. The Geant4 version (10.1) and Geant4 physics list were the same as in the pCT software platform Geant4 simulation (chapter 5). Photons were incident on the phantom and, again, the dose to water deposited in the centre and 4 peripheral locations of the dose

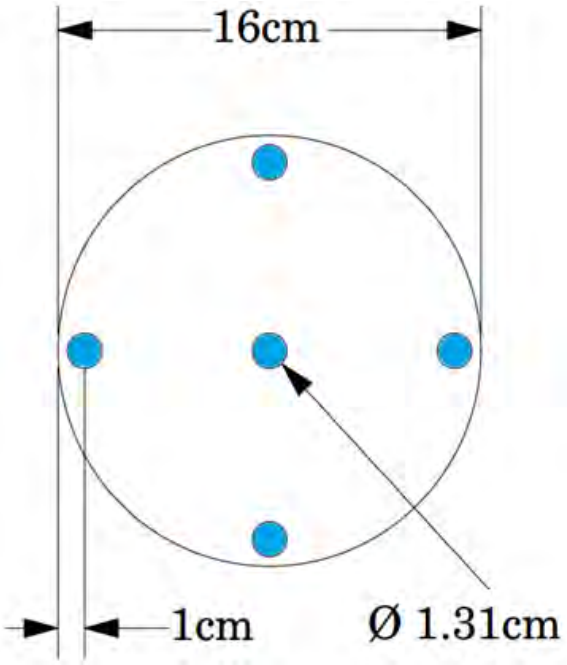

Figure 6.10: Schematic representation of the Catphan CTP554 16 cm acrylic dose phantom (The Phantom Laboratory, Greenwich, NY) representing a human head, used to measure the dose to water in the simulated pCT scans. The blue circles indicate the centre and the 4 peripheral locations where the dose to water was calculated.

phantom was calculated.

In the simulated CBCT scan, the low-dose head protocol (100 kVp, 360mAs, 36 sec scan, 20ms pulse width) was adopted according to[117].

Preliminary experimental measurements started recently to be conducted at the Northwestern Medicine Chicago Proton Center (NMCPC) in Warrenville (Illinois) to determine the dose delivered during a pCT examination.

6.6 Simulated dose results

Fig. 6.11 shows the reconstructed images of the Catphan sensitometry module. In the simulated pCT scan, 90 projections with 200 MeV protons were acquired with a central fluence of $\sim$100 protons/mm^2, typical a high-quality (low noise) pCT scan. The representative OBI CBCT image of the same phantom and similar image quality (noise) was taken from[118].

The absorbed dose to water at the central location and the average dose at the 4 peripheral locations of the dose phantom is shown in Table 6.4. For CBCT, a standard head protocol with an angular coverage of $204°$ and a full bow-tie filter was assumed[117].

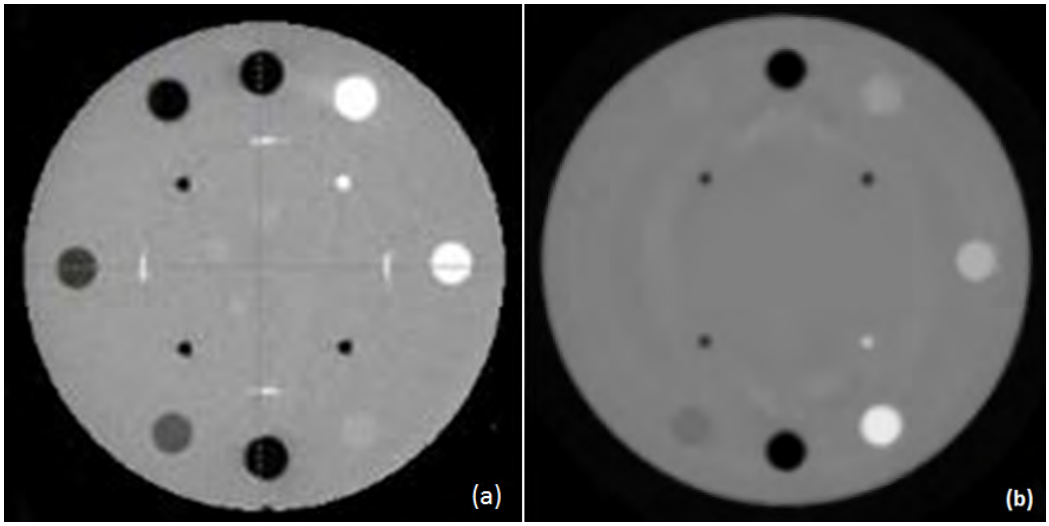

Figure 6.11: Catphan® 600 sensitometry module reconstructions: (a) OBI CBCT scan (taken from[118]); (b) pCT scan (simulation). The high-density lines in the CBCT scan correspond to metal wires not included in the pCT simulation.

Table 6.4: Comparison of the absorbed dose at central and peripheral dose phantom locations in pCT and CBCT head phantom scans. Thedose is calculated by means of Geant4 simulations.

	pCT dose [mGy]	CBCT dose [mGy]
Centre	0.37	4.6
Periphery (average)	0.30	4.4

6.7 Discussion

The RSP values of materials inside the different scanned objects reconstructed from experimental and simulated data agreed to better than 1.5%. The reconstructed RSP values from data created by the Geant4 simulation with the pCT software platform were found in good agreement with theoretical RSP values, except for those materials that suffered from partial volume effects due to small geometric dimensions (dentine and cortical bone in the head

phantom). The spatial resolution limit was of the order of 5 lp/cm for both experimental and simulated reconstructions with good agreement between the MTF of both modalities, demonstrating that the simulation correctly reproduces the factors limiting the spatial resolution of pCT reconstruction, in particular multiple Coulomb scattering in the object and the silicon planes.

The validation results presented here show a good agreement between experimental and simulated data, demonstrating that the simulation can accurately reproduce the performance of the actual pCT scanner.

The simulated dose deposited during a full pCT at LLUMC was also calculated and compared with the dose deposited during a CBCT, adopting the standard low-dose head protocol[117]. The simulated results show that the dose deposited in a pCT scan is approximately 10 times lower than with CBCT.

Preliminary experimental dose measurements recently started to be performed at NMCPC. The Catphan CTP554 16 cm acrylic dose phantom was used to measure the dose to water during a typical pCT scan, as done in the simulated dosimetric study. The preliminary experimental dose to water, after the background correction, was 1.46 mGy in the peripheral location and 1.48 mGy in the central location (practically uniform across the phantom). The simulated dose calculated in this work is lower than the preliminary experimental one. This can be attributed to different exposure times and incident proton beam characteristics. Future work, which will not be part of the PhD project presented, includes modelling and implementation of the NMCPC beam line in the pCT software platform.

6.8 Conclusion

In this work, validation of the image reconstruction module of the pCT software platform described in chapter 5 was performed.

The validated pCT software platform described in chapter 5 is a versatile tool for pCT

performance and application studies. The platform is flexible and can be modified to simulate not just existing versions of pCT scanners but also higher proton energies than those currently clinically available. In particular, in this chapter, the pCT software platform was used to conduct a dosimetric study on the pCT scanner prototype.

Chapter 7

A Medipix Study of Proton Paths Through Heterogeneous Materials During pCT Data Acquisition

7.1 Introduction

In the previous chapters pCT was presented as an imaging technique that provides RSP of protons for better proton range accuracy in treatment planning than currently possible with xCT based planning[2].

For image reconstruction purposes, the path of a proton through the scanned object has to be estimated knowing entrance and exit position of that proton. The MLP of each proton history is in fact used by iterative reconstruction techniques such as algebraic reconstruction techniques (ART)[119] or parallelizable algorithms[107] to reconstruct the traversed object. As mentioned in chapter 2, the main limiting factor for pCT spatial resolution is MCS. MCS impacts the correctness of the estimation of proton MLP, therefore it is necessary to have an MLP algorithm that takes this into account.

Currently, all existing MLP formalisms[6,105,120] are based on the assumption of homo-

geneous medium (water), which is not generally valid when imaging patients.

It is well know that protons scatter more in heterogeneous medium because of the change in density at the interface between two adjacent materials and Sawakuchi et al.[121] proved that the Bragg peak degradation is mainly caused by MCS at the interface between two different tissues.

In this chapter, we report on the use of the pixelated Medipix detector to study the effect of heterogeneities on the accuracy of the MLP. Medipix detectors have been previously used for ion beam therapy studies[122] . In this work the Medipix was successfully integrated with the experimental prototype pCT scanner built by the pCT collaboration[4] and described in chapter 3.

7.2 Materials and Methods

7.2.1 Medipix Detector

The Medipix is a pixelated detector that consists of a semiconductor sensor chip which is made of one of several different materials (Si, GaAs, CdTe, Y) and is bonded to a readout chip. In particular, a 256×256 square pixels matrix is connected by the bump-bonding technique to a readout ASIC chip containing an amplifier, two discriminators and a 13-bit counter for each pixel[123]. The pixel size is 55 μm. Each pixel can work in one of three modes: Medipix mode (counting incoming particles), Timepix mode (the counter works as a timer and measures the time when the particle is detected) and Time Over Threshold (TOT) mode (the counter allows direct energy deposited measurement in each pixel)[124].

The Medipix used in this study consisted of a 150 μm silicon detector chip operated in the Timepix mode. The detector was configured to receive an outside trigger to start recording data. The trigger was given by the first scintillator stage of the multistage detector of the pCT scanner. Medipix frames were recorded for a time interval of 1 ms; each frame

contained the coordinates of the hit pixels and the time when the hit occurred.

Pixelman[125] was the software package used to control the Medipix data acquisition.

7.2.2 Experimental Setup

A custom made PMMA plate was built to hold the Medipix in one of 5 different locations between the tracking planes. Several measurements were performed inserting the Medipix between different tissues equivalent slabs (CIRS, Norfolk, VA) to determine the proton path and the accuracy of the MLP estimate in heterogeneous objects (Fig. 7.1). In particular, a human chest configuration was created by symmetrically arranging slabs of cortical bone, soft tissue, and lung on either side of the phantom centre; a human head configuration was created by symmetrically arranging slabs of cortical bone, soft tissue, trabecular bone and brain. Additional measurements were performed for the same locations but using only one type of tissue equivalent slabs: lung, brain, soft tissue, or cortical bone. The configurations used in this experiment are summarised in Table 7.1, including the slabs thickness's.

The Medipix was located at the centre of each configuration, specifically (1.3 $\pm$ 0.5) mm upstream from the isocentre. The exact horizontal and vertical positions of the Medipix were (29.90 $\pm$ 0.01) mm right of the beam centre and (0.10 $\pm$ 0.01) mm below the beam centre.

The output of the experiment consisted in:

- pCT bit stream output consisting of:
    1. the coordinates of the proton hits in the tracking planes (measured in mm);
    2. the energy deposited in the multistage energy detector;
    3. the timestamp of each proton traversing the tracking planes.
- Pixelman output consisting of:

Table 7.1: Slabs configurations. B stands for brain, L for lung, CB for cortical bone, ST for soft tissue, TB for trabecular bone

Configuration Name	Run	Configuration Description
Empty	43	Medipix at centre, nothing else
B1	44	Medipix + 8 cm B
B2	47	8 cm B + Medipix + 8 cm B
B3	48	8 cm B + Medipix
L1	52	Medipix + 5 cm L
L2	53	5 cm L + Medipix + 5 cm L
L3	54	5 cm B + Medipix
CB-ST1	59	1 cm CB + 5 cm ST + Medipix
CB-ST2	60	5 cm ST + 1 cm CB + Medipix
CB-ST3	61	Medipix + 1 cm CB + 5 cm ST
CB-ST4	62	Medipix + 5 cm ST + 1 cm CB
Chest	55	1 cm CB + 2 cm ST + 7 cm L + Medipix + 7 cm L + 2 cm ST + 1 cm CB
Head	58	1 cm CB + 0.2 cm ST + 3 cm TB + 8 cm B + Medipix + 8 cm B + 3 cm TB + 0.2 cm ST + 1 cm CB

1. the coordinates of the proton hits in Medipix (measured pixel number); note that the pixels are numbered from 1 to 256 in x and y direction;
2. the timestamp of each proton traversing the detector.

PCT and Medipix timestamps were used to match the events recorded by the two systems.

During the data collection, the scattering lead foil placed immediately after the SEM exit window to spread the proton beam, was removed (Fig. 5.2). In fact, the Medipix size is very small compared to the size of the tracking planes therefore a scattered beam was not necessary.

7.2.2.1 Medipix and pCT data collection

The pCT DAQ sent a trigger to the Medipix when detecting a proton. The Medipix opened a frame to accumulate events for 1 ms, and sent a busy signal back to pCT. pCT continued taking data for 1 ms but it set a flag on the event that opened the frame, to know the starting frame on the pCT side. The pCT waited for the Medipix readout to finish (i.e. it waited for the busy signal to be removed), and then it waited another extra 10 ms (extra safety margin).

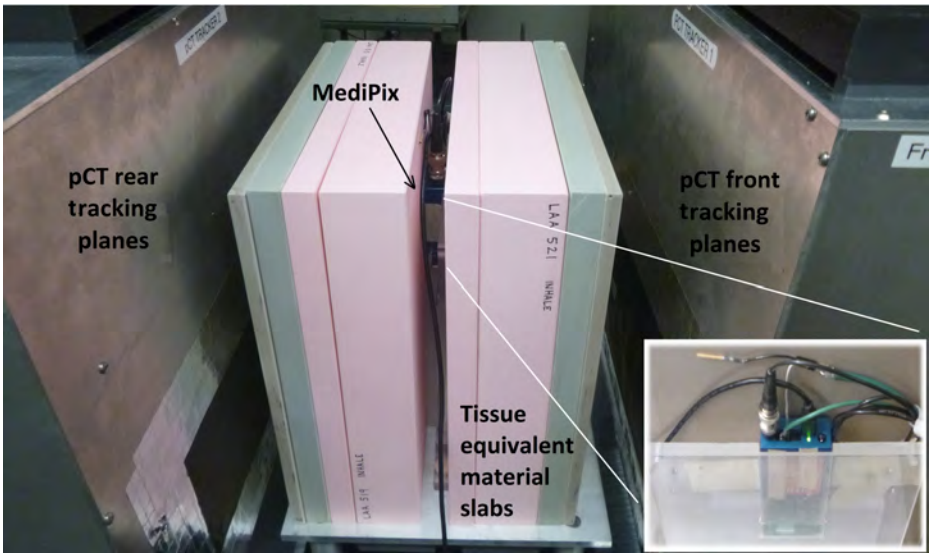

Figure 7.1: Experimental setup for the Medipix-pCT study. Here the Medipix was located in the center of the slab phantom between 2 slabs of lung (7 cm), 1 slab of soft tissue (2 cm) and 1 slab of cortical bone (1 cm), forming the "chest configuration". The figure insert shows how the Medipix was positioned.

Several empty runs were performed before starting the data collection in order to check that the number of triggers transmitted to the Medipix by the pCT scanner corresponded to the number of frames recorded by the Medipix.

The timestamp recorded in each Medipix pixel corresponds to the time interval from when the protons hit the pixels until when the Medipix frame is closed and it is measured in clock cycle (9.6 Mhz per clock). The Medipix accumulated events for 1 ms (approximately 9600 clocks) to prevent pixels from reaching the saturation.

The data collected from pCT scanner and Medipix detector were synchronized. The synchronization was based on the time of the occurrence of the events. The Medipix time recorded in clock cycle was converted into seconds in order to match the timestamp provided by the pCT scanner.

When a proton hit the Medipix, it usually deposited enough energy to generate a cluster of hit pixels. The cluster size depends on the energy deposited by the proton: the larger the energy deposited, the larger the cluster. The center of gravity of each cluster was calculated and associated to a pCT event according to the timestamp recorded.

The pixels presenting a high number of counts for every run (*hot spot*), independently from the configuration chosen, were neglected (*masked*). They correspond to noisy pixels that are for some reasons damaged and always receiving a signal. The "masked" pixels must be neglected because they represent false positive results.

7.2.2.2 Medipix Calibration

Once the matching pixel were identified, two calibration curves were created to find the correspondence between pixel number and coordinates, in mm. The calibration curves were obtained plotting the coordinates of the hits in the pCT trackers and the respective pixel number of the hits in the Medipix. The data used for the calibration were collected during an empty run (empty configuration) and the hit coordinates of the front tracking plane were used. The plot was fit with a straight line and the equation of the line was used to convert pixel numbers in mm in every configuration set up .

7.2.3 Geant4 Modeling of the Medipix

The medipix-pCT system was modelled in the Geant4 simulation included in the pCT software platform described in chapter 5. 5×10^3 proton histories were generated per each scan and the scanned phantoms were the slabs configurations described in Table 7.1.

The output of the simulation consists of:

1. the coordinate of the proton hits in the tracking planes (measured in mm);

2. the coordinate of the proton hits in Medipix (measured in mm).

Note that with the simulated data, the Medipix calibration was not necessary anymore since the coordinates of the Medipix hit were retrieved directly.

7.2.4 Most Likely Path

7.2.4.1 Most Likely Path formalism

Several approaches describe the calculation of the MLP of charged particles, and protons in particular, in literature[6,105,120]. For the MLP study presented in this chapter, the approach described by R. W. Schulte et al.[6] was used since that is the formalism adopted in the image reconstruction algorithm for the phase II pCT scanner prototype.

This statistical formalism is based on the assumption that protons traverse a reconstruction volume made of water. Considering position and direction of protons entering and exiting the object, it is possible to estimate the lateral displacement and direction at any depth in the object.

In particular, $y_0 = (t_0, \theta_0)$, $y_2 = (t_2, \theta_2)$ and $y_1 = (t_1, \theta_1)$ are respectively the position and direction calculated at the entrance position u_0, at the exit position u_2 and at any positions u_1. Fig. 7.2 shows a schematic example of these positions.

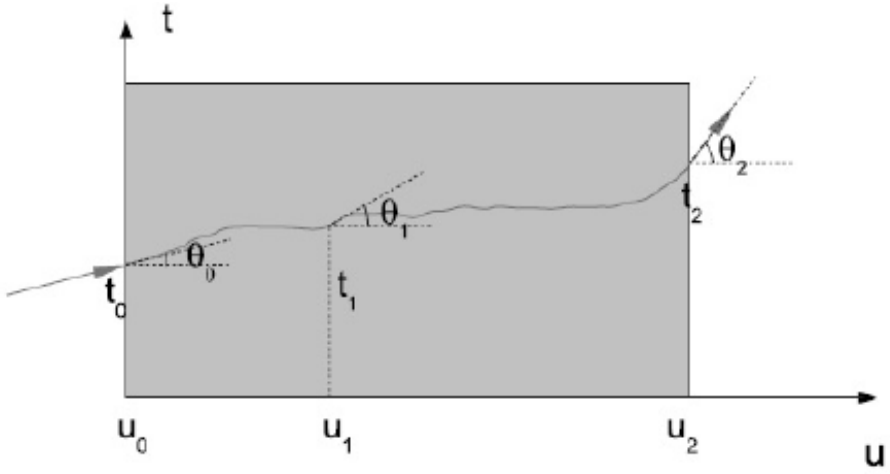

Figure 7.2: Schematic of the MLP formalism.

In Bayesian statistics, the prior likelihood $L(y_1|entry\ data)$ and the posterior likelihood $L(y_1|exit\ data)$ can be combined according to Bayes' theorem:

$$L(y_1|exit\ data) = L(exit\ data|y_1)L(y_1|entry\ data) \tag{7.1}$$

Maximizing $L(y_1|exit\ data)$, it is possible to find the MLP of a particle as:

$$y_{MLP} = (\Sigma_1^{-1} + R_1^T \Sigma_2^{-1} R_1)^{-1} (\Sigma_1 R_0 y_0 + R_1^T \Sigma_2^{-1} y_2) \tag{7.2}$$

The scattering matrix are:

$$\Sigma_1 = \begin{pmatrix} \sigma_{t_1}^2 & \sigma_{t_1\theta_1}^2 \\ \sigma_{t_1\theta_1}^2 & \sigma_{\theta_1}^2 \end{pmatrix} \tag{7.3}$$

$$\Sigma_2 = \begin{pmatrix} \sigma_{t_2}^2 & \sigma_{t_2\theta_2}^2 \\ \sigma_{t_2\theta_2}^2 & \sigma_{\theta_2}^2 \end{pmatrix} \tag{7.4}$$

The elements of the scattering matrix correspond to the variance and covariance of t_1 and θ_1 calculated. They depend on the depth of the proton and on the energy loss.

$$\sigma_{t_1}^2(u_0, u_1) = E_0^2 \left(1 + 0.038 \ln\frac{u_1 - u_0}{X_0}\right)^2 \times \int_{u_0}^{u_1} \frac{(u_1 - u)^2}{\beta^2(u)p^2(u)} \frac{du}{X_0} \tag{7.5}$$

$$\sigma_{\theta_1}^2(u_0, u_1) = E_0^2 \left(1 + 0.038 \ln\frac{u_1 - u_0}{X_0}\right)^2 \times \int_{u_0}^{u_1} \frac{1}{\beta^2(u)p^2(u)} \frac{du}{X_0} \tag{7.6}$$

$$\sigma_{t_1\theta_1}^2(u_0, u_1) = E_0^2 \left(1 + 0.038 \ln\frac{u_1 - u_0}{X_0}\right)^2 \times \int_{u_0}^{u_1} \frac{u_1 - u}{\beta^2(u)p^2(u)} \frac{du}{X_0} \tag{7.7}$$

$$\sigma_{t_2}^2(u_1, u_2) = E_0^2 \left(1 + 0.038 \ln\frac{u_2 - u_1}{X_0}\right)^2 \times \int_{u_1}^{u_2} \frac{(u_2 - u)^2}{\beta^2(u)p^2(u)} \frac{du}{X_0} \tag{7.8}$$

$$\sigma_{\theta_2}^2(u_1, u_2) = E_0^2 \left(1 + 0.038 \ln\frac{u_2 - u_1}{X_0}\right)^2 \times \int_{u_1}^{u_2} \frac{1}{\beta^2(u)p^2(u)} \frac{du}{X_0} \tag{7.9}$$

$$\sigma_{t_2\theta_2}^2(u_1, u_2) = E_0^2 \left(1 + 0.038 \ln\frac{u_2 - u_1}{X_0}\right)^2 \times \int_{u_1}^{u_2} \frac{u_2 - u}{\beta^2(u)p^2(u)} \frac{du}{X_0} \tag{7.10}$$

where $E_0 = 13.6\mathrm{MeV}/c$ is an empirical constant and $X_0 = 36.1\ \mathrm{cm}$ is the radiation length of water[126].

The rotation matrices are expressed as:

$$R_0 = \begin{pmatrix} 1 & u_1 - u_0 \\ 0 & 1 \end{pmatrix} \tag{7.11}$$

$$R_1 = \begin{pmatrix} 1 & u_2 - u_1 \\ 0 & 1 \end{pmatrix} \tag{7.12}$$

$1/\beta^2(u)p^2(u)$ was estimated using a fifth degree polynomial curve fitting the results of a Geant4 simulation retrieving position and kinetic energy of 200 MeV protons traversing a uniform water phantom[119].

$$\frac{1}{\beta^2(u)p^2(u)} = \frac{(E(u) + E_p)^2 c^2}{(E(u) + 2E_p)^2 E^2(u)} \tag{7.13}$$

Since vertical and lateral scattering can be considered as two independent statistical processes, the derivation of the MLP can be calculated for each plane independently.

7.2.4.2 Most Likely Path calculation

In this study, the coordinates of the hits at entrance and exit tracking planes were used to reconstruct the proton MLP. The reconstruction volume selected was a cube with a side length of 26 cm, which corresponds to the largest thickness configuration set up experimentally built. The proton path between the trackers and the reconstruction volume was assumed to be a straight line, since protons travelled in air. The MLP was reconstructed for discrete depths within the reconstruction volume. Knowing the depth at which the Medipix is located, the coordinates of the hits on the Medipix were predicted using the MLP formalism. For both horizontal and vertical coordinates, the accuracy of the prediction was calculated

as:

$$\Delta(MLP) = MLP_{\text{measured}} - MLP_{\text{predicted}} \tag{7.14}$$

Equation 7.14 was used to calculate $\Delta(MLP)$ both for simulated ($\Delta(MLP)_{\text{sim}}$) and experimental ($\Delta(MLP)_{\text{exp}}$) data. A Gaussian fit was then applied to the distribution of $\Delta(MLP)$ and mean and standard deviation were calculated.

To further quantify the accuracy of the predicted coordinates, the correlation coefficient between MLP_{measured} and $MLP_{\text{predicted}}$ was also calculated.

7.3 Results

7.3.1 Accuracy of the predicted MLP

The set up of the Geant4 simulation used to calculate the fifth degree polynomial curve fitting $1/\beta^2(u)p^2(u)$ was briefly described in section 7.2.3.

Fig. 7.3.a represents the proton energy loss by 200 MeV protons when traversing an increasing thickness of water as calculated by means of the pCT Geant4 simulation. Fig. 7.3.b represents the correspondent $1/\beta^2(u)p^2(u)$ curve.

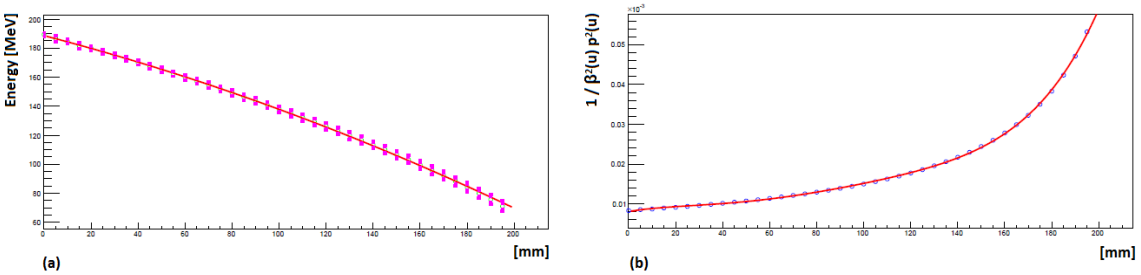

Figure 7.3: (a) Energy loss by 200 MeV protons when traversing an increasing water thickness in the simulation set-up described in section 7.2.3. (b) $1/\beta^2(u)p^2(u)$ curve obtained using the energy plotted in (a).

7.3.2 Experimental results

7.3.2.1 Medipix and pCT synchronization and calibration

Several empty runs were performed to test the correspondence between the number of triggers transmitted to the Medipix by the pCT scanner and the number of frames recorded by the Medipix.

Initially, approximately half of the trigger signals were not detected by the Medipix. This problem was solved making the pCT trigger signal 3 times longer. Afterwards the agreement between number of triggers transmitted and number of frames recorded was 100%.

Fig. 7.4 shows the matching events measured during an empty run. Fig. 7.4.a shows all the hits recorded in the front tracking plane while Fig. 7.4.b shows the matching hits between Medipix and tracking plane. Approximately 4% of the total recorded events were measured by the Medipix. This can be explained by the fact that the area of the Medipix is approximately 100 times smaller than the sensitive area of the tracking planes.

Fig. 7.5.a shows the clusters of pixel hit while figure 7.5.b shows the correspondent centres of gravity retrieved for each cluster.

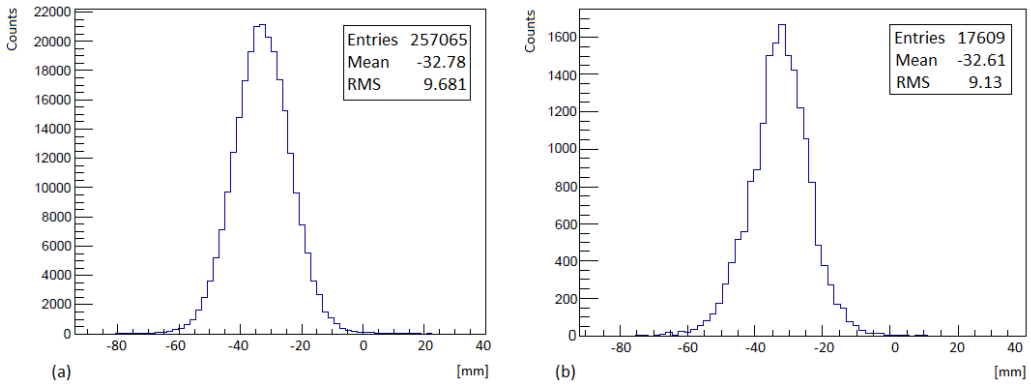

Figure 7.4: (a) Entries in the front tracker (b) Entries in the front tracker that are matching the entries in the Medipix.

Fig. 7.6 shows the calibration curve for the horizontal and vertical direction. The Medipix position was shifted 0.1 mm in the vertical direction and 2.9 cm in the horizon-

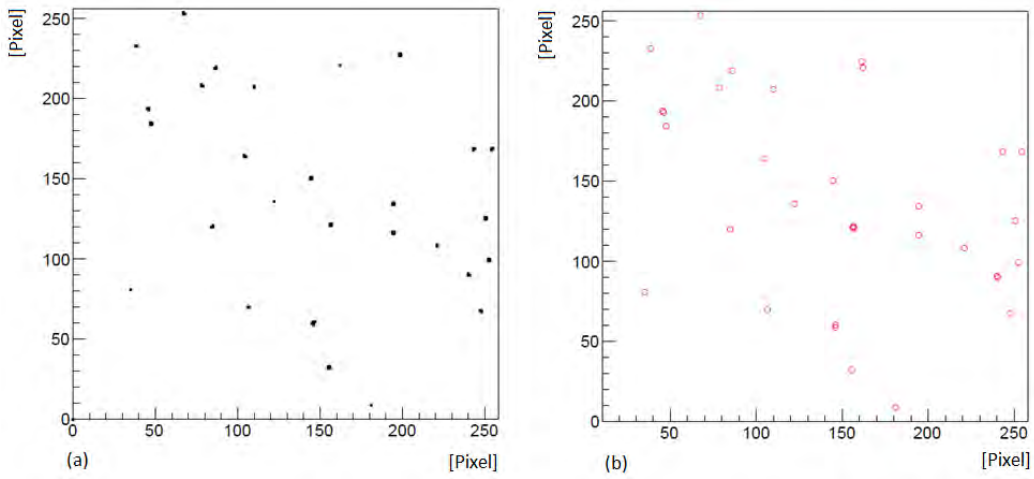

Figure 7.5: (a) Hits in the Medipix (clusters). (b) Centre of gravity of the clusters created by the hits.

tal direction as shown in Fig.. 7.6.a and Fig. 7.6.b, respectively.

The calibration curves were plotted both using front and rear trackers and the calibration coefficients variation found was less than 2%; although, the calibration curve generated using the front tracker was selected because of the lower proton scattering.

The calibration curves can be represented by the general equation of a line $y = p_1 x + p_0$. The calibration coefficients p_0 and p_1, necessary for converting pixel number in x and y coordinates, can be found in Tab. 7.2.

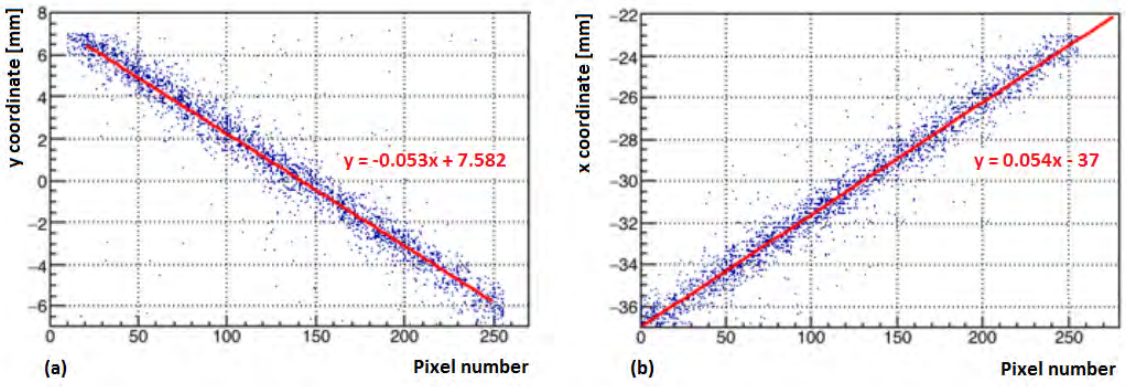

Figure 7.6: Calibration curve between pixel number and (a) vertical and (b) horizontal coordinates in mm.

Table 7.2: Calibration coefficients for x and y coordinates.

	x coordinates	y coordinates
p_0	-37.000 ± 0.035	7.582 ± 0.051
p_1	0.0538 ± 0.0003	-0.0535 ± 0.0003

7.3.3 Verification of experimental and Geant4 results with respect to theoretical calculations

Fig. 7.7 and 7.8 show the comparison between $\Delta(MLP)_{\text{sim}}$ and $\Delta(MLP)_{\text{exp}}$ for an empty run configuration and a chest configuration, respectively. The data are more spread out in the chest configuration because of the increased scattering due to the presence of the tissue equivalent slabs.

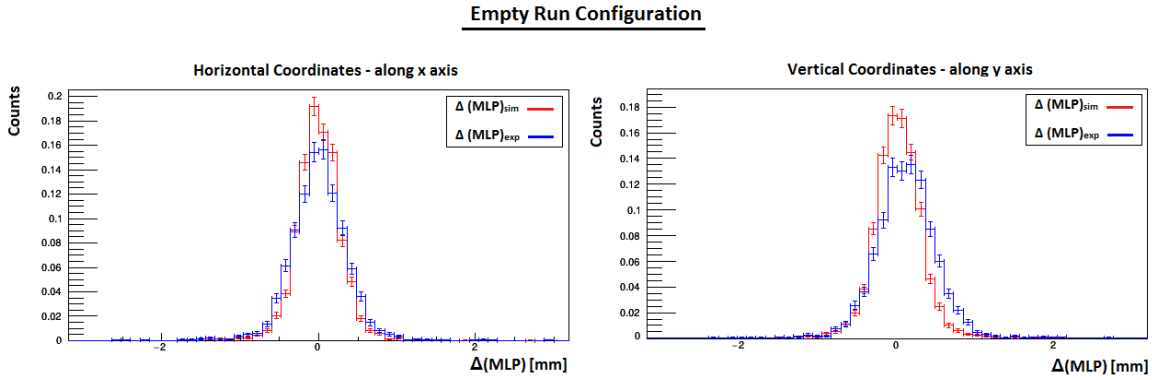

Figure 7.7: Comparison between $\Delta(MLP)_{\text{sim}}$ (red) and $\Delta(MLP)_{\text{exp}}$ (blue) in the empty configuration.

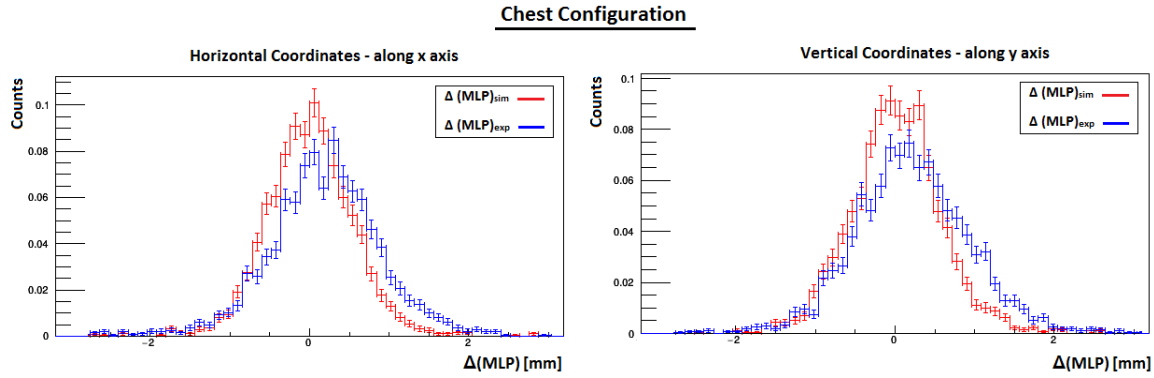

Figure 7.8: Comparison between $\Delta(MLP)_{\text{sim}}$ (red) and $\Delta(MLP)_{\text{exp}}$ (blue), in the chest configuration.

Fig. 7.9 and 7.10 shos the comparison between linear correlation of simulated and experimental data for the same empty run and chest configuration, respectively.

Table 7.3: Experimental and simulated $\Delta(MLP)$ and correlation factor along x and y axis for all the configurations of the experiment.

	Experimental				*Simulated*			
Configuration	$\Delta(MLP)_x \pm SD$	r_x	$\Delta(MLP)_y \pm SD$	r_y	$\Delta(MLP)_x \pm SD$	r_x	$\Delta(MLP)_y \pm SD$	r_y
Empty	0.004 ± 0.317	0.993	0.109 ± 0.350	0.994	0.001 ± 0.256	0.993	0.013 ± 0.269	0.994
B1	0.225 ± 0.448	0.980	0.129± 0.481	0.985	0.002 ± 0.317	0.993	0.002 ± 0.319	0.994
B2	0.291 ± 0.540	0.972	0.090± 0.581	0.975	-0.006 ± 0.483	0.982	0.006 ± 0.478	0.987
B3	0.273 ± 0.417	0.983	0.107 ± 0.429	0.987	-0.002 ± 0.443	0.987	0.008 ± 0.433	0.989
L1	0.299 ± 0.388	0.981	0.092 ± 0.434	0.987	-0.002 ± 0.255	0.995	0.003 ± 0.269	0.994
L2	0.374 ± 0.542	0.968	0.004 ± 0.564	0.979	0.004 ± 0.283	0.991	-0.004 ± 0.289	0.993
L3	0.320 ± 0.433	0.983	0.060 ± 0.458	0.989	0.006 ± 0.288	0.992	0.003 ± 0.300	0.993
CB-ST1	0.252 ± 0.415	0.984	0.178 ± 0.451	0.988	-0.012 ± 0.407	0.988	0.014 ± 0.408	0.991
CB-ST2	0.270 ± 0.413	0.982	0.150 ± 0.447	0.987	0.016 ± 0.461	0.982	0.015 ± 0.440	0.988
CB-ST3	0.293 ± 0.436	0.979	0.091 ± 0.429	0.984	-0.001 ± 0.364	0.990	-0.012 ± 0.351	0.991
CB-ST4	0.305 ± 0.399	0.988	0.149 ± 0.418	0.990	0.003 ± 0.313	0.993	-4.861e-05 ± 0.319	0.994
Chest	0.199 ± 0.650	0.974	0.213 ± 0.682	0.979	0.005 ± 0.512	0.985	0.007 ± 0.543	0.985
Head	0.215 ± 0.528	0.979	0.195 ± 0.564	0.983	0.028 ± 0.912	0.957	0.011 ± 0.972	0.957

Table 7.3 shows mean, standard deviation (SD) and correlation coefficient (r) of simulated and experimental $\Delta(MLP)$ along x and y direction for all the configurations.

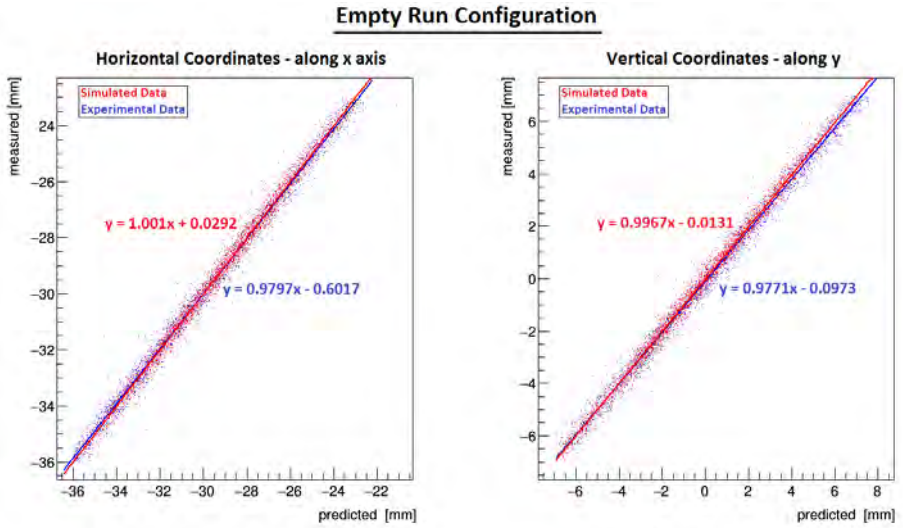

Figure 7.9: Comparison between simulated (red) and experimental (blue) correlated points during an empty run, fitted with a line of best fit.

7.4 Discussions

In this work, the integration of a Medipix pixelated detector with a prototype pCT scanner was successfully realised. The Medipix was used as an extra detector between the pCT

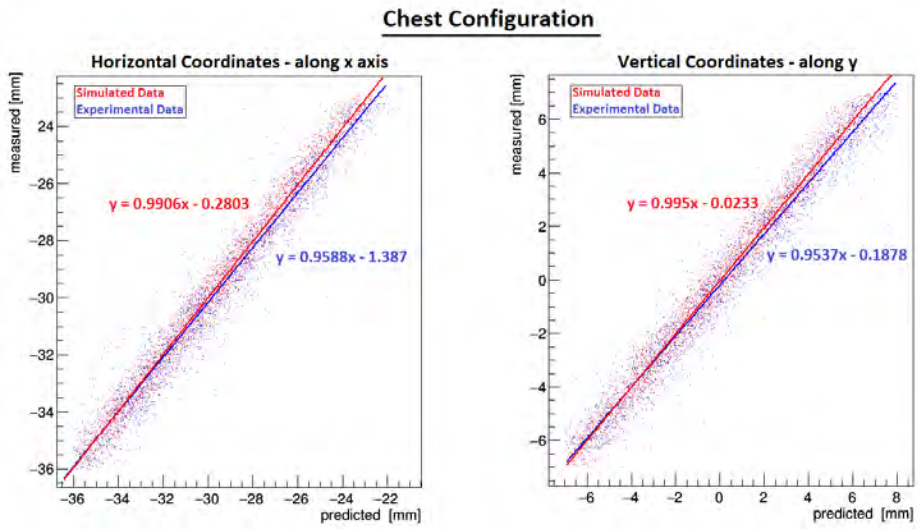

Figure 7.10: Comparison between simulated (red) and experimental (blue) correlated points in the chest configuration, fitted with a line of best fit.

tracking planes to study the proton MLP accuracy and, in particular, the effect of heterogeneities in the MLP calculation. The same experimental set up was also modelled in the Geant4 simulation described in chapter 5.

Table 7.3 summarises experimental and simulated results. The agreement between experimental and simulated results was very good: $\Delta(MLP)_{\text{exp}}$ and $\Delta(MLP)_{\text{sim}}$ always agree within one standard deviation. $\Delta(MLP)_{\text{sim}}$ is closer to zero than $\Delta(MLP)_{\text{exp}}$ denoting that the simulated MLP prediction is more accurate. The margin of error in the experimental data can be partially explained by the uncertainty of the calibrations coefficients p_0 for x and y coordinates (the uncertainty on p_1 is negligible). Moreover, there is a big uncertainty in the Medipix position along the z direction (1.3 ± 0.5) mm because of the safety measures adopted to protect the silicon detector. A rectangular circuit board with a square hole in correspondence of the silicon detector was positioned right above the pixelated detector (see Fig. 7.11) in order to protect it from hitting any objects. Therefore, even using a calliper, it is very difficult to measure the exact z coordinate of the silicon detector, i.e. the depth u where the MLP is calculated. This work evaluated for the first time experimentally the accuracy of the MLP algorithm. For the future, it is recommended to evaluate the effects of

the detector position uncertainty on the detector response.

Figure 7.11: Close-up view of the Medipix detector protection.

The correlation coefficients along vertical and horizontal direction are close to 1 for all the configurations showing a good agreement between predicted and measured data. For the configurations B2 and L2, r_x and r_y are lower than for the configurations B1, B3 and L1, L3, both for experimental and simulated data. This can be explained by the extra slab of tissue equivalent material in the latter configurations. No substantial differences were noticed in measurements with the same slabs positioned either upstream or downstream the Medipix.

These results confirm the validity of the MLP algorithm chosen since $\Delta(MLP)$ is always close to zero. A similar analysis was conducted by Wong et al.[127] using a symmetrical inhomogeneous phantom with bone, air and water slabs. The novelty of the work here reported is the use of experimental data collected with high spatial resolution pixelated detector Medipix.

7.5 Conclusions

A Medipix pixelated detector was successfully integrated a with the phase II pCT scanner prototype. The analysis of the data taken in the experiment was used to (1) analyse the accuracy of the MLP calculated based on the assumption of homogeneous water phantom while the phantom was heterogeneous, and (2) validate the Geant4 simulation of the Medipix-pCT

system to further investigate the MLP calculation during pCT image reconstruction.

The MLP algorithm was proven to be not significantly effected by heterogeneities. A possible future study derived from this work, would be the use of Medipix in a full 360° pCT scan in order to directly associate any variations in the MLP accuracy with the correspondent reconstructed image. If a substantial correlation will be found, the MLP formalism could be improved including heterogeneities once they are detected in a first reconstruction run thus leading to an improvement of the overall accuracy and spatial resolution of pCT reconstruction. It would be useful to repeat this study in the future using more realistic phantoms/geometries to have a better idea of the MLP behaviour inside of a patient.

Chapter 8

Discussions and Outlook

This thesis investigated several aspects of pCT using experimental and simulated data. In particular, the existing phase II pCT scanner prototype was modelled using MC methods: RSP accuracy, MLP correctness and dose delivered during a pCT scan were investigated.

The candidate own contribution to the work can be summarized in:

1. modelling the entire pCT system with all its modular components in a software platform;
2. modelling a high resolution digital head phantom and implementing it in the previously mentioned platform;
3. studying how to improve the calibration of the pCT system;
4. reconstructing several phantoms, both using experimental and simulated pCT data;
5. conducting preliminary measurements of the dose deposited during both an experimental and a simulated pCT scan;
6. evaluating the MLP accuracy in heterogeneous materials, both experimentally and by means of MC simulations.

The results presented in the previous chapters, however, represent just the tip of the iceberg. During this four years PhD project, considerable progress has been made. Specifically:

- the phase II pCT scanner prototype was able to operate at an event rate of $1\ \mathrm{MHz}$;
- a large area ($9\times18\ \mathrm{cm}^2$) was covered by the tracking plane with minimal loss events due to the gaps between SSDs;
- an algorithm recovering missing hits was developed in order to reduce even more the number of lost events;
- a pCT scan of an detailed anthropomorphic head phantom was performed;
- a pCT scan of a human chest was simulated implementing DICOM images in a software platform of the pCT system;
- a Medipix detector was successfully integrated and synchronized with the phase II pCT scanner prototype;
- a WEPL resolution of $2.8\ \mathrm{mm}$ was achieved;
- a RSP accuracy within 1.5% was achieved;
- a preliminary dosimetric evaluation of pCT was performed proving the dosimetric validity of pCT.

At the same time, all these encouraging results lead towards upgrades that could further strengthen the validity of pCT as an imaging technique.

8.1 Phase II pCT system: possible improvements

8.1.1 Tracking planes

Several tracking planes system already implemented in pCT were mentioned in chapter 2. In particular both scintillating fibers used at NIU and INFN[46,47,55,56] and solid state silicon micro-strip sensors (Micron Semiconductor Ltd, 150 μm) used by the PRaVDA Consortium seem to be promising detectors. In particular it is very interesting the PRaVDA solution of positioning the detectors at a 60° angle with respect to each other to precisely measure the proton hit coordinates.

Two alternative technologies that could be used for tracking protons are plasma panel sensors (PPS) and gas microstrip detectors (GMDs) but they have never been used before for this purpose so they are still under investigation. Pixelated detectors (like Medipix) could also be used as tracking device but cost and size represent currently a major issue.

The dimension of the tracking planes should also be increase in order to be able to scan bigger object, and eventually, also animals.

8.1.2 Energy detector

The 5-stage scintillator detector was chosen to improve the performance of the segmented array of thallium doped caesium iodide CsI(Tl) crystal calorimeter. The multistage detector was definitely an improvement but the trade off was that developing adequate electronics for the device and establishing a satisfactory calibration for the system was time consuming and very complicated. The range straggling was the main complication encountered, causing problems in distinguishing stopping or transiting protons near the interfaces between the stages of the detector.

A valid alternative was proposed in 1989 by Takada et al.[128] who suggested using magnetic spectrometer for pCT. This system might be too expensive but it is definitively a pos-

sibility to be explored.

The sixty polystyrene layers of scintillating fibers proposed at INFN[55,56] could be a short term more feasible solution. This system, theoretically, should also allow for high rates event acquisition therefore could be a valid alternative for replacing the multistage energy detector

8.1.3 Image reconstruction algorithm

Iterative reconstruction algorithms have proven to work very well in pCT[107]. A possible improvement in the reconstruction code currently used was proposed by Karbasi, Schultze and Schubert at Baylor University (Texas, USA). In primis, the use of space carving techniques for hull detection[129] thus replacing the currently used FBP, would reduce image blurring and artefacts. Secondly, the complete parallelization of the code would improve the reconstruction speed, doing a step forward toward the on-fly pCT image reconstruction.

Other algorithms being studied include

1. a modified FBP algorithm, which uses distance-driven-binning along the MLP, rather than a straight-line projection algorithm, in order to achieve a higher-quality image with a fast FBP-based algorithm[130];

2. a proton-attenuation algorithm which uses the proton MLP and the ratio of protons emitted to detected, similar as in xCT[131].

Finally, an important topic that should be investigated is the applicability of pCT for organs in motion. Nowadays breath hold CT, slow CT, gated CT and 4DCT are some possible options adopted to overcome the organ motion during a CT scan[132,133] The possibility of using pCT for the same purpose would largely reduce the dose delivered to the patient. One of the advantages would be that tumour motion (and shrinking) could better monitored repeating the scan more often without delivering an excessive amount of radiation to the patient.

8.2 Conclusions

PCT is a promising modality for low-dose image guidance and adaptive proton therapy. Improved proton range accuracy may be achieved with pCT, because it provides a direct measurement of RSP from proton energy loss measurements[36]. The uncertainty and thus the added planning margin may be reduced to 1% or less of the proton range in most cases, and the dose delivered to the patient can also be reduced compared to CBCT[134], which makes pCT an attractive alternative for in-room image guidance.

Promising results were presented in this PhD thesis but lots of aspects can still be improved: the investigation in proton imaging is far to be over.

References

[1] H. Paganetti, *Proton Therapy Physics*. CRC Press, 2011.

[2] B. Schaffner and E. Pedroni, "The precision of proton range calculations in proton radiotherapy treatment planning: experimental verification of the relation between CT-HU and proton stopping power." *Physics in Medicine & Biology*, vol. 43, no. 6, pp. 1579–1592, 1998.

[3] R. W. Schulte, V. A. Bashkirov, T. Li *et al.*, "Conceptual design of a proton computed tomography system for applications in proton radiation therapy," *IEEE Transactions on Nuclear Science*, vol. 51, no. 3, pp. 866–872, 2004.

[4] H. F.-W. Sadrozinski, R. P. Johnson, S. Macafee *et al.*, "Development of a Head Scanner for Proton CT," *Nuclear Inst. and Methods in Physics Research, A*, vol. 699, pp. 205–210, 2013.

[5] S. Agostinelli, J. Allison, K. Amako *et al.*, "GEANT4 - A simulation toolkit," *Nuclear Instruments and Methods in Physics Research, Section A: Accelerators, Spectrometers, Detectors and Associated Equipment*, vol. 506, no. 3, pp. 250–303, 2003.

[6] R. W. Schulte, S. N. Penfold, J. T. Tafas *et al.*, "A maximum likelihood proton path formalism for application in proton computed tomography." *Medical Physics*, vol. 35, no. 11, pp. 4849–4856, 2008.

[7] H. B. Hewitt, "Rationalizing radiotherapy: some historical aspects of the endeavour," *The British Journal of Radiology*, vol. 46, no. 550, pp. 917–926, 1973.

[8] R. R. Wilson, "Radiological Use of Fast Protons," *Radiology*, vol. 47, no. 5, pp. 487–491, 1946.

[9] M. M. Urie, J. M. Sisterson, A. M. Koehler *et al.*, "Proton beam penumbra: effects of separation between patient and beam modifyng devices," *Medical Physics*, vol. 13, no. 5, pp. 734–741, 1986.

[10] S. N. Penfold, "Image reconstruction and Monte Carlo simulations in the development of proton computed tomography for applications in proton radiation therapy," Ph.D. dissertation, University of Wollongong, 2010.

[11] E. Hall, "Protons for radiotherapy: a 1946 proposal," *The Lancet Oncology*, vol. 10, no. 2, p. 196, 2009.

[12] J. M. Slater, J. O. Archambeau, D. W. Miller *et al.*, "The proton treatment center at Loma Linda University Medical Center: Rationale for and description of its development," *International Journal of Radiation Oncology, Biology, Physics*, vol. 22, no. 2, pp. 383–389, 1992.

[13] "http://www.proton-cancer-treatment.com/proton-therapy/proton-therapy-around-the-world/operating-clinical-proton-centres/."

[14] E. Bezak and L. Marcu, *Biomedical Physics in Radiotherapy for Cancer*, B. Allen, Ed. Springer-Verlag London, 2012.

[15] D. Dinesh Mayani, "Proton therapy for cancer treatment." *Journal of oncology pharmacy practice : official publication of the International Society of Oncology Pharmacy Practitioners*, vol. 17, no. 3, pp. 186–90, 2011.

[16] R. Zhang, R. M. Howell, P. J. Taddei *et al.*, "A comparative study on the risks of radiogenic second cancers and cardiac mortality in a set of pediatric medulloblastoma patients treated with photon or proton craniospinal irradiation," *Radiotherapy and Oncology*, vol. 113, no. 1, pp. 84–88, 2014.

[17] T. I. Yock and P. a. Caruso, "Risk of Second Cancers After Photon and Proton Radiotherapy," *Health Physics*, vol. 103, no. May, pp. 577–585, 2012.

[18] C. S. Chung, T. I. Yock, K. Nelson *et al.*, "Incidence of second malignancies among patients treated with proton versus photon radiation," *International Journal of Radiation Oncology Biology Physics*, vol. 87, no. 1, pp. 46–52, 2013.

[19] A. J. Lomax, T. Bortfeld, G. Goitein *et al.*, "A treatment planning inter-comparison of proton and intensity modulated photon radiotherapy," *Radiotherapy and Oncology*, vol. 51, no. 3, pp. 257–271, 1999.

[20] A. A. Mustafa and D. F. Jackson, "The relation between x-ray CT numbers and charged particle stopping powers and its significance for radiotherapy treatment planning," *Physics in Medicine & Biology*, vol. 28, no. 2, pp. 169–176, 1983.

[21] U. Schneider, E. Pedroni, and A. J. Lomax, "The calibration of CT Hounsfield units for radiotherapy treatment planning." *Physics in Medicine & Biology*, vol. 41, no. 1, pp. 111–24, 1996.

[22] N. Kanematsu, N. Matsufuji, and R. Kohno, "A CT calibration method based on the polybinary tissue model for radiotherapy treatment planning," *Physics in Medicine & Biology*, vol. 48, pp. 1053–1064, 2003.

[23] M. Yang, X. R. Zhu, P. C. Park *et al.*, "Comprehensive analysis of proton range uncertainties related to patient stopping-power-ratio estimation using the stoichiometric calibration," *Physics in Medicine & Biology*, vol. 57, pp. 4095–4115, 2012.

[24] "http://www.icru.org/home/reports/tissue-substitutes-in-radiation-dosimetry-and-measurement-report-44."

[25] N. Hudobivnik, F. Schwarz, T. Johnson *et al.*, "Comparison of proton therapy treatment planning for head tumors with a pencil beam algorithm on dual and single energy CT images," *Medical Physics*, vol. 495, no. 43, pp. 495–504, 2016.

[26] A. M. Cormack, "Representation of a Function by Its Line Integrals, with Some Radiological Applications," *Journal of Applied Physics*, vol. 34, no. 9, pp. 2722–2727, 1963.

[27] ——, "Representation of a Function by Its Line Integrals, with Some Radiological Applications II," *Journal of Applied Physics*, vol. 35, no. 10, pp. 2908–2913, 1964.

[28] A. M. Koehler, "Proton radiography," *Science*, vol. 160, pp. 303–304, 1968.

[29] A. M. Koehler and V. W. Steward, "Proton radiographic detection of strokes," *Nature*, vol. 245, no. 5419, pp. 38–40, 1973.

[30] D. R. Moffett, E. P. Colton, G. A. Concaildi *et al.*, "Initial test of a proton radiographic system," *IEEE Transactions on Nuclear Science*, vol. 22, no. 3, pp. 1749–1751, 1975.

[31] S. L. Kramer, R. L. Martin, D. R. Moffett *et al.*, "Application of proton radiography to medical imaging," in *SciTech Connect*, vol. 64, North America, Chicago (IL, USA), 1978.

[32] M. Goitein, "Three-dimensional density reconstruction from a series of two-dimensional projections," *Nuclear Instruments and Methods*, vol. 101, no. 3, pp. 509–518, 1972.

[33] A. M. Cormack and A. M. Koehler, "Quantitative proton tomography: preliminary experiments," *Physics in Medicine & Biology*, vol. 21, no. 4, p. 560, 1976.

[34] K. M. Hanson, J. N. Bradbury, T. M. Cannon *et al.*, "The application of protons to computed tomography," *IEEE Transactions on Nuclear Science*, vol. 25, no. 1, pp. 657–660, 1978.

[35] K. M. Hanson, "Proton computed tomography," *Modern Physics Letters A*, vol. 26, no. 1, pp. 1635–1640, 1979.

[36] K. M. Hanson, J. N. Bradbury, T. M. Cannon *et al.*, "Computed tomography using proton energy loss," *Physics in Medicine & Biology*, vol. 26, no. 6, pp. 965–983, 1981.

[37] K. M. Hanson, J. N. Bradbury, R. Koeppe *et al.*, "Proton computed tomography of human specimens." *Physics in Medicine & Biology*, vol. 27, no. 1, pp. 25–36, 1982.

[38] U. Schneider and E. Pedroni, "Proton radiography as a tool for quality contron in proton therapy," *Medical Physics*, vol. 22, no. 353, 1995.

[39] U. Schneider, J. Besserer, P. Pemler *et al.*, "First proton radiography of an animal patient." *Medical Physics*, vol. 31, no. 5, pp. 1046–1051, 2004.

[40] L. a. Feldkamp, L. C. Davis, and J. W. Kress, "Practical cone-beam algorithm," *Journal of the Optical Society of America A*, vol. 1, no. 6, p. 612, 1984.

[41] P. Zygmanski, K. P. Gall, M. S. Rabin *et al.*, "The measurement of proton stopping power using proton-cone-beam computed tomography." *Physics in Medicine & Biology*, vol. 45, no. 2, pp. 511–28, 2000.

[42] H. F.-W. Sadrozinski, V. A. Bashkirov, B. Keeney *et al.*, "Toward proton computed tomography," *IEEE Transactions on Nuclear Science*, vol. 51, no. 1 I, pp. 3–9, 2004.

[43] J. Missaghian, R. F. Hurley, V. A. Bashkirov *et al.*, "Beam test results of a CsI calorimeter matrix element," *Journal of Instrumentation*, vol. 5, no. 6, pp. 1–14, 2010.

[44] R. P. Johnson, J. DeWitt, C. Holcomb *et al.*, "Tracker Readout ASIC for Proton Computed Tomography Data Acquisition," *IEEE Transactions on Nuclear Science*, vol. 60, no. 5, pp. 3262–3269, 2013.

[45] V. A. Bashkirov, R. W. Schulte, R. F. Hurley *et al.*, "Novel scintillation detector design and performance for proton radiography and computed tomography," *Medical Physics*, vol. 43, no. 2, pp. 664–674, 2016.

[46] G. Poludniowski, N. M. Allinson, P. M. Evans *et al.*, "Proton radiography and tomography with application to proton therapy," *British Institute of Radiology*, vol. 88, no. 1053, 2015.

[47] A. Dyshkant, B. Erdelyi, A. Gearhart *et al.*, "Development of a proton Computed Tomogrcaphy (pCT) scanner at NIU," 2013.

[48] G. A. P. Cirrone, G. Cuttone, G. Candiano *et al.*, "Monte Carlo studies of a Proton Computed Tomography System," *IEEE Transactions on Nuclear Science*, vol. 54, no. 5, pp. 1487–1491, 2007.

[49] D. Menichelli, M. Bruzzi, M. Bucciolini *et al.*, "Characterization of a silicon strip detector and a YaG: Ce calorimeter for a proton computed radiography apparatus," *IEEE Transactions on Nuclear Science*, vol. 57, no. 1, pp. 8–16, 2010.

[50] V. Sipala, M. Brianzi, M. Bruzzi *et al.*, "PRIMA: An apparatus for medical application," *Nuclear Instruments and Methods in Physics Research, Section A: Accelerators, Spectrometers, Detectors and Associated Equipment*, vol. 658, no. 1, pp. 73–77, 2011.

[51] M. Scaringella, M. Brianzi, M. Bruzzi *et al.*, "The PRIMA (PRoton IMAging) collaboration: Development of a proton Computed Tomography apparatus," *Nuclear Inst. and Methods in Physics Research, A*, vol. 730, pp. 178–183, 2013.

[52] E. Vanzi, M. Bruzzi, M. Bucciolini *et al.*, "The PRIMA collaboration : Preliminary results in FBP reconstruction of pCT data," *Nuclear Inst. and Methods in Physics Research, A*, vol. 730, pp. 184–190, 2013.

[53] C. Civinini, M. Bruzzi, M. Bucciolini *et al.*, "Recent results on the development of a proton computed tomography system," *Nuclear Inst. and Methods in Physics Research, A*, vol. 732, pp. 573–576, 2013.

[54] M. Scaringella, M. Bruzzi, M. Bucciolini *et al.*, "A proton Computed Tomography based medical imaging system," in *Journal of Instrumentation*, vol. 12009, Guildford, Surrrey, UK, 2014, pp. 1–8.

[55] D. Lo Presti, D. L. Bonanno, F. Longhitano *et al.*, "Design and Characterization of a Real Time , Large Area , High Spatial Resolution Particle Tracker Based on Scintillating Fibers," *Advances in high energy physics*, vol. 2, no. 4, pp. 159–174, 2013.

[56] D. Lo Presti, D. Bonanno, F. Longhitano *et al.*, "A real-time, large area, high space resolution particle radiography system," in *Journal of Instrumentation*, vol. 06012, no. 6, Paris, France, 2014, pp. 1–10.

[57] J. T. Taylor, P. P. Allport, G. L. Casse *et al.*, "Proton tracking for medical imaging and dosimetry," in *Journal of Instrumentation*, vol. 10, 2015, p. 2.

[58] J. T. Taylor, C. Waltham, T. Price *et al.*, "A new silicon tracker for proton imaging and dosimetry," *Nuclear Inst. and Methods in Physics Research, A*, pp. 1–5, 2016.

[59] T. Price, "PRaVDA : High Energy Physics towards proton Computed Tomography," *Nuclear Inst. and Methods in Physics Research, A*, vol. 824, no. 1, pp. 226–227, 2016.

[60] T. Price, M. Esposito, G. Poludniowski *et al.*, "Expected proton signal sizes in the PRaVDA Range Telescope for proton Computed Tomography," *Journal of Instrumentation*, vol. 10, no. 5, pp. 1–9, 2015.

[61] M. Akisada, J. Ohashi, K. Kondo *et al.*, "Conceptual Design of Proton Computed Tomography with Magnetic Spectrometer," *Japanese Journal of Applied Phyiscs*, vol. 22, no. 4, pp. 752–758, 1983.

[62] Y. Saraya, T. Izumikawa, J. Goto *et al.*, "Study of spatial resolution of proton computed tomography using a silicon strip detector," *Nuclear Inst. and Methods in Physics Research, A*, vol. 735, pp. 485–489, 2014.

[63] T. Kawasaki, T. Izumikawa, J. Goto *et al.*, "High rate silicon tracker for proton computed tomography," in *Nuclear Science Symposium Conference Record*, no. 2, 2014, pp. 2–5.

[64] S. Tanaka, T. Nishio, and K. Matsushita, "Development of proton CT imaging system using plastic scintillator and CCD camera," *Physics in Medicine & Biology*, vol. 61, no. 11, pp. 4156–4167, 2016.

[65] W. D. Newhauser and R. Zhang, "The physics of proton therapy," *Physics in Medicine & Biology*, vol. 60, no. 8, pp. R155 – 201, 2015.

[66] O. Voskresenskaya and A. Tarasov, "Moliere's multiple scattering theory revisited," 2012. [Online]. Available: http://arxiv.org/abs/1204.3675

[67] U. Schneider, E. Pedroni, M. Hartmann *et al.*, "Spatial resolution of proton tomography: Methods, initial phase space and object thickness," *Zeitschrift fur Medizinische Physik*, vol. 22, no. 2, pp. 100–108, 2012.

[68] T. E. Plautz, V. A. Bashkirov, V. Giacometti *et al.*, "An evaluation of spatial resolution of a prototype proton CT scanner," *Medical Physics*, vol. 43, no. 12, pp. 6291–6300, 2016.

[69] M. A. Hayat, *Cancer Imaging: Instrumentation and Applications*. Academic Press, 2007.

[70] H. Bethe, "Zur theorie des durchgangs schneller korpuskularstrahlen durch materie," *Ann. Phys.*, vol. 5, pp. 324–400, 1930.

[71] F. Bloch, "Zur bremsung rasch bewegter teilchen beim durchgang durch materie," *Ann. Phys.*, vol. 16, pp. 285–320, 1933.

[72] J. F. Ziegler, "The Stopping of Energetic Light Ions in Elemental Matter," *Journal of Applied Physics*, vol. 85, no. 3, pp. 1249–1272, 1999.

[73] R. W. Schulte, V. A. Bashkirov, M. C. L. Klock *et al.*, "Density resolution of proton computed tomography." *Medical Physics*, vol. 32, no. 4, pp. 1035–1046, 2005.

[74] H. Paganetti, "Nuclear interactions in proton therapy: dose and relative biological effect distributions originating from primary and secondary particles," *Phys. Med. Biol*, vol. 47, no. 5, pp. 747–766, 2002.

[75] "http://www.icru.org/home/reports/clinical-proton-dosimetry-part-i-beam-production-beam-delivery-and-measurement-of-absorbed-dose."

[76] R. F. Laitano, M. Rosetti, and M. Frisoni, "Effects of nuclear interactions on energy and stopping power in proton beam dosimetry," *Nuclear Instruments and Methods in Physics Research, Section A: Accelerators, Spectrometers, Detectors and Associated Equipment*, vol. 376, no. 3, pp. 466–476, 1996.

[77] M. Goitein and M. Jermann, "The relative costs of proton and X-ray radiation therapy," *Clinical Oncology*, vol. 15, no. 1, 2003.

[78] M. Lodge, M. Pijls-Johannesma, L. Stirk *et al.*, "A systematic literature review of the clinical and cost-effectiveness of hadron therapy in cancer," *Radiotherapy and Oncology*, vol. 83, no. 2, pp. 110–122, 2007.

[79] J. Lundkvist, M. Ekman, S. R. Ericsson *et al.*, "Cost-effectiveness of proton radiation in the treatment of childhood medulloblastoma," *Cancer*, vol. 103, no. 4, pp. 793–801, 2005.

[80] ——, "Economic evaluation of proton radiation therapy in the treatment of breast cancer," *Radiotherapy and Oncology*, vol. 75, no. 2, pp. 179–185, 2005.

[81] E. Clements, "Pursuing protons for medical imaging | symmetry magazine," *Symmetry Magazine*, 2012.

[82] A. Zatserklyaniy, R. P. Johnson, S. Macafee *et al.*, "Track Reconstruction with the Silicon Strip Tracker of the Proton CT Phase-2 Scanner," in *2014 IEEE Nuclear Science Symposium and Medical Imaging Conference (NSS/MIC)*, Seattle, WA, 2014, pp. 1–4.

[83] R. P. Johnson, V. A. Bashkirov, L. Dewitt *et al.*, "A Fast Experimental Scanner for Proton CT: Technical Performance and First Experience With Phantom Scans," *IEEE Transactions on Nuclear Science*, vol. 63, no. 1, pp. 52–60, 2016.

[84] H. Zaidi and X. G. Xu, "Computational anthropomorphic models of the human anatomy: the path to realistic Monte Carlo modeling in radiological sciences." *Annual review of biomedical engineering*, vol. 9, no. 1, pp. 471–500, 2007.

[85] C. Lee, J. L. Williams, C. Y. Lee *et al.*, "The UF series of tomographic computational phantoms of pediatric patients." *Medical Physics*, vol. 32, no. 12, pp. 3537–3548, 2005.

[86] J. C. Nipper, J. L. Williams, and W. E. Bolch, "Creation of two tomographic voxel models of paediatric patients in the first year of life," *Physics in Medicine & Biology*, vol. 47, no. 17, pp. 3143–3164, 2002.

[87] C. Lee, D. Lodwick, J. Hurtado *et al.*, "The UF family of reference hybrid phantoms for computational radiation dosimetry." *Physics in Medicine & Biology*, vol. 55, no. 10, pp. 339–363, 2010.

[88] M. Caon, G. Bibbo, and J. Pattison, "An EGS4-ready tomographic computational model of a 14-year-old female torso for calculating organ doses from CT examinations voxel-based computational models Organ and effective doses in newborn patients during MSCT An EGS4-ready," *Physics in Medicine & Biology*, vol. 44, no. 9, pp. 2213–2225, 1999.

[89] J. L. Ioppolo, R. I. Price, T. Tuchyna *et al.*, "Diagnostic x-ray dosimetry using Monte Carlo simulation," *Physics in Medicine & Biology*, vol. 47, no. 10, pp. 1707–1720, 2002.

[90] G. Gualdrini, P. Battisti, R. Biagini *et al.*, "Development and characterisation of a head calibration phantom for in vivo measurements of actinides," *Applied Radiation and Isotopes*, vol. 53, no. 1-2, pp. 387–393, 2000.

[91] F. M. Milian, A. Attili, G. Russo *et al.*, "Development of virtual CT DICOM images of patients with tumors: application for TPS and Monte Carlo dose evaluation," in *International Nuclear Atlantic Conference*, Recife, PE (Brazil), 2013, pp. 24–29.

[92] J. Allison, K. Amako, J. Apostolakis *et al.*, "Geant4 developments and applications," *IEEE Transactions on Nuclear Science*, vol. 53, no. 1, pp. 270–278, 2006.

[93] R. W. Schulte, V. A. Bashkirov, R. P. Johnson *et al.*, "Overview of the LLUMC/UCSC/CSUSB Phase 2 Proton CT Project," *Trans. Am. Nucl. Soc.*, vol. 106, pp. 59–62, 2012.

[94] J. Allison, K. Amako, J. Apostolakis *et al.*, "Recent developments in Geant4," *Nuclear Instruments and Methods in Physics Research, Section A: Accelerators, Spectrometers, Detectors and Associated Equipment*, vol. 835, pp. 186–225, 2016.

[95] G. Coutrakon, J. Hubbard, J. Johanning *et al.*, "A performance study of the Loma Linda proton medical accelerator." *Medical Physics*, vol. 21, no. 11, pp. 1691–1701, 1994.

[96] S. Chauvie, S. Guatelli, V. Ivanchenko *et al.*, "Geant4 low energy electromagnetic physics," in *2004 IEEE Nuclear Science Symposium and Medical Imaging Conference (NSS/MIC)*, vol. 3, no. C, Rome, 2004, pp. 1881–1885.

[97] Https://geant4.web.cern.ch/geant4/UserDocumentation/UsersGuides/ForApplicationDeveloper/html/ch06s "Geant4."

[98] W. R. Leo, *Techniques for Nuclear and Particle Physics Experiments : A How-to Approach*. Berlin: K, Springer-Verlag Berlin and Heidelberg GmbH & Co., 1994.

[99] R. F. Hurley, R. W. Schulte, V. A. Bashkirov *et al.*, "Water-equivalent path length calibration of a prototype proton CT scanner," *Medical Physics*, vol. 39, no. 5, pp. 2438–2446, 2012.

[100] V. A. Bashkirov, R. P. Johnson, V. Giacometti *et al.*, "A Novel Phantom and Method for Calibration of the Phase II Proton CT Scanner," in *2014 IEEE Nuclear Science Symposium and Medical Imaging Conference (NSS/MIC)*, 2014.

[101] T. Dou, J. Ramos-Mendez, P. Piersimoni *et al.*, "SU-E-J-148: Tools for Development of 4D Proton CT," in *Medical Physics*, vol. 42, no. 6, jun 2015, pp. 3298–3299.

[102] D. De Ruysscher, E. Sterpin, K. Haustermans *et al.*, "Tumour movement in proton therapy: Solutions and remaining questions: A review," *Cancers*, vol. 7, no. 3, pp. 1143–1153, 2015.

[103] S. N. Penfold, R. W. Schulte, Y. Censor *et al.*, "Total variation superiorization schemes in proton computed tomography image reconstruction." *Medical Physics*, vol. 37, no. 11, pp. 5887–5895, 2010.

[104] S. Rit, G. Dedes, N. Freud *et al.*, "Filtered backprojection proton CT reconstruction along most likely paths," *Medical Physics*, vol. 40, no. 3, pp. 31 103–31 109, 2016.

[105] D. Wang, T. R. Mackie, and W. Tomé, "On the use of a proton path probability map for proton computed tomography reconstruction." *Medical Physics*, vol. 37, no. 8, pp. 4138–4145, 2010.

[106] G. Poludniowski, N. M. Allinson, and P. M. Evans, "Proton computed tomography reconstruction using a backprojection-then-filtering approach," *Physics in Medicine & Biology*, vol. 59, no. 24, pp. 7905–7918, 2014.

[107] S. N. Penfold and Y. Censor, "Techniques in Iterative Proton CT Image Reconstruction," *Sensing and Imaging*, vol. 16, no. 1, pp. 1–19, 2015.

[108] A. Mirandola, S. Molinelli, G. Vilches Freixas *et al.*, "Dosimetric commissioning and quality assurance of scanned ion beams at the Italian National Center for Oncological Hadrontherapy," *Medical Physics*, vol. 42, no. 9, pp. 5287–5300, 2015.

[109] Https://www.python.org/, "Python.org."

[110] Http://geant4.web.cern.ch/geant4/UserDocumentation/Doxygen/examples_doc/html/DICOM, "_8cc_source.html."

[111] H. Paganetti, "Range uncertainties in proton therapy and the role of Monte Carlo simulations." *Physics in Medicine & Biology*, vol. 57, no. 11, pp. 99–117, 2012.

[112] H. Jianga, J. Seco, and H. Paganetti, "Effects of Hounsfield number conversion on CT based proton Monte Carlo dose calculations," *Medical Physics*, vol. 34, no. 4, pp. 1439–1449, 2007.

[113] S. España and H. Paganetti, "The impact of uncertainties in the CT conversion algorithm when predicting proton beam ranges in patients from dose and PET-activity distributions," *Physics in Medicine & Biology*, vol. 55, no. 24, pp. 7557–7571, 2010.

[114] K. Amako, S. Guatelli, V. Ivanchenko *et al.*, "Validation of Geant4 electromagnetic physics versus protocol data," *2004 IIEEE Nuclear Science Symposium and Medical Imaging Conference (NSS/MIC)*, vol. 4, pp. 1–5, 2004.

[115] M. Testa, J. M. Verburg, M. Rose *et al.*, "Proton radiography and proton computed tomography based on time-resolved dose measurements." *Physics in Medicine & Biology*, vol. 58, no. April, pp. 8215–33, 2013.

[116] S. Mutic, J. R. Palta, E. K. Butker *et al.*, "Quality assurance for computed-tomography simulators and the computed-tomography-simulation process: report of the AAPM Radiation Therapy Committee Task Group No. 66." *Medical Physics*, vol. 30, no. 66, pp. 2762–2792, 2003.

[117] K. McMillan, M. McNitt-Gray, and D. Ruan, "Development and validation of a measurement-based source model for kilovoltage cone-beam CT Monte Carlo dosimetry simulations." *Medical Physics*, vol. 40, no. 11, p. 111907, 2013.

[118] M. F. Chan, J. Yang, Y. Song *et al.*, "Evaluation of imaging performance of major image guidance systems," *Biomedical Imaging and Intervention Journal*, vol. 7, no. 2, pp. 1–7, 2011.

[119] T. Li, Z. Liang, J. V. Singanallur *et al.*, "Reconstruction for proton computed tomography by tracing proton trajectories – A Monte Carlo study," *Medical Physics*, vol. 33, no. 3, pp. 699–706, 2006.

[120] D. C. Williams, "The most likely path of an energetic charged particle through a uniform medium," *Physics in Medicine & Biology*, vol. 49, no. 13, p. 2899, 2004.

[121] G. O. Sawakuchi, U. Titt, D. Mirkovic *et al.*, "Density heterogeneities and the influence of multiple Coulomb and nuclear scatterings on the Bragg peak distal edge of proton therapy beams," *Physics in Medicine & Biology*, vol. 53, no. 53, pp. 4605–4605, 2008.

[122] M. Martišíková, J. Jakubek, C. Granja *et al.*, "Measurement of secondary radiation during ion beam therapy with the pixel detector Timepix," *Journal of Instrumentation*, vol. 6, no. 11, pp. C11 014–C11 014, 2011.

[123] X. Llopart, R. Ballabriga, M. Campbell *et al.*, "Nuclear Instruments and Methods in Physics Research Section A: Accelerators, Spectrometers, Detectors and Associated Equipment," *Nuclear Instruments and Methods in Physics Research Section A: Accelerators, Spectrometers, Detectors and Associated Equipment*, vol. 581, no. 1-2, pp. 485–494, 2007.

[124] X. Llopart and M. Campbell, "First test measurements of a 64 k pixel readout chip working in single photon counting mode," *Nuclear Instruments and Methods in Physics Research, Section A: Accelerators, Spectrometers, Detectors and Associated Equipment*, vol. 509, no. 1-3, pp. 157–163, 2003.

[125] "http://aladdin.utef.cvut.cz/ofat/index.html."

[126] "http://pdg.lbl.gov/2016/AtomicNuclearProperties/."

[127] K. Wong, B. Erdelyi, R. W. Schulte *et al.*, "The Effect of Tissue Inhomogeneities on the Accuracy of Proton Path Reconstruction for Proton Computed Tomography," in *AIP Conf. Proc.*, Fort Worth (Texas), 2009, pp. 476–482.

[128] Y. Takada, K. Kondo, T. Marume *et al.*, "Proton computed tomography with a 250 MeV pulsed," *Nuclear Instruments and Methods in Physics Research Section A: Accelerators, Spectrometers, Detectors and Associated Equipment*, vol. 273, no. 1, pp. 410–422, 1988.

[129] B. Schultze, M. Witt, Y. Censor *et al.*, "Performance of Hull-Detection Algorithms For Proton Computed Tomography Reconstruction," *Contemporary Mathematics*, vol. 636, pp. 211–224, 2015.

[130] S. Rit, R. Clackdoyle, J. Hoskovec *et al.*, "List-mode proton CT reconstruction using their most likely paths via the finite Hilbert transform of the derivative of the backprojection," *Fully3D*, vol. Submitted, pp. 324–327, 2015.

[131] C. T. Quiñones, J. M. Létang, and S. Rit, "Filtered back-projection reconstruction for attenuation proton CT along most likely paths," *Physics in Medicine & Biology*, vol. 61, no. 9, pp. 3258–3278, 2016.

[132] M. S. Nazmy, Y. Khafaga, A. Mousa *et al.*, "Cone beam CT for organs motion evaluation in pediatric abdominal neuroblastoma," *Radiotherapy and Oncology*, vol. 102, no. 3, pp. 388–392, 2012.

[133] W. Wang, J. B. Li, H. G. Hu *et al.*, "Correlation between target motion and the dosimetric variance of breast and organ at risk during whole breast radiotherapy using 4DCT." *Radiation Oncology*, vol. 8, no. 1, p. 111, 2013.

[134] V. A. Bashkirov, R. P. Johnson, H. F.-W. Sadrozinski *et al.*, "Development of proton computed tomography detectors for applications in hadron therapy," *Nuclear Instruments and Methods in Physics Research, Section A: Accelerators, Spectrometers, Detectors and Associated Equipment*, vol. 809, pp. 120–129, 2016.